Università degli Studi di Ferrara
Universitè de Nice Sophia Antipolis
International Relativistic Astrophysics PhD
Erasmus Mundus

PhD Thesis

Gamma-ray Lens: Development and Test

Supervisor
Prof. Filippo Frontera
Co-Supervisor
Dott. Enrico Virgilli

Candidate
Vincenzo Liccardo

Ferrara, November 2013

To my beloved grandmother

God runs electromagnetics by wave theory on Monday, Wednesday, and Friday, and the Devil runs them by quantum theory on Tuesday, Thursday, and Saturday.
(Sir William Bragg)

List of Figures

Contents

Acknowledgements

I acknowledge the support from Erasmus Mundus Joint Doctorate Program by Grant Number 2010-1816 from the EACEA of the European Commission. The LAUE project is the result of huge efforts of large number of organizations and people. I would like to thank all of them. I also acknowledge the ASI (Italian Space Agency) for its support to the LAUE project under contract I/068/09/0.

I would like to thank my supervisor Prof. Filippo Frontera for his teaching during the 3 years. He also encouraged me during the first school in Nice, when I was still deciding which project of the PhD program join. He was always present to help me whenever required, and I couldn't have asked for more. I will always be indebted to him for giving me an insight into this wonderful topic. I am very much grateful and looking forward to work with him in the years to come.

This PhD has been less tough thanks to my friend and fellow, Enrico Virgilli. His funny, quick and smart way of thinking has helped me to develop my research skills. A great companion, he is the core of friends network that I have here in Ferrara. I am also thankful to him for sharing with me many travels which I will never forget.

Over these three years, I was fortunate to have a quite flatmate, Vineeth Valsan. My collaborator in the lab, a great photographer and a great indian chef, he has whole heartedly made a number of delicious Indian cuisines, sometimes a little bit hot, but nevertheless I have enjoyed a lot. Words of gratitude will not be enough for his endless friendship.

Experimental stages are always with unlikely and untimely event of hitches. Vito Carassiti and Stefano Squerzanti were always there to help us at these

times. I am thankful to them for their aid, without which this project would have faced enormous delay.

Roberto Verbeni is one of the energetic people, I have ever met, who kindly welcomed me during the months in Grenoble. The charm and liveliness he posses along with his intellect, were very helpful for me in my work. I am thankful to him for teaching me a different topic, for the several scientific discussions we had and also for introducing me many people working at the ESRF.

My heartfelt gratefulness also goes to Stefano Silvestri and Angelo Basili for the humorous environment they provided during the final year of my thesis and of course, also for numerous biscuits.

The unconditional love and support I get from my family is the backbone to the thoughts that move me forward. My parents, grandparents and my sister have always been there for me. I will always be beholden to these vibrant people.

Introduction

The role of X-ray astronomy (energies greater than 2 keV) is now widely recognized. Currently the X-ray telescopes are divided into two categories according to their ability to focus or not the photons: in a focusing telescope the flux is given by the photons concentrated by the optics onto a detector, with a giant increase in sensitivity and angular resolution, while the telescopes belonging to the second class are essentially composed of a direct view detector equipped with collimators and / or coded masks.

Until few years ago, the focusing optics were efficient for energies lower than 10 keV, while for higher energies, all the instruments were based on the direct view optics [1], [2]; Just the last year *The Nuclear Spectroscopic Telescope Array (NuSTAR)* mission, has been launched being the first focusing high-energy X-ray telescope in orbit. NuSTAR operates in the band 3-79 keV, extending the sensitivity of focusing far beyond the ∼10 keV high-energy cutoff achieved by all previous X-ray satellites [4].

The best technique to focus X-rays with energies lower than 70 keV is the Bragg diffraction by multilayers. These are composed of a series of superimposed layers, alternating a low Z material with a high Z of defined thickness [3]. However, at the energies greater then 70 keV, the mirrors consisting of multilayers become quite inefficient [5], and the Bragg diffraction by crystals in Laue geometry (transmission) appears to be the best method to face the problem of focusing X-ray at high energies. In addition, in the last years bent crystals have become available, taking advantage of their high reflectivity and excellent PSF with respect to the mosaic flat crystals, encouraging the employment of Laue optics for high energy astrophysics researches [6]. Therefore, it becomes crucial to develop techniques for the control of important parameters, such as curvature, *mosaicity*, *angular spread* and $reflectivity$, and also measurement techniques able to characterize the crystals produced.

The group of high-energy astrophysics in Ferrara has been working for several years on the possibility to focus X-rays with crystals [7]. Studies have now reached a good degree of maturity, and the possibility to construct a Laue lens prototype with the aim of proposing a mission by satellite seems, at this point, to be a concrete prospect. During my PhD, I have been initialy involved in the activity of realization and test of the second Laue lens prototype built in the LARIX facility of the Physics and Earth Science Department of Ferrara. The prototype consists of a set of 20 crystals placed in a circular ring and capable to focus 100 keV photons at a focal distance of 6 m. Moreover, I have taken part to a more ambitious and technologic project named LAUE, supported by ASI and still on going, whose aim among others, is to build a Laue lens petal with a 20 m focal length. In the last three years I have been working in particular in the LARIX (Large Italian X-ray facility) laboratory of the University of Ferrara, where thanks to this X-ray facility, I performed many measurements regarding the characterization of the crystals. I have also taken part to the assembling phase of the new LARIX facility in which the LAUE project is now located, the facility being in a 100m long tunnel. The new facility is designed to meet the demands of the LAUE project and it will be possible to calibrate the new focusing optics which are considered, by now, the future of Astrophysics in the hard X-/soft gamma-ray energy range.

This thesis is a presentation of the most significant results obtained in the recent years in the LARIX laboratory. In addition to a brief description of the tools and techniques of X-ray radiation detection and an introduction to the X-ray diffraction theory, in this thesis I will present the HAXTEL project, the LAUE project and eventually the results achieved, including the discussion and the comparison with the expectations. The thesis work will also focus on the measurements performed on the new generation of bent crystals (Germanium, Silicon and Gallium Arsenide), which for the first time can be provided with a good reproducibility in terms of curvature and efficiency. The tests carried out in the LARIX facility have been crucial for the choice of the best materials and for deeper studying the features of this class of crystals, which will be used for the first time to build Laue lens for space applications.

Finally, I will also present, in the appendix, part of my work performed during the mobility period at the European Synchrotron Radiation Facility (ESRF) in Grenoble, France.

Chapter 1

Status of Hard X-/Gamma-ray Astronomy

We know that X-rays are a form of electromagnetic radiation, like visible light, but the individual quanta of radiation, the photons, have energy at least a thousand times that of optical photons. X-rays from cosmic sources cannot penetrate even the thin outer layers of the Earth's atmosphere. It is thus impossible to observe X-rays from astronomical sources with ground-based instruments.Hence, observing from above the atmosphere is essential in this field. To see any X-rays at all, it is necessary to be above 99 % of the atmosphere, and to detect X-rays in the band where sources are most prominent.

In the following section I will present a brief history of the X-ray astronomy, focusing in particular on the broadband hard X-ray missions. I will also present some open astrophysical issues in the hard X-/soft gamma-ray band.

1.1 X-rays from stars

Celestial X-rays can be produced by several processes (thermal process, bremsstrahlung, synchrotron etc.). Since the X-ray photon energies are 1000 times greater than that of optical photons, the process to produce X-rays must be more energetic. Thus, if X-rays are generated in a thermal process, the temperature must be of the order of 1000 times greater than that in places where visible light is produced. Therefore, a search for cosmic X-ray sources is a search for materials at temperatures of millions (or more) degrees, in contrast to the familiar stars with surface temperatures of thousands of degrees.

Until 1962, very few astronomers believed that the Universe contained such objects capable of generating detectable amounts of high energy radiation. These ideas changed dramatically in the early 1960s with the discovery of the strong source of X-rays SCO X-1, and of a diffuse celestial X-ray background. Some X-ray sources have a strange and powerful emission that Astronomers had to introduce new classes of cosmic objects and astrophysical processes to explain them.

1.2 An brief history of the X-ray sky

The American Science and Engineering (AS&E) group, led by Riccardo Giacconi, discovered by chance the first cosmic source of X-radiation because their main goal was the detection of X-ray fluorescence from the Moon. The rocket launch of the AS&E instrument, on a new Aerobee rocket, took place from White Sands, New Mexico, on 18 June 1962. Two of the three X-ray Geiger counters worked well and, although they failed to detect any X- rays from the Moon's surface, they made the first detection of a powerful cosmic X-ray source [9], SCO X-1, in the Scorpius costellation (Fig.1.1).

After the discovery of Sco X-1, astronomers were thus forced to recognise that there were many objects at stellar distances which were unbelievably strong, although the nature of the X-ray sources and the occurring processes in which energy was generated was not obvious.

A convincing explanation of its nature was not found until 1971 when Uhuru discovered and measured the peculiar X-ray variation of another source that lies in the southern sky in the Centaurus constellation (Cen X-3). The Uhuru observations of Cen X-3, made in 1971, were spectacular [10]. The X-ray observations determined the nature of the source.

After this, many other X-ray sources were detected within our Galaxy, and mostly of them are accretion-powered binaries, in which a normal star and a compact star are locked in a close orbit. The accretion-powered sources

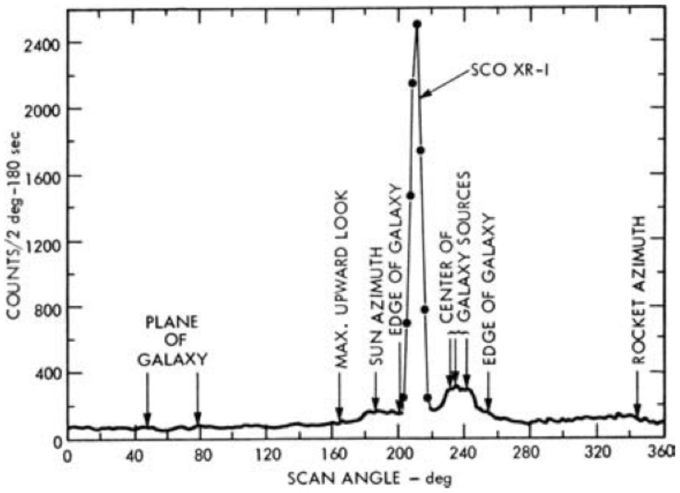

Figure 1.1: Three minutes of data from a rocket-borne X-ray detector flown in October 1967. This shows the counting rate of the detector as it scanned a great circle containing the source Sco X-1 and a cluster of sources in the direction of the galactic centre. The signal from Sco X-1 is very strong. (from Hill et al., 1968).

are the most luminous in our galaxy. Some have X-ray luminosities $L \approx 10^{38}$ erg s^{-1}.

Another class of very bright astronomical X-ray sources is that of the supernova remnants. The Crab Nebula is the first observed object belonging to this class. Neverthless, the X-ray luminosity of most remmants is 10-100 times lower than that of the Crab Nebula and the spectrum is softer, such that the low energy absorption is much more severe, making much more difficult the observations (Fig.1.2).

The first satellite/observatory specifically designed for an all-sky survey was HEAO-1 in 1979, which used an array of large-area proportional counters. The result was a catalogue containing 842 sources. Ten years later, ROSAT satellite mapped the soft X-ray sky (0.1-2.5 keV) for the first time using an imaging telescope and low-background detector. Its detection limit was 8.5 $\times$ 10^{-6} ph/cm^2/s/keV in 10^5 s (the most sensitive X-ray instrument at that time), and the first version of the ROSAT catalogue (Fig. 1.3) contained more than 18000 sources, both galactic and extragalactic [11].

The HEAO-2 observatory (later known as "Einstein"), was launched on

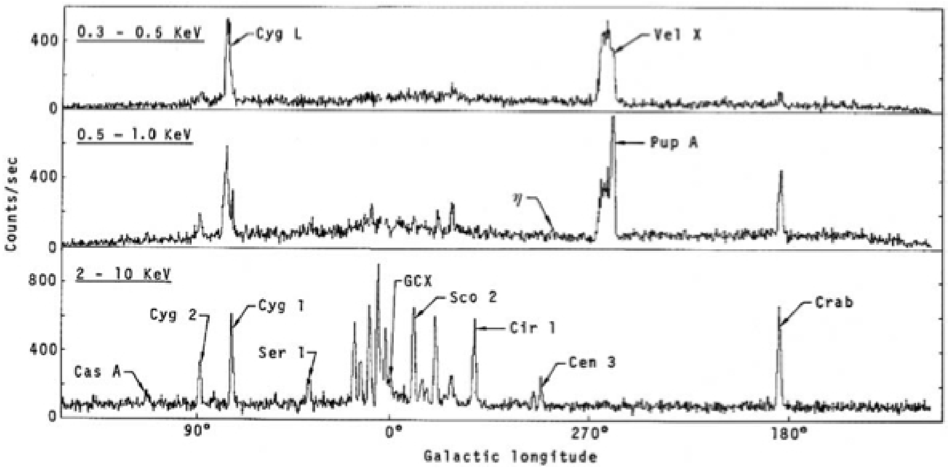

Figure 1.2: The entire Milky Way as surveyed with rocket-borne proportional counters in May 1970, May 1971, and October 1972 (Seward et al., 1972). Data from the three flights have been combined to show counting rate as a function of galactic longitude in three energy bands. There are no soft X-rays observed from the cluster of bright sources around the galactic centre.

November 13, 1978. A set of 4 Wolter type 1 nested mirrors focussed X-rays from 0.2 to 4 keV. Spatial resolution was 5 arcsec on axis, degrading to 1.5 arcmin at the edge of the 1° field of view. X-ray imaging was the principal aim of the mission [14]. The theoretical effective mirror area ranges from about 400 cm^2 at 0.25 keV down to about 30 cm^2 at 4 keV. The limit sensitivity was about 5×10^{-6} $\mathrm{ph/cm^2/s/keV}$.

In addition to the imagers, two high-resolution spectrometers were included (Fig. 1.4). The objective grating spectrometer (OGS) was a set of gold diffraction gratings which could be inserted into the telescope light path. The dispersed spectrum was recorded by one of the imagers. The focal-plane crystal spectrometer (FPCS) was a curved-crystal which operated at the telescope focus. Their small effective area ($\approx$ 10 cm^2 or less) make them useful for the brightest sources.

Einstein accomplished 5600 observations allowing us to see for the first time the structure of supernova remnants, the distribution of sources in normal galaxies and the structure of clusters of galaxies.

A big leap forward in terms of angular resolution occurred in 1999 with

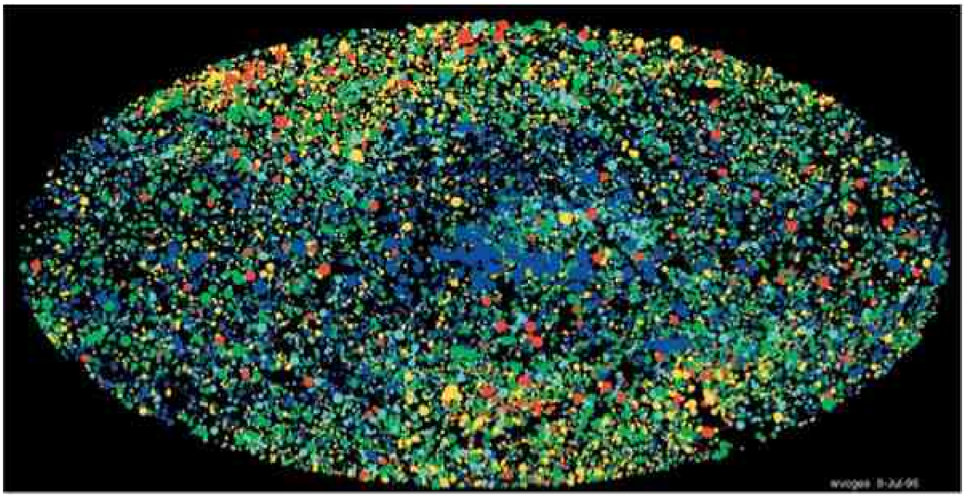

Figure 1.3: Map showing X-ray sources from the ROSAT all-sky survey in the energy band 0.1-2.4 keV. Size of the dot shows the brightness of the source. Colours indicate energy - going from red (soft) to blue (hard). Absorption in the Interstellar Medium (ISM) removes all soft X-rays from sources in the galactic plane especially towards the galactic centre. (from Voges et al., 1999).

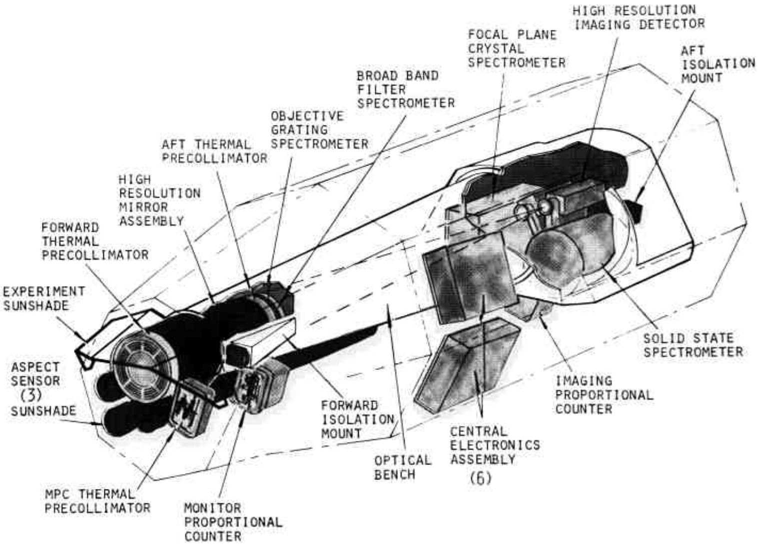

Figure 1.4: Configuration of the Einstein Observatory.

the launch of the Advanced X-ray Astrophysics Facility "Chandra" (passband 0.1-10 keV) designed to have 4 times the area of the Einstein mirror at low energies and to have a considerable collecting area between 6 and 7 keV (from 800 cm^2 at 0.25 keV down to about 100 cm^2 at 8 keV), the energy of the iron lines emitted by most astrophysical sources. An order of magnitude better angular resolution was achieved (0.5 arcsec), and sensitivity ($\sim 5 \times 10^{-8}$ ph/cm^2/s/keV, detection in 10^5 s) is 2 orders of magnitude better than that of Einstein .

The telescope consists of a set of 8 Wolter type 1 nested reflecting surfaces (Fig. 1.5) with a field of view depending on the camera (HRC-I: $\sim 30 \times 30$ arcmin, HRC-S: 6×90 arcmin). The response at energies between 7 and 10 keV is achieved by use of small reflection angles and by coating the three inner mirrors with iridium. The combination of high spatial resolution, higher effective area and sensitivity makes possible the study of extremely faint sources in crowded fields.

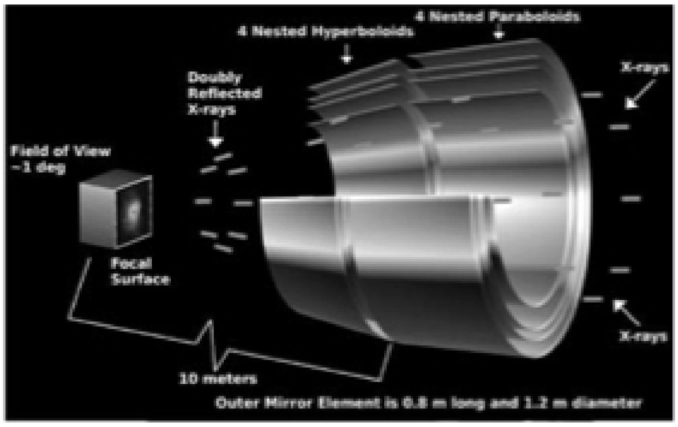

Figure 1.5: The geometry of the Chandra mirrors. Reflection angles are greatly exaggerated. An annular on-axis beam enters the aperture of each mirror pair. X-rays are first reflected from the inner surface of the parabolic mirror and then from the inner surface of the hyperbolic mirror (NASA/CXC/ D. Berry 2010).

There are four focal plane instruments and a mechanism to place any one of them at the telescope focus. The Advanced CCD Imaging Spectrometer (ACIS) is a collection of 10 CCD chips, four in an imaging array (which has a 16×16 arcmin field of view) and six in a linear array for spectroscopy. The

High Resolution Camera (HRC) comprises two detectors: HRC-I is a square micro-channel plate with a field of view of 40′; HRC-S was made for soft X-ray spectroscopy covering the low-energy transmission grating (LETG) dispersion pattern from 0.07 to 10 keV. There are three diffraction gratings which can be rotated into the telescope beam, and the diffracted spectra are imaged with focal plane detectors [19].

In the same year also the European X-ray Multi-Mirror Mission "XMM-Newton" was launched. Like Chandra, it is designed for a combination of imaging spectroscopy and high-resolution grating spectroscopy in the energy range 0.1-15 keV. It consists of three X-ray telescopes each one made of 58 Wolter I mirrors which are nested in a coaxial and confocal configuration (Fig. 1.6). Thus, using more mirrors it reaches an effective area (4300 cm^2 three mirror-assemblies of 1400 cm^2 each) of the imaging spectrometers 4 times that of Chandra, but the focus is not as sharp. The grating spectrometers have twice the Chandra area but half of its spectral resolving power. Each X-ray telescope has a CCD at the focal plane, all supplied by the European Photon Imaging Camera Consortium (EPIC), providing a sensitivity in the range 2-10 keV of $\sim 10^{-7}$ ph/cm^2/s/keV after 10^5 s [82]. The two X-ray observatories, Chandra and XXM-Newton, operating at the same time, are complementary to each other [20].

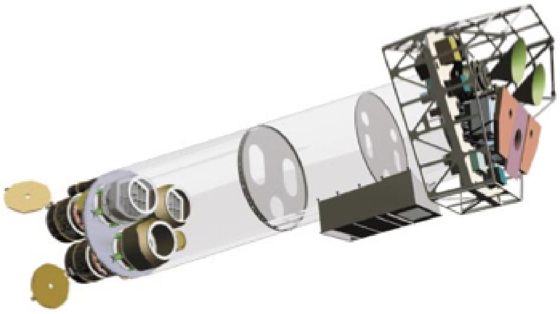

Figure 1.6: An "Open"view of the XMM-Newton observatory. To the left the three mirror modules can be seen, while at the right the back-end of the instrument platform with the focal plane instruments.

1.3 Broadband hard X-ray satellites

In the next section a brief history of the hard X-ray satellite is presented. The main challenge of hard X-/soft gamma-ray spectroscopy is that the signal intensity from the source is usually weaker than detector background. The main causes of the background include diffuse gamma rays and also cosmic rays such as protons and other heavy ions. As we will see, a higher sensitivity is required in this energy band in order to obtain good data even from the weaker sources. Focusing optics are the only way, at present, to overcome this sensitivity limit.

1.3.1 HEAO-1: An all-sky survey

The first High Energy Astronomy Observatory (HEAO-1) was launched on August 1977, carrying four large instruments, all with mechanical collimators. An all-sky survey was first accomplished, then the instruments were pointed at various sources to study spectra and time variability. The principal survey instrument, A1, was a proportional counter array sensitive to energies of 1-20 keV. This produced a catalogue of 842 sources (Fig. 1.7). The A2 detectors covered the energy range 0.2-60 keV. These were designed to measure spectra of sources and in particular of the diffuse background. The A3 experiment was a bench of proportional counters behind modulation collimators. Moderately bright sources could be located with an accuracy of $20''$. The A4 experiment included a phoswich of NaI(TI)/CsI(Na) collimated scintillators with a passband from 13 to 180 keV. The sensitivity of this instrument is 2×10^{-5} ph/cm^2/s/keV, integration time 10^5 s at 30 keV. The sky survey performed with A4 found 70 sources [13].

1.3.2 Rossi XTE: High temporal resolution

The X-ray Timing Explorer (XTE) mission, launched at the end of 1995, was designed for fast X-ray timing in the energy range 2-250 keV. It monitored with millisecond accuracy the emission of hard X ray sources like black holes, neutron stars, X-ray pulsars and X-ray bursts.

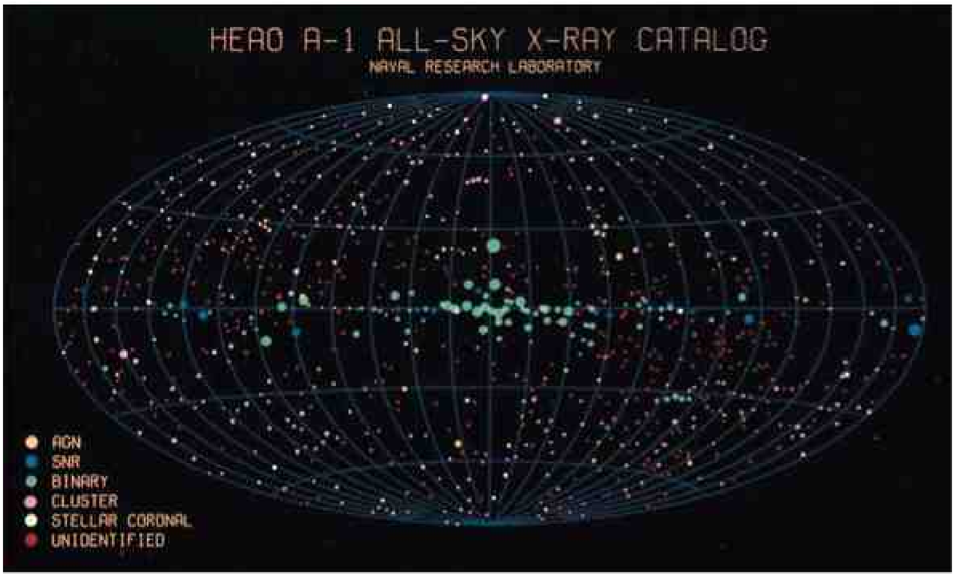

Figure 1.7: Map showing X-ray sources from the HEAO-1 all-sky survey in the energy band 0.5-25 keV. Size of the dot shows the brightness of the source. Colours indicate type of source (from Wood et al., 1984).

The proportional counter array (PCA) was a large collecting area (2-60 keV energy range, 6500 cm^2) and was the most sensitive instrument on the payload. It consisted of five identical methane-xenon-filled proportional counters. Along with the PCA the High-Energy X-ray Timing Experiment, HEXTE (15-250 keV energy range, 2 × 800 cm^2, FOV 1 degree FWHM) is mounted on the payload pointing in the same direction and with the same field of view of the PCA. Both instruments performed high time resolution (1 microsec) monitoring of bright X-ray sources. The time resolution, of course, depended on the source strength. The satellite was capable of measuring photon arrival time to an accuracy of 5 μs. It could observe millisecond fluctuations from stronger sources and variations with durations of hours to days from the fainter ones [76].

A third detector was an All-Sky Monitor (ASM) (2-10 keV energy range, 30 mCrab sensitivity) which was able to scan the whole sky every 1.5 hours. The sky was also scanned for transient sources, such as X-ray novae, whose outbursts are unpredictable.

1.3.3 *Beppo*SAX: Broadband spectroscopy

This was a major Italian program with participation of the Netherlands. Several instruments performed observations over the broad energy band of 0.1-200 keV. It included 2 Wide Field Cameras and Narrow field Instruments (NFI) which were coaligned and pointed with an accuracy of 2 arcsec. A Gamma Ray Burst Monitor was also onboard. The original purpose of the mission was to determine source properties through timing and spectroscopy [17].

The broad energy coverage was designed for an accurate determination of the source spectral parameters. Below 10 keV there were four nested, gold-coated mirror/concentrator that focus on position-sensitive gas scintillation proportional counters. A high-pressure gas scintillation proportional counter, HPGSPC, extended the nominal coverage to 120 keV, and a phoswich scintillation detector, the PDS, recorded photons with energies up to 200 keV. A relevant property of the BeppoSAX scientific payload is the broad overlapping energy response of the various instruments, that will allow cross-calibration of the instruments.

*Beppo*SAX was launched in April 1996 and ended its operational life exactly 6 years later. It accomplished the first observation of a Gamma-Ray Burst (GRB) X-ray afterglow (Fig. 1.8) and monitored the afterglow intensity of many GRB sources [18]. Broadband spectroscopy was obtained for all types of X-ray sources. The *Beppo*SAX most important result achieved was the accurate localization of GRBs, allowing the earth telescopes to quickly point to them in order to find the optical/radio counterparts. Therefore, thanks to its accuracy in determining the GRB coordinates after the burst, the discovery of the so called *Afterglow* was possible. GRBs which before *Beppo*SAX launch were believed to lie within our Galaxy, are now known to be extragalactic objects.

1.3.4 INTEGRAL: A Gamma-ray mission

The International Gamma Ray Astrophysics Laboratory (INTEGRAL), launched in October 2002, is a European Gamma-ray observatory with coverage extending down into the X-ray band. The spacecraft carries three

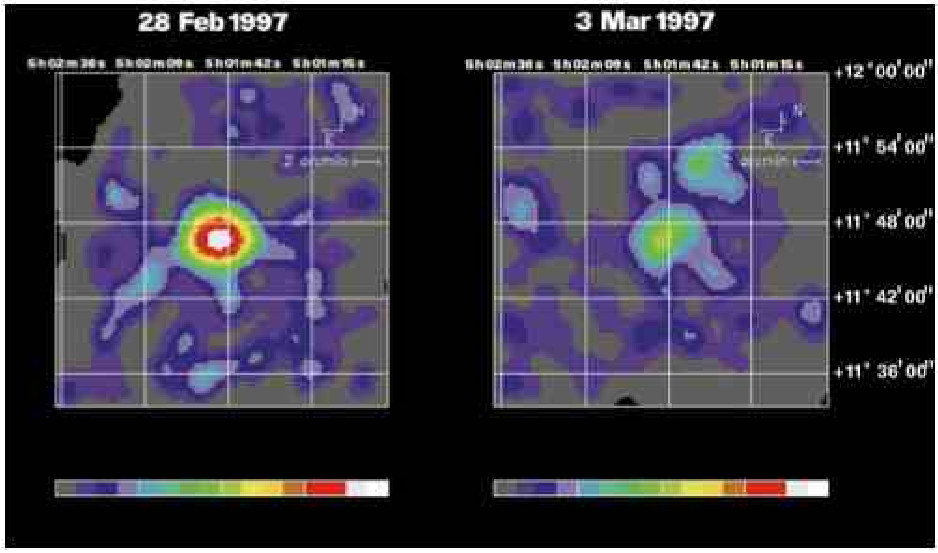

Figure 1.8: False-colour images of the source 1SAX J0501.7+1146, as detected in the error box of GRB970228 with Beppo-SAX Medium Energy Concentrator Spectrometer (2-10keV) during the first and second Target of Opportunity observations (TOO1 and TOO2, respectively). Taking into account the correction for the number of telescopes (one in TOO1 and three in TOO2) and the vignetting in TOO1 due to off-axis pointing, the source faded by a factor of ~ 20 in three days.

imaging instruments via coded masks: the SPI γ-ray spectrometer covers the range 18 keV to 8 MeV, has a 16° field of view with an angular resolution of 2.5° [77]. The detectors are high-purity germanium and have a spectral resolution of 2 keV. The IBIS imager (Fig. 1.9) covers the range 15 keV to 10 MeV and is coaligned with SPI but has a better angular resolution (about 0.2°). The IBIS continuum sensitivity at 100 keV is 2.85×10^{-6} ph/cm^2/s/keV in 10^5 s [83]. The JEM-X telescope provides images with arcminute angular resolution in the 3-35 keV energy band. Thus both high-energy spectra and locations can be obtained for new sources, e.g. transient γ-ray sources [8].

1.3.5 Swift: Fast response for Gamma-ray bursts

The Swift spacecraft, launched in November 2004, is dedicated to the study of Gamma Ray Bursts (GRB). It is designed to prompt detect bursts,

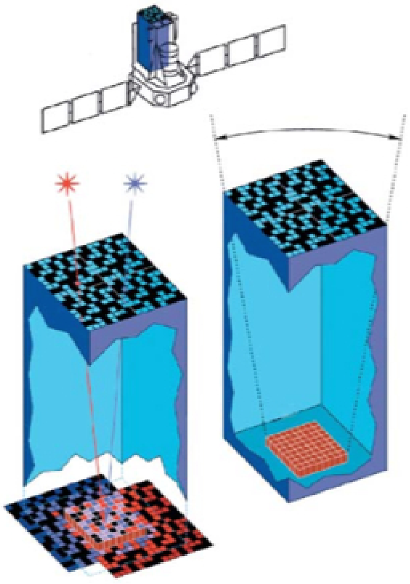

Figure 1.9: The coded mask detector, IBIS, on the Integral spacecraft is shown at the top. At right, the field of view is shown to be determined by the detector and mask dimensions. At left, two sources, red and blue, produce different shadows of the mask on the detector. IBIS images X-rays and γ rays in the range 15 keV to 10 Mev with spatial resolution of $12'$ (ESA/IAS/CEA 2009).

to quickly point instruments at the approximate position so that the accurate location can be measured in X-rays and in the optical band and quickly distributed to the astronomical community. It observes the early fading X-ray and optical afterglow of GRB while it is still relatively bright.

It carries a burst alert telescope (BAT), which locates the position of each event with an accuracy of 1 to 4 arcmin within 15 seconds (energy range 15-150 keV, collecting area 5200 cm^2). This coarse position is immediately relayed to the ground, and some wide-field, rapid-slew ground-based telescopes can catch the GRB with this information. The X-ray telescope (XRT) which can take images and perform spectral analysis of the GRB afterglow in the range 0.2-10 keV (sensitivity $\sim 2 \times 10^{-7}$ ph/cm^2/s/keV in 10^5 s). It uses a Wolter Type I X-ray telescope with 12 nested mirrors with an effective area of 110 cm^2 at 1.5 keV and 5 arcsec angular resolution. The UV/optical telescope (UVOT) is used to detect the optical afterglow (passband 170-600 nm) (Fig. 1.10) providing a sub-arcsec angular resolution ($\sim$ 0.9 arcsec) [21].

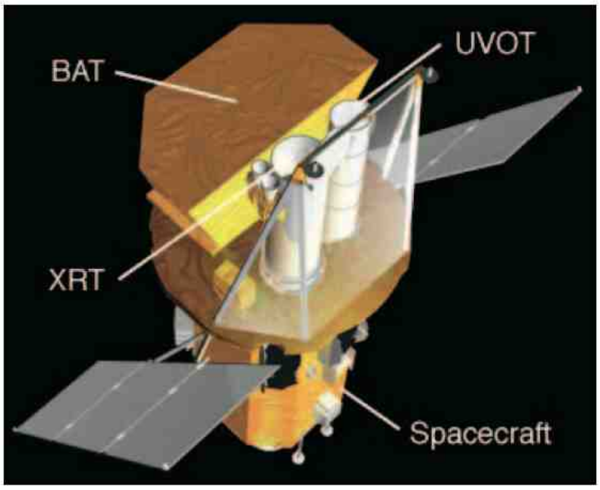

Figure 1.10: The *Swift* satellite with its on board instruments.

1.3.6 NuSTAR: Focusing the high energies

The *Nuclear Spectroscopic Telescope Array (NuSTAR)* mission, launched on 13 June 2012, is the first focusing high-energy X-ray telescope in orbit, as it operates in the band from 3-79 keV. It will observe the sky with an improvement of two order of magnitude in terms of sensitivity, with respect to mechanically collimated or coded instruments. In Figure 1.11 is shown the effective area of NuSTAR, which strongly determines the sensitivity (3×10^{-8} ph/cm^2/s/keV in 10^6 s at 40 keV) [4]. With such a sensitivity the satellite has many scientific objectives including the observation of blazars, the line and continuum from core-collapse supernovae in the Local Group, and also the study of the population of hard X-ray emitting compact objects in our Galaxy (central regions of the Milky Way).

The NuSTAR observatory, (Fig. 1.12), consists of two co-aligned hard X-ray telescopes which focus onto two independent solid-state focal plane detectors. The telescopes are pointed at celestial targets by a three-axis-stabilized spacecraft. The two optics and detectors are designed to be as

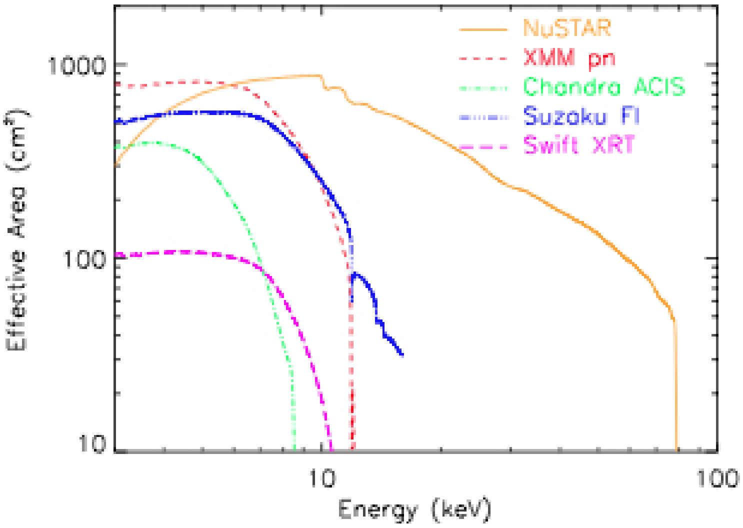

Figure 1.11: Effective collecting area of NuSTAR compared to some operating focusing telescopes. NuSTAR provides good overlap with these soft X-ray observatories, and extends focusing capability up to 79 keV.

identical as possible with each other, so that the focal plane images can be co-added to gain sensitivity. Once the satellite was launched, an extendible mast was deployed to achieve the 10.14 m instrument focal length.

The angular resolution of the telescope is dominated by the optics, with a Half Power Diameter (HPD) of 58 arcsec.

Each telescope has its own focal plane module, consisting of a solid state CdZnTe pixel detector surrounded by a CsI anti-coincidence shield. Its good energy resolution is 400 eV at 10 keV and 0.9 keV at 60 keV. A two-by-two array of detectors provides a 12′ field of view. The NuSTAR observatory, launched in June 2012, is operating nominally on-orbit, with performance fully consistent with pre-launch expectations.

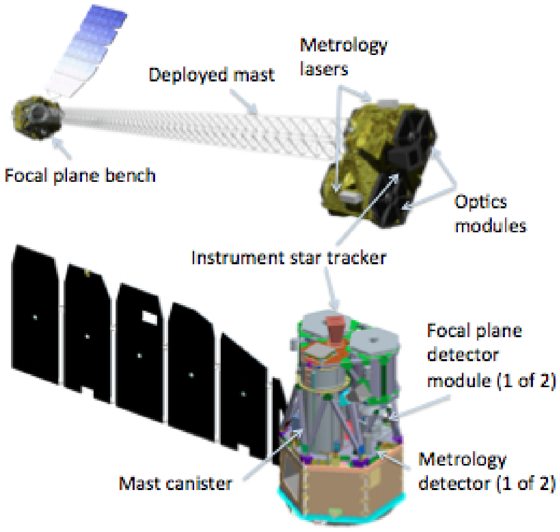

Figure 1.12: Sketch of the observatory in the stowed (bottom) and deployed (top) configurations.

1.4 CLAIRE: The first gamma-ray lens experiment

CLAIRE is a balloon experiment dedicated to validating the concept of a diffraction gamma-ray lens. This new concept for high energy telescopes is very promising and could significantly increase sensitivity and angular resolution above 100 keV. The CLAIRE experiment consists of a 45 cm diameter Laue lens with a 277 cm focal length. Its 556 Ge-Si crystals are tuned to focus 170 keV photons onto a 1.5 cm diameter focal spot [22]. The main goal of the project was to prove the feasibility of a gamma-ray lens to study nuclear lines, providing, thanks to its focusing capability, higher sensitivity than "‘classic"’ gamma-ray telescopes as it will be discussed later.

Laue lenses exploit the coherently interaction between the γ radiation and the internal crystal lattice structure (Bragg diffraction). Every ring of crystals uses a different set of crystalline planes $[hkl]$ in order to focus photons in a single energy band onto a common focal spot. Moreover each crystal is

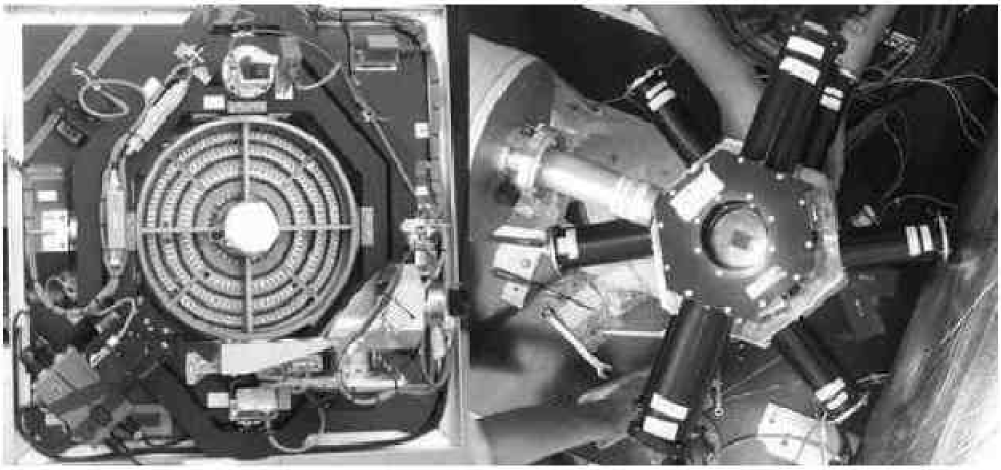

Figure 1.13: The CLAIRE Laue lens (*left*) employed to focus 170 keV energy photons and the 3×3 HP-Ge detector surrounded by the anti-coincidence shield.

oriented in order to obtain the correct diffraction angle, for a given incoming energy, from a source at infinity. On the focal plane a platform helds the detecting system (3×3 detector array, its collimator, electronics, etc.). The γ-ray detector units are made of HPGe cooled by liquid nitrogen (Fig. 1.13).

During a stratospheric balloon flight on 2001 June 14, CLAIRE was pointed to the Crab Nebula for an observation time of 72 min. About 33 photons at 170 keV were detected (Fig. 1.14), in the 3 keV energy band of the lens. Given the Crab flux and the efficiency of the detectors ($\approx$ 60 % at 170 keV), the detection of photons corresponds to a peak efficiency of $\approx$ (7.8 $\pm$ 1.8 %) (i.e. 40 cm^2 effective area). This CLAIRE's efficiency is averaged over the 556 crystals of the lens. Data obtained during the lens tuning indicated that the performance of individual crystals varies strongly from tile to tile.

The flight results basically validated the theoretical models and demonstrated that the γ-ray lens is a useful tool for investigating the nuclear astrophysics [23],[24].

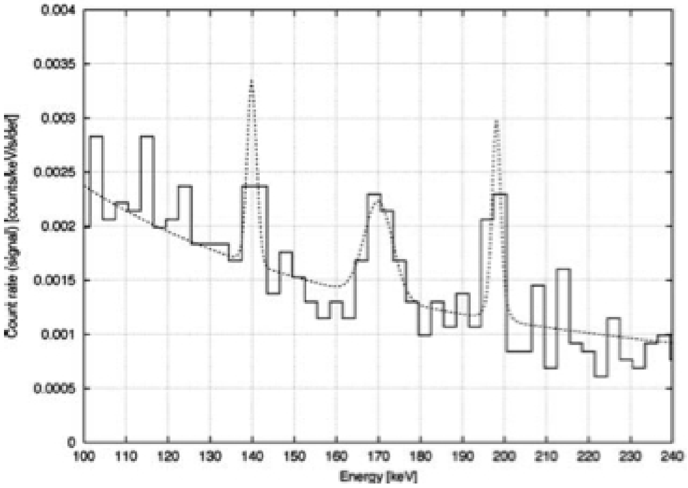

Figure 1.14: Spectrum for single events recorded during time intervals with good Crab pointing: at 170 keV, an excess of 33 photons was detected.

1.5 Astrophysical open issues at high energies (>80 keV)

Most of the visible radiation that we receive from the universe arises from thermal emission processes. Observing the sky in the X-/gamma band, however, the sources are more powerful and the phenomena are far more violent. The universe that we see at these wavelengths is often originated from explosive events and from non-thermal processes that accelerate particles to relativistic energies or synthesize elements of which the universe is composed, through processes still poorly understood.

The telescopes launched so far, can be classified into two categories, based on their capability to focus or not incident photons. At the present time the focusing optics are efficient for energies up to 70 keV, whereas for higher energies the most common technique is the direct view of the sky with a coded mask. To increase the sensitivity by two/three orders of magnitude at these energies, focusing is required. To address the problem of focalization, the best method appears to be the Bragg diffraction in Laue geometry (transmission) (see Sec. 4.6). The availability of focusing optics for energies above 70 keV could allow to face several astrophysical open issues at high energies, thanks to an increase, at least by an order of magnitude, of the telescope sensitivity.

In the next sections I resume some examples of scientific motivations that justify the need of new focusing optics for hard X-rays (Laue lens).

1.5.1 Need of Gamma-ray sensitive observations

Gamma-ray observations above 100 keV allow us to explore the most violent regions of the Universe, revealing the most extreme conditions where compact objects heat matter at temperatures of billions of degrees and the most intense magnetic fields accelerate particles at high energies. The gamma radiation is very penetrating, thus allowing the study of otherwise obscure regions such as parts of the Galactic disk hidden by dense interstellar clouds, or the deep inner regions of the accretion disk of black holes.

As demonstrated by the huge size and weight of the IBIS instrument on board INTEGRAL, achieving significant improvements in the direct-view telescope sensitivity is a rather hard challenge. However the numerous results already obtained with the most recent satellite missions (e.g., $BeppoSAX$, $Rossi-XTE$, $INTEGRAL$) on many classes of X-ray celestial sources, have demonstrated the importance of having a broad energy band in order to understand the Astrophysical phenomena, the knowledge of the radiation production mechanisms, the source nature, the mass accretion geometry.

Although many astrophysical missions have shown excellent performances, none of them has been able to yield detailed spectra above 100 keV. Therefore it is very important to extend the observational window to higher energies together an increased sensitivity, allowing us to study still open issues in the high energy astrophysics.

1.5.2 The galactic disk electron-positron 511 keV emission

Gamma-ray line radiation at 511 keV is the signature of electron-positron annihilation. Such radiation has been known for about 30 years to come from the general direction of the Galactic Centre, but the origin of the positrons has remained a mystery. Although it had long been suspected that electron-positron pair plasmas may exist in X-ray binaries, it was not evident that many of the positrons could escape to lose energy and ultimately annihilate with electrons in the interstellar medium and thus lead to the emission of a narrow 511 keV line. Positron production at this level from 'hard' low mass X-ray binaries (LMXBs) in the Galactic bulge would reduce (and possibly eliminate) the need for more exotic explanations, such as those involving dark matter.

A recent INTEGRAL study of the e^-/e^+ annihilation radiation from the Galactic centre has given new results on the disk component of the 511 keV emission that has important implications for the origin of positrons in the Galaxy [39]. A distinct and surprising asymmetry in its distribution has been observed indeed (Fig. 1.15).

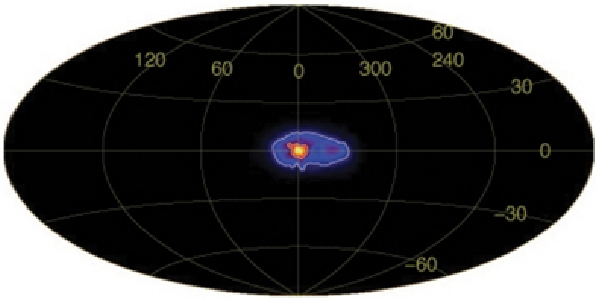

Figure 1.15: A sky map in the 511 keV electron-positron annihilation line.

The asymmetry cannot be due to differences in the column densities of the interstellar medium (ISM) in which the positrons annihilate. Furthermore, spectroscopy of the 511 keV line emission from the two sides of the inner Galactic disk suggests no differences in line shape that might indicate that the flux difference is associated with differing conditions in the ISM. Therefore the annihilation asymmetry is in some way linked to the positron production.

LMXBs containing accreting stellar-mass black holes or neutron stars have been considered as possible candidates for sources of the positrons [39], partly because their concentration towards the Galactic bulge at the time of the observation, is similar to that seen in annihilation line radiation. However the most recent results obtained with INTEGRAL show that this asymmetry is not found in the angular distribution of the LMXB.

With the existing instrumentation, the emission appears to be diffuse; no point sources of annihilation radiation have yet been detected, and no firm conclusion as to the origin of the positrons has been possible because of the limited angular resolution and sensitivity of the current gamma-ray instrumentation. Complications also arise from uncertainties in the distribution of potential positron sources and in the distribution and content of gas. It seems clear that the availability of a more sensitive instrument may represent the opportunity to deeply probe this important open X-ray astrophysical issue.

1.5.3 The origin of the soft gamma-ray background

A step forward in the sensitivity would be also crucial to understand the contribution of different sources to the Cosmic X-ray Background (CXB). The CXB is contributed mainly by active galactic nuclei (AGNs) powered by accreting supermassive black holes at the centers of large galaxies. Optically bright quasars and Seyfert galaxies dominate at low energies (up to a few keV), while obscured AGNs, with $N_H > 10^{24}$-10^{25} cm^{-2}, which outnumber the unobscured one by a factor of 3-4, are responsible for the bulk of the CXB at high energies ($>$10 keV) [42].

In addition, the origin of the cutoff in the CXB spectrum, deduced at energies of beyond 30 keV, can be definitely established only measuring the AGN spectra at hard X-/soft gamma-ray energies.

1.5.4 AGNs physics

The spectrum and spatial distribution of the cosmic X-ray background radiation (CXB) make it possible to obtain important information on the formation and evolution of galaxies, in particular AGNs. In the energy range below 5 keV the radiation is emitted by discrete sources, Seyfert galaxies, whereas above 100 MeV it is observed a high number of blazars, highly fluctuating and very compact energy sources, usually associate a supermassive black holes in the center of the host galaxy, with spectral characteristics similar to those of the extragalactic background.

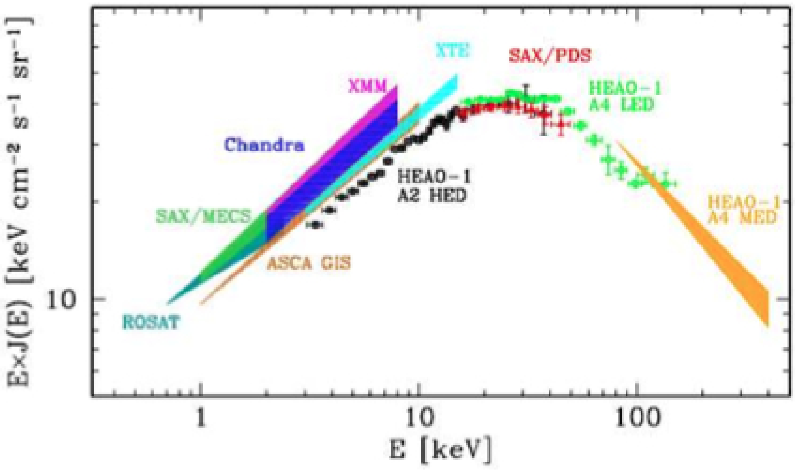

Figure 1.16: CXB spectrum as observed with the PDS experiment on board *BeppoSAX* (*red points*) compared with measurement results obtained with other missions.

The scenario is not so clear in the hard X-/gamma ray range: from 100 keV to MeV the source type to be considered highly depend on the value of the high energy cut-off observed in the spectrum which is still unknown [40]. The overall picture suggests some link with the absence (low energy cut-off) or presence (high energy cut-off) of jets in the various AGN types sampled (Fig. 1.17). This assumption could be rejected or confirmed, with a large sampling and well studied (in terms of sensitivity) AGNs. Moreover, it is important to measure the degree and level of polarization of high-energy photons emitted by the AGNs, since the accretion disks and relativistic jets of blazars are believed to be polarized sources.

It is crucial, therefore, to determine through a more detailed approach and with an increased sensitivity the cut-off at high energies in the spectrum of the AGNs to better understand the physics that feature them. The only way seems to be a mission based on a Laue lens optics.

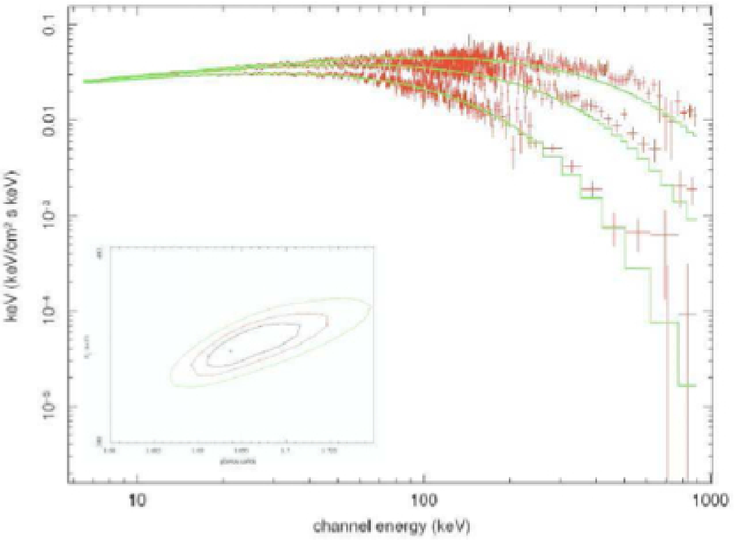

Figure 1.17: Seyfert spectra with different cut-off energies for a flux of 3 mCrab in the 2-10 keV energy range [40].

Chapter 2

Need of more Sensitivity beyond 100 keV

We have seen in the last section that higher sensitivity, beyond 100 keV, is required to study the still open astrophysical issues. At present, only direct view instruments are available at energies higher than 100 keV. In this chapter I will present the comparison between the sensitivity of focusing/non-focusing instruments.

2.1 Direct-view telescopes

Early hard X-ray observations used detectors with simple slat or *honeycomb* collimators to restrict the detector field of view. Rectangular collimators combined with a spinning spacecraft produced the scan of a strip of sky. Width of the strip was determined by the broader size of the collimator cells dimension. The smaller size of the collimator allowed to get the one-dimensional position of the source along the strip. A subsequent scan with different orientation would enable a two-dimensional location of sources on the sky with positional accuracy dependent on the collimator dimension and source strength. A much better angular resolution is obtained using coded mask. In order to significantly improve the angular resolution of coded mask, focusing telescopes are needed.

2.2 Mirrors and focusing telescopes

Low energy X-rays (<100 keV) are reflected from smooth surfaces if the incidence angle is small. If the surface is pretty smooth and the incidence angle <1°, reflection efficiency is close to 1. For a given energy, as the angle is increased, efficiency stays high until a critical angle, θ_c, after which reflection efficiency drops rapidly (as shown in Figure 2.1 for some materials used in current-generation X-ray mirrors). For photon energy E and electron density ρ, then $\theta_c \propto \sqrt{\rho}/E$.

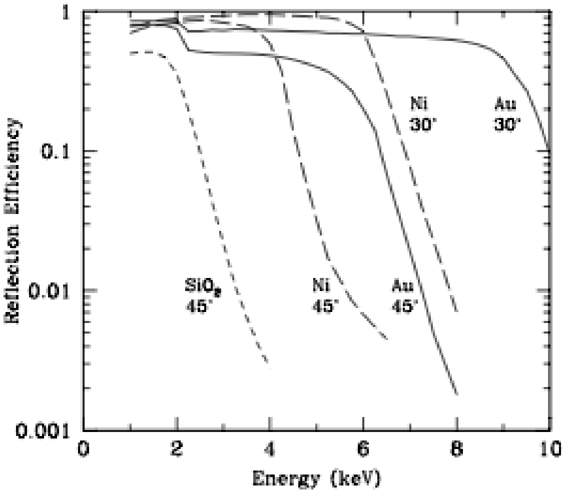

Figure 2.1: Efficiency of X-ray reflection from polished surfaces of quartz (short-dashed line), nickel (long-dashed line) and gold (solid line). Incidence angles are 0.5° (30 arcmin) and 0.75° (45 arcmin) (from Seward, 1977).

In an X-ray telescope, the angle is fixed. As can be seen in Figure 2.1 the reflection efficiency is almost constant until the angle exceeds a certain value, at which the efficiency rapidly falls to low values.

A parabolic mirror surface, with one reflection, will focus a parallel beam of X-rays to a point. Such telescopes have been used to concentrate X-rays onto a small spectrometer. Two reflections, however, are required to produce an image. Imaging geometries were studied by Wolter (1952) for X-ray microscopy. The design usually adopted for a telescope is the Wolter type 1, where X-rays are first reflected from the inside of a parabolic surface and the second reflection is from the inside of a hyperbolic surface (Fig. 2.2).

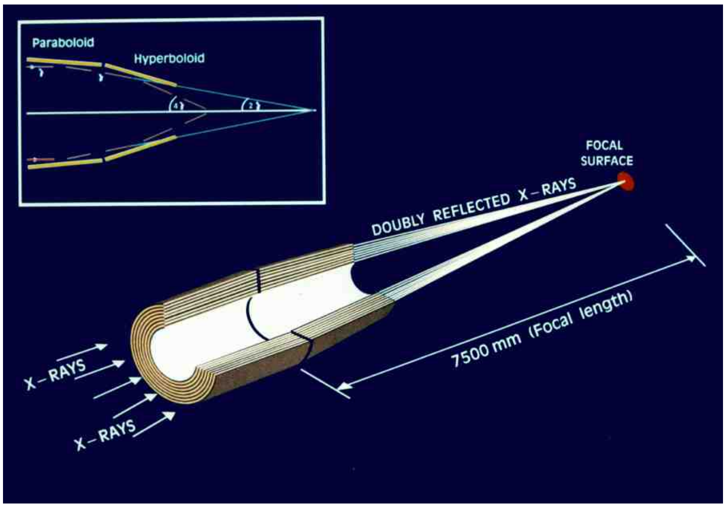

Figure 2.2: The geometry of the NuSTAR mirrors. The shells of varying size are nested tightly together to increase the telescope's effective area.

The on-axis image of a point X-ray source produced by such a telescope consists of a bright core surrounded by a faint, broad halo. The size of the core is determined by the figure of the mirrors, while the broad halo arises from scattering due to small imperfections in the mirrors. The surface brightness distribution of the image of a point source is called the *Point Spread Function* (PSF). A mirror is also characterised by the *Half-Power Radius* (HPR), the radius of a circle containing half of the number of the reflected beam photons.

For most X-ray detectors the major background contribution to the counting rate comes from cosmic rays, solar particles, albedo radiation and primary X-ray background. This background is proportional to the detector area, and limits the detectable signal. A focusing telescope, however, focuses the X-rays onto a small area of the detector, and only the background from this area must be considered.

2.3 Telescope sensitivity

In the following sections, we discuss the sensitivity of direct-view and focusing telescopes to show the advantages of the focusing optics. I consider two cases: the continuum sensitivity of direct-view telescopes and that of focusing telescopes.

2.3.1 Direct-view telescope sensitivity

The source continuum sensitivity of a telescope is defined as the minimum intensity (I^{min}) detectable from an X-ray source in the observation time (Δt).

Given a flux intensity of photons, $I(E)$ $\left[\frac{photons}{cm^2\ s\ keV}\right]$ at energy E, coming from an X-ray source, the number of events, N_{tot}, counted by the detector in the time interval Δt in the energy band ΔE around E can be expressed as the sum of two contributions:

$$N_{tot} = N_S + N_B \tag{2.1}$$

where N_S are counts due to the photons from the X-ray source and N_B are the counts due to the telescope background.

For a direct-view telescope, N_S and N_B are given by:

$$N_s = \epsilon_d S_d \Delta t I\left(E\right) \Delta E, \tag{2.2}$$

$$N_B = S_d \Delta t B\left(E\right) \Delta E, \tag{2.3}$$

where ϵ_d is the detector efficiency, S_d is the detector area and $B(E)$ is the intensity of the measured background spectrum $\left[\frac{counts}{cm^2 skeV}\right]$ at the energy E.

The information on the source is contained in N_S and can be derived subtracting from the total counts the background counts. Therefore, the standard deviation of the counts due to the source is given by:

$$\sigma_{N_S} = \sqrt{\sigma^2_{N_{tot}} + \sigma^2_{N_B}}, \tag{2.4}$$

where $\sigma_{N_{tot}}$ and σ_{N_B} are the standard deviations of N_{tot} and N_B respectively. This expression for $\sigma_{N_{tot}}$ is valid if the flux from the source and from the background are uncorrelated.

With the aim of evaluating the sensitivity, it is assumed that the number of counts is dominated by the background ($N_S \ll N_B$). Using a Poisson statistics, we have $\sigma_{N_{tot}} = \sqrt{N_{tot}}$ and $\sigma_{N_B} = \sqrt{N_B}$, so:

$$\sigma_{N_S} = \sqrt{(N_S + N_B) + N_B} \approx \sqrt{2\sigma_{N_B}^2} = \sqrt{2B(E)S_d\Delta t\Delta E}. \tag{2.5}$$

The confidence level chosen for the sensitivity is generally 99.7% corresponding to a number of standard deviations (n_σ) of 3. Thus:

$$N_S^{min} = \epsilon_d S_d \Delta t I^{min}(E)\Delta E = 3\sqrt{2B(E)S_d\Delta t\Delta E} \tag{2.6}$$

from which:

$$I^{min} = \frac{3}{\epsilon_d}\sqrt{\frac{2B(E)}{S_d\Delta t\Delta E}}. \tag{2.7}$$

More in general the ratio between the source signal and its error is given by:

$$n_\sigma = \frac{N_S}{\Delta N_S} = \frac{\epsilon_d I S_r \Delta t\Delta E}{\sqrt{2BS_r\Delta t\Delta E}}. \tag{2.8}$$

Therefore, the sensitivity of a direct-view telescope at a confidence level corresponding to n_σ is given by:

$$I^{min} = \frac{n_\sigma}{\epsilon_d}\sqrt{\frac{2B}{S_d\Delta t\Delta E}}. \tag{2.9}$$

The easiest, and also exploited, way to improve the instrument sensitivity is to decrease the background and to increase the value of the detector area S_d. However the sensitivity dependence on $\sqrt{S_d}$ implies that the minimum detectable intensity decreases by a factor 10 when the detector surface increases of a factor 100.

2.3.2 Focusing telescope sensitivity

The situation changes radically for a focusing telescope. In this case, while the background counts remain those of Eq. (2.3), the number of counts due to the source is affected by the focusing optics and becomes:

$$N_S = \epsilon_d(E)\epsilon_f(E)S_{eff}(E)\Delta t I(E)\Delta E, \tag{2.10}$$

where ϵ_f is the fraction of photons inside the surface sector S_d of the focal plane detector, and S_{eff}(E) is the effective area of the optics at the energy E. This quantity, of key importance, is the product of the geometrical area of the optics projected onto the focal plane times its reflection efficiency at the energy E.

With this newly defined value for N_S and following the same steps that lead to Eq. (2.9), it is possible to obtain the sensitivity of a focusing telescope (I^{min}) at a confidence level corresponding to n_σ:

$$I^{min}(E) = \frac{n_\sigma}{\epsilon_d(E)\epsilon_f(E)S_{eff}(E)}\sqrt{\frac{2BS_d}{\Delta t\Delta E}}. \tag{2.11}$$

It is worth pointing out that in this case the minimum detectable flux is inversely proportional to the effective area of the focusing optics. S_d is in general very small providing a very narrow PSF. Thus I^{min} is also decreased by the low S_d. In addition it depends on the effective area of the optics like S_{eff}^{-1} vs. $I^{min} \propto S_d^{-0.5}$ in the case of direct-view telescopes. Unfortunately the lack of focusing optics for gamma-ray photons with energy greater than 10 keV has compelled astronomers to build direct-view telescopes with overgrowing size.

Figure 2.3 shows the sensitivity of some of the missions discussed in the previous chapter, along with Laue lens expected sensitivity. Focusing telescopes like NuSTAR have already improved sensitivity with respect to the past satellites, but for energies beyond 100 keV where multilayer optics are not efficient, Laue lenses appear to be the best solution.

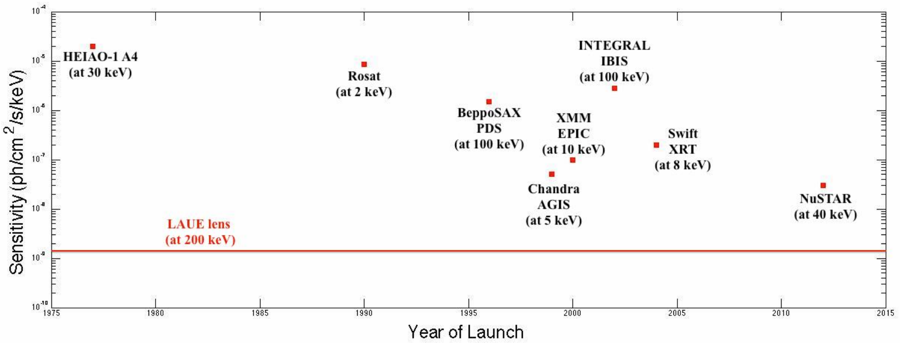

Figure 2.3: Sensitivity of some of the important missions over the years. Observation time 10^5 s.

Chapter 3

Introduction to γ-ray Detection

In this chapter I give an introduction to the gamma-ray detectors, focusing in particular on detectors employed for the measurements shown in this thesis. One of them is cooled Ge detector to perform spectroscopy measurements; the other is NaI(Tl) scintillator to monitor the incident beam; the third is CsI(Na) scintillator used as an X-ray imager.

3.1 Solid state detector

The solid state (semiconductor) detectors are based on the atoms ionisation of the detector material generated by the incoming X-ray, producing a number of electron-hole pairs (Fig. 3.1). The collection of the produced charge is possible thanks to the very low working temperatures ($\sim$ -193 °C) so that thermal noise can be significantly reduced. The number of electrons produced by the passage of radiation is much higher than in the gas proportional counters.

The functioning of all present-day semiconductor detectors depends on the formation of a semiconductor *junction*, known also as a rectifying diode. Semiconductor diodes can be formed in a number of ways. A simple configuration used for illustration purposes is the *pn* junction formed by the juxtaposition of a p-type semiconductor with an n-type material. These junctions, of course, cannot be obtained by simply pressing n- and p-type materials together. Special techniques must be used to achieve the intimate

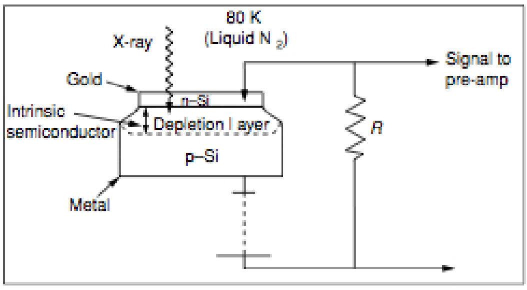

Figure 3.1: Diagram of a solid state spectrometer (SSS)

contact necessary for junction formation. The formation of a pn-junction creates a special zone at the interface between the two materials. Because of the difference in the concentration of e- and holes between the two materials, there is an initial diffusion of holes towards the n-region and a similar diffusion of electrons towards the p region. An electric field gradient across the junction is created due to the different charge of the regions, which eventually halts the diffusion process leaving a region of immobile space charge. Because of the electric field, there is a potential difference across the junction, known as the *contact potential*. The region of changing potential is known as the *depletion zone* and has the special property of being empty of all mobile charge carriers (Fig. 3.2).

Special solid state detectors can be assembled in arrays of $\sim 10^6$ detectors (CCDs), called pixels, making them the primary choice for the astronomical missions of the 2 last decades. When an X-ray is absorbed in a pixel, a charge proportional to the photon energy is deposited there. At the end of the recording interval, the device is read out one row at a time by circuitry at one edge of the chip. After the first row is read out, charge in all pixels is shifted down one row and the second row is read out. This charge-transfer clocking process takes 0.04 s to read 1024 rows [25].

The response of semiconductors is linear with energy. If E is the energy of the radiation then $n = E/w$ electron-hole pairs are created, where w is the average energy for pair creation. Assuming a collection efficiency ϵ, then a charge $Q = \epsilon\ eE/w$ is collected on the electrodes. If the depletion region has a capacitance C, the observed voltage on the electrodes is given by:

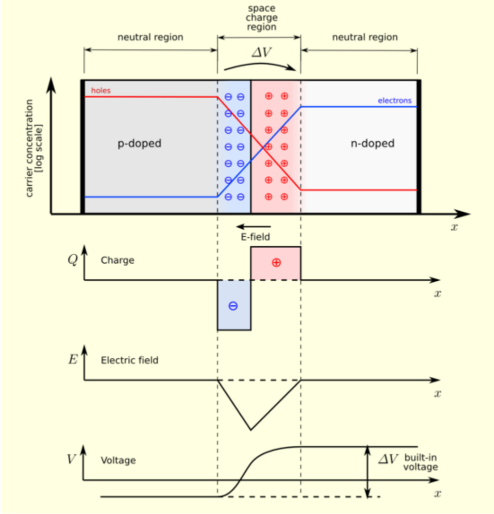

Figure 3.2: A scheme of a semiconductor p-n junction.

$$V = \frac{Q}{C} = \varepsilon \frac{eE}{wC}. \tag{3.1}$$

A small fluctuating current usually flows through semiconductor junctions when voltage is applied. This current appears as noise at the detector output and sets a limit on the smallest signal pulse height which can be measured. The leakage current has several sources:

- **A.** The movement of minority carriers, i.e., holes from the n-region which are attracted across the junction to the p-side and electrons from the p-region which are similarly attracted to the opposite side.
- **B.** Thermally generated e-h pairs originating from recombination and trapping in the depletion region.
- **C.** The largest source of leakage current is through surface channels. This component is complex and depends on many factors including the surface chemistry, the existence of contaminants, the surrounding atmosphere, the type of mounting, etc.

Temperature plays an important role on the conductivity of the detector. Ge detectors must always be operated at low temperatures (~ -190 °C) otherwise the high leakage current will cause irreversible damage to the crystal. Decreasing the temperature normally greatly reduces noise.

Because of the small signals obtained from semiconductor detectors, care must be taken to use low-noise electronics for signal processing. In particular, a preamplification is necessary before any further treatment can be made. A preamplifier is the first component in a signal processing chain of a radiation detector. The charge created within a detector is collected by the preamp. In spite of its name, the preamp does not amplify any signal, but acts as an interface between the detector and the pulse processing electronics that follows. The main function of a preamplifier is to extract the signal from the detector without significantly degrading the intrinsic signal-to-noise ratio.

The main advantage of the semiconductors with respect the other types of detectors, is that the energy required to create an electron-hole pair is $\sim$10 times smaller than that required for gas ionization. Thus the produced charge for a given energy is an order of magnitude greater resulting in increased energy resolution.

3.2 Instrumental effects introduced by detector

In gamma-ray spectroscopy applications, the detectors produce output pulses whose magnitudes are proportional to the energy deposited in the detecting medium by the incident photons. Regardless of the type of detector used, the measured spectra have many features in common, and in this section I will give a brief description of them.

3.2.1 Generic detector response

In figure 3.3(a) it is shown the spectrum of a monoenergetic gamma-ray source of energy E_0, which could be, for example, the gamma-ray line produced by a decaying nucleus. Since detected gamma-ray photons do not usually come from free nuclei but are emitted in material media, some of them may undergo scattering before they emerge from the radioactive sample. This scattering leaves the affected photons with slightly less energy than E, and the energy spectrum of photons emitted from a material sample is slightly broadened into energies below E$_0$ as shown in Figure 3.3(b).

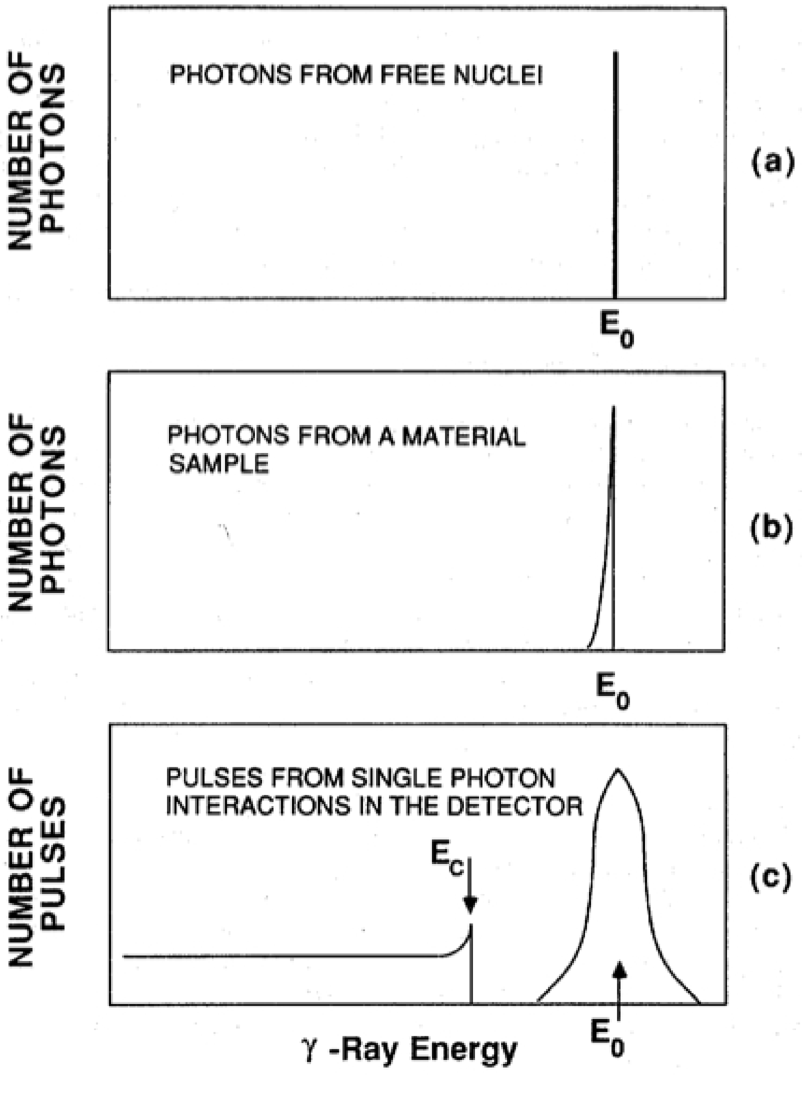

Figure 3.3: An idealization of the photon spectrum (a) produced by free nuclei, (b) emerging from a material sample, and (c) displayed from interactions in a detecting medium.

When the gamma ray enters the detection medium, it transfers part or all of its energy to an atomic electron, expelling the electron from its atomic shell. This free electron then usually transfers its kinetic energy, in a series of collisions, to other atomic electrons in the detector medium.

A photoelectric interaction transfers all of the incident photon's energy to a photoelectron; this electron subsequenty causes multiple ionizations until its energy is depleted. The amount of charge produced from this type of event is therefore proportional to the actual photon energy. The Compton scattering interaction, dominant in the energy range 0.2-10 Mev, transfers only part of the incident photon's energy to an ionized electron, and that electron subsequently causes ionizations until its energy is depleted. The amount of charge produced from this type of event is proportional to the partial energy originally lost by the incident photon but conveys partial information about the actual photon energy. Multiple Compton scattering events for a single photon can produce amounts of charge closer to the value representing the full energy of the original photon. The idealized detector response to the photoelectric and Compton interactions in the detection medium is shown in Figure 3.3(c). The maximum energy that can be deposited in the detection medium from a Compton scattering event comes from an event where the photon is back-scattered. The Compton-generated detector pulses are therefore distributed below this maximum energy [E_c in Figure 3.3(c)].

The full-energy peak in Figure 3.3(c) is significantly broadened by the statistical fluctuation in the number of charges produced by the photoelectron. This effect is the primary contributor to the width of the full-energy peak and is therefore the dominant factor in the detector energy resolution.

3.2.2 Detector resolution

The resolution of a detector is a measure of its ability to resolve two lines that are close in energy. The parameter used to specify the detector resolution is the Full Width of the (full-energy) photopeak at Half its Maximum height (FWHM). If a standard Gaussian shape is assumed for the photopeak, the FWHM is given by:

$$FWHM = 2\sigma\sqrt{\ln 2} \tag{3.2}$$

where σ is the width parameter for the Gaussian. High resolution (small FWHM) makes individual definition of close-lying peaks easier, and it is desirable to have it the best possible.

There are both natural and technological limits how precisely the energy of a gamma-ray detection event can be registered by the detection system. The natural limit on the energy precision arises primarily from the statistical fluctuations associated with the charge production processes in the detector medium. The resolution can also be affected by electronic effects, such as noise, pulse pileup, etc.

3.2.3 HPGe cooled detectors and NaI(Tl) scintillator detectors

The two types of detectors that are most widely used in gamma-ray applications are NaI(Tl) scintillation detectors and the Germanium solid-state detectors. These detectors are among those used for the Laue lens development discussed in this thesis. NaI detectors generate full-energy peaks that are much wider than those obtained from the Germanium detectors. This is shown in Figure 3.4, where it can be seen that the number of details in the germanium spectrum, from a plutonium gamma-ray source, is higher than in the corresponding NaI spectrum.

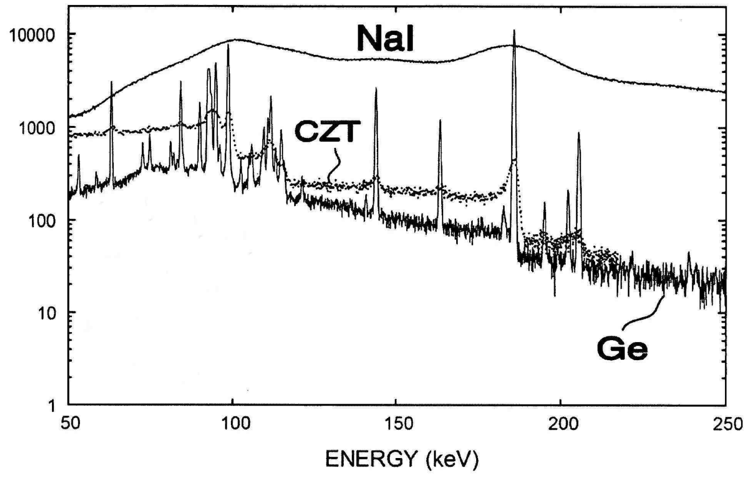

Figure 3.4: Gamma-ray spectrum, taken with a high-resolution solid-state detector HPGe, CZT and NaI scintillation counter. Gamma-ray energies are given in keV.

As above discussed this is due to the different energy resolution. Indeed, in X-ray detectors the number of electron charges n, produced by the primary detection event, depends upon the total energy deposited E and the average amount of energy required to produce an electron-ion pair (δ):

$$n = E/\delta \tag{3.3}$$

where n is mainly governed by Poisson statistics, and the random statistical variance in n is the primary source of fluctuation in the full-energy pulse amplitude. However, for detector types, like solid state detectors, this statistical variance is found to be smaller than that expected assuming a Poisson statistics, by a factor known as the Fano factor [26]:

$$\sigma^2 (n) = Fn = FE/\delta \tag{3.4}$$

This effect comes from the fact that the processes which give rise to the formation of the charge carriers are not independent. Therefore the total number of charge carriers cannot be described through the Poisson statistics, and we get:

$$\Delta E_{stat}/E = 2.35\sigma (n) /n = 2.35[F\delta/E]^{1/2} \tag{3.5}$$

The electronic contribution to the energy fluctuations (ΔE_{elect}) is essentially independent of photon energy and determined largely by the detector capacitance and preamplifier. Thus, the total energy resolution can be expressed as the combination of the electronic and statistical effects:

$$\Delta^2 E_{tot} = \Delta^2 E_{elect} + \Delta^2 E_{stat} = \alpha + \beta E \tag{3.6}$$

In Figure 3.5 the energy resolutions of scintillation, gas, and solid-state detectors are compared [27].

The scintillation efficiency is the main factor influencing the number of electrons produced at the photocathode of a scintillation detector. Other factors, such as scintillator transparency, play important roles [25].

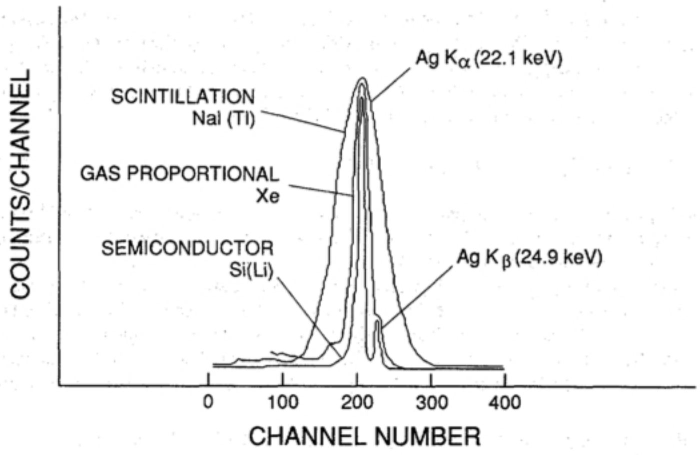

Figure 3.5: Resolution comparison among NaI scintillation, gas proportional, and Si(Li) semiconductor detectors for the primary X-rays of silver.

3.2.4 Pile-up and dead time

One of the most common problems regarding the X-ray detectors is the *pile-up* effect. If the source is bright and the focus sharp, there can be two or more interactions in a single pixel during the recording interval. This charge is recorded as a single event having the summed energy of the interacting photons. As a consequence of this effect a distortion in the spectrum appears. A very bright source will deposit many X-rays in a few central pixels during each recording cycle, and the charge can be so large that the event is rejected. Generally pile-up involves the superposition of pulses on the long-duration tail or undershoot from a preceding pulse. Tails or undershoots can persist for relatively long periods of time so that tail pile-up can be significant even at relatively low counting rates. The effect on the measurements is to worsen the resolution by adding wings to the recorded peaks in the pulse height spectra as shown in the Figure 3.6.

In all detector systems, there is a minimum amount of time that must separate two events in order that they can be recorded as two separate pulses. Usually the limiting time is set by the electronics or may arise in the detector itself. This minimum time separation is called *dead time*. Therefore there will be always some probability that a true event is lost because it occurs too

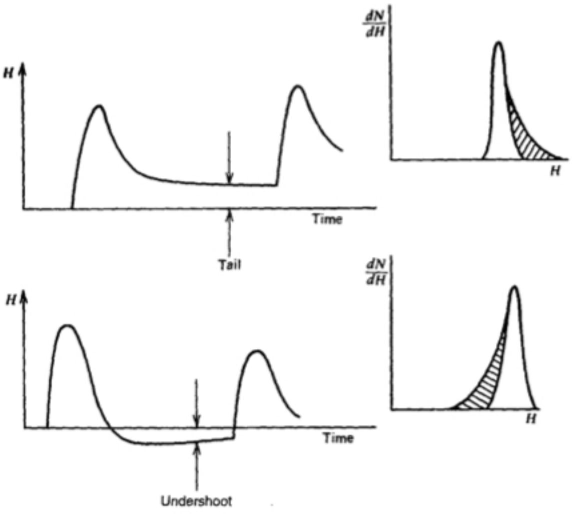

Figure 3.6: Pile-up from the tail or undershoot of a preceding pulse.

quickly following a preceding event. Also in this case the dead time losses can become rather severe when high counting rates occur, and some correction for these losses must be considered.

3.3 The MultiChannel pulse-height Analyzer (MCA)

The Multichannel Pulse-Height Analyzer is the primary tool used in X-ray spectroscopy to record the energy or time spectra available from high-energy radiation detectors. It is often called as MCA (MultiChannel Analyzer).

The basic function of the MCA is the following. Assuming the case of a detector which offers a linear response to the energy of gamma rays, as we have previously seen, it produces a pulse of electrical charge for every gamma-ray photon that is detected. In simplest terms, the amount of charge in the pulse produced by the detector is proportional to the energy of the photon. The preamplifier collects that charge, while adding as little noise as possible, converts the charge into a voltage pulse, and transmits the result to the supporting amplifier. The amplifier applies low-pass and high-pass filters to the signal to improve the signal-to-noise ratio, and increases the amplitude of the pulse. At the output of the amplifier, each pulse has a duration of the order of microseconds, and an amplitude or pulse height that is proportional to the energy of the detected photon. Measuring that pulse height reveals the energy of the photon. Rating the number of pulses of each height detected over a period of time gives the energy spectrum of the detected gamma-rays.

All the pulses coming from the amplifier are sent to an Analog-to-Digital Converter (ADC) to be coded as a digital representation of the analog voltage. Essentially, the ADC compares the analog pulse height to a ladder of voltage levels. The ladder extends from 0 to 10 V with a uniform space between the rungs. Each rung represents a defined voltage. The intervals between rungs are numbered from zero to N_{max}. If the pulse falls in the N^{th} space between rungs, one count is added to the existing counts in the N^{th} memory location of the histogramming memory. Once the analysis of the pulse is completed, the MCA opens its linear gate and waits for the next available pulse to arrive. The process is repeated on a pulse-by-pulse basis over the counting time established by the instrument operator. At the end of the counting time, the histogramming memory contains a record of counts versus memory location.

The data in the histogramming memory represent the spectrum broke up into discrete, digital intervals. These intervals are typically called channels.

MCAs that are supported by computers generally use the computer to display the spectrum, analyze the spectral content and select the operating parameters for the MCA. Because the channel number is proportional to the energy of the gamma ray (to first order), the horizontal scale can be calibrated to read in the appropriate units of energy (Fig. 3.7) [29].

3.4 X-ray imaging detector for Laue lens development

An X-ray imaging unit is available in the LARIX facility of the University of Ferrara to be used for the Laue lens development. In the following section I will describe its features and the working principle. The Thales TH 59432HD is a high-definition imaging X-ray detector. The unit is constituted by an image intensifier (X-Ray Image Intensifier, XRII) coupled to a high-resolution

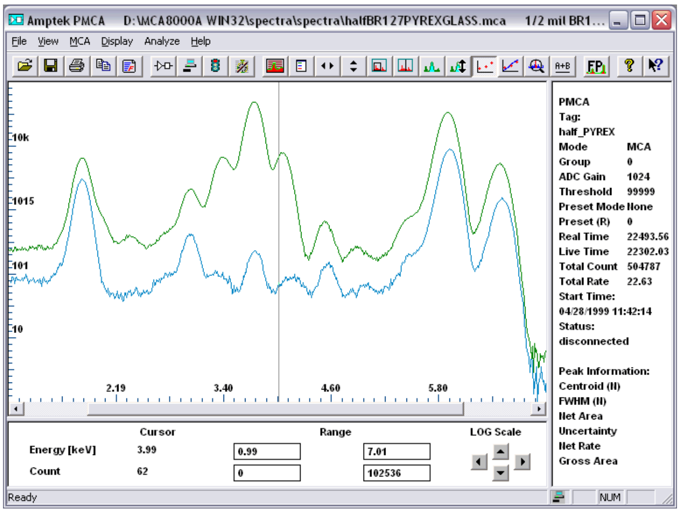

PMCA
Tag:
half_PYREX
Mode MCA
Group 0
ADC Gain 1024
Threshold 99999
Preset Mode None
Preset (R) 0
Real Time 22493.56
Live Time 22302.03
Total Count 504787
Total Rate 22.63
Start Time:
04/28/1999 11:42:14
Status:
disconnected

Peak Information:
Centroid (N)
FWHM (N)
Net Area
Uncertainty
Net Rate
Gross Area

	Cursor	Range	
Energy [keV]	3.99	0.99	7.01
Count	62	0	102536

Figure 3.7: Typical MCA windows Software showing multiple spectra.

CCD through an optical compact system that includes a motorized iris, a neutral density filter (NDF), and a photodiode (Fig. 3.8).

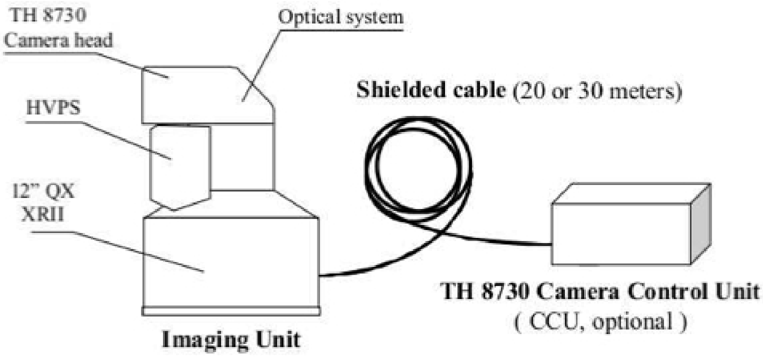

Figure 3.8: Diagram of the Thales internal structure.

The XRII is made up of a entry window, a CsI(Na) scintillator, a photocathode, several electrostatic focussing lenses, an anode and an output screen (Fig. 3.9). The X-ray entrance window is part of a box that maintains the XRII under vacuum. It is made of aluminum (thickness about 1 mm) with a convex shape in order to maximize the size of the input area (nominally 320 mm in diameter) and to better resist the atmospheric pressure. Immediately behind the window there is a CsI(Na) scintillator. Thanks to this scintillator, the X-ray photons incident on the X-ray imager are turned into photons of visible light. The scintillator should be thick enough to absorb the majority of the incident X-radiation, but also sufficiently thin because in the case of too many photons it would cause their diffusion from the fluorescent side screen, producing a significant degradation of the spatial resolution. In our case the thickness is of 450 μm. Coupled to the scintillator there is a 20 nm thick $SbCs_3$ photocathode, with efficiency equal to 10% -15% [78].

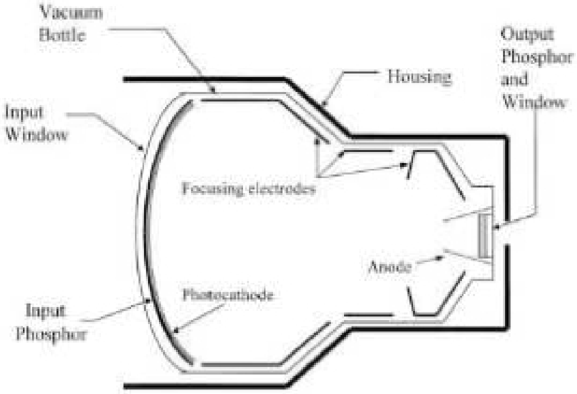

Figure 3.9: XRII outline.

The importance of using the Cesium Iodide scintillator is in the fact that this material has the fundamental property of being made up of needle-shaped crystals (Fig. 3.10): the long and thin crystalline columns act as light guides which direct the visible light emitted from inside them to the photocathode with a minimal lateral dispersion.

Just behind the photocathode, is positioned a system of collimating lenses that focus the electrons coming from the photocathode to the anode. In this way the size of the electron beam is made comparable (diameter $\sim$ 25 mm) to that of the fluorescent screen output (P20). The screen is a layer of ZnCdS(Ag) which has a green emission spectrum ($\sim$ 530 nm) and it is very thin (4-8 μm). At this stage the number of photoelectrons is not increased, but care must be taken to maintain stable the high voltage of electrodes to

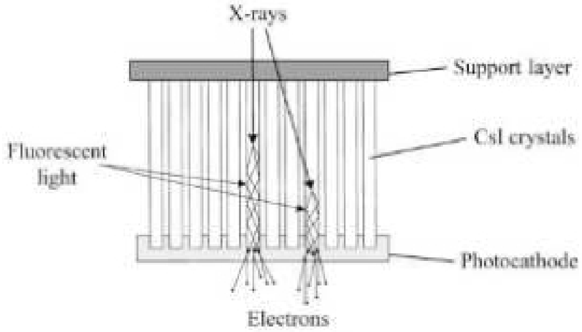

Figure 3.10: Diagram of the CsI crystal structure.

avoid distortion in the output image [79].

The optical system is positioned between the XRII and the CCD, and its task is to transfer the output signal from the detector to the CCD camera (Fig. 3.11). After the exit window of the image intensifier there are collimating lenses which direct the light beam outgoing from XRII towards the focal plane where a CCD is placed. At half of this section there is a semi-reflective mirror which allows to direct the light signal towards both the CCD and an apparatus for the measurement of light in real time (at the top in Figure 3.11), which uses a photodiode (HAMAMATSU S2387-66R) to provide a current proportional to the incident light. The signal that goes in the direction of the CCD, meets at this point a motorized iris. The iris operates in a mechanical way (by increasing or decreasing the diameter of the hole) the quantities of photons arriving at the CCD. This component of the optical system can be managed remotely using a special software.

The CCD camera has a progressive scan readout. It has an active area of 13.1×13.1 mm^2 and the number of active pixels is 1024×1024 with dimension of each pixel of 12.8×12.8 μm^2. It has an operation mode that can vary from the 15 to 60 progressive frames per second. The efficiency at 540 nm is 30%. The output of the CCD provides 12-bit digital images with the possibility to obtain continuous images, pulsed or single. The maximum time of integration reached by external trigger is 2 sec. Thanks to the very low current ($2n$A/cm^2), the detector does not need a external cooling system.

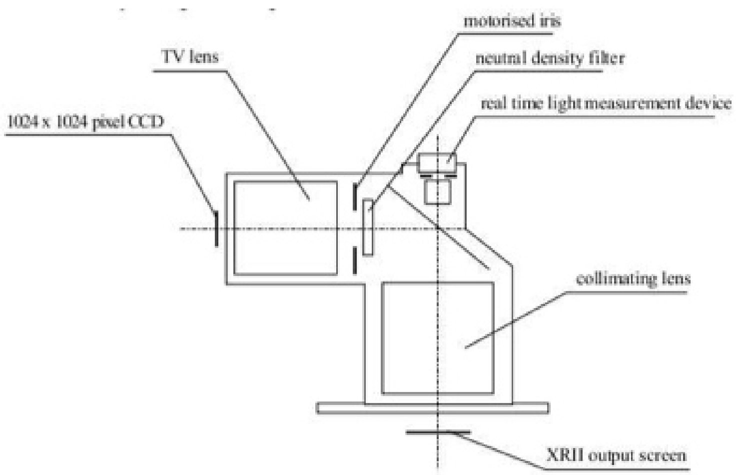

Figure 3.11: Optical system scheme.

The image intensifier has a spatial resolution of 300 μm, efficiency detection of 79% at 60 keV and 32% at 100keV.

Chapter 4

X-ray Diffraction and Laue Lens Concept

In 1912 the German physicist von Laue claimed that, if crystals were composed of regularly spaced atoms which might act as scattering centers for X-rays, and if X-rays were electromagnetic waves of wavelength about equal to the interatomic distance in crystals, then it should be possible to diffract X-rays by means of crystals.

This chapter is devoted to introduce the theory which drives the diffraction of X-rays by crystals. Two crystal models are presented: the first concernes the diffraction from flat crystals and the second concerns crystals with bent diffractive planes. I will also introduce the Laue lens concept.

4.1 The crystal geometry

A crystal may be defined as a solid composed of atoms arranged in a pattern periodic in three dimensions. Crystals differ in a fundamental way from gases and liquids because the atomic arrangements in the latter do not possess the essential requirement of periodicity. However, not all solids are crystalline, some are *amorphous*, like glass, and do not have any regular interior arrangement of atoms.

In thinking about crystals, it is often convenient to ignore the actual atoms composing the crystal and their periodic arrangement in space, and to think instead of a set of imaginary points which has a fixed relation in space to the atoms of the crystal. A set of points arranged in such a way that each point has identical surroundings constitutes a *point lattice*. "Identical surroundings" means that the lattice of points, when viewed in a particular direction from a lattice point, would have exactly the same appearance when viewed in the same direction from any other lattice point (Fig. 4.1). Since all the cells of the lattice shown in Figure 4.1 are identical, we may choose anyone as a *unit cell*.

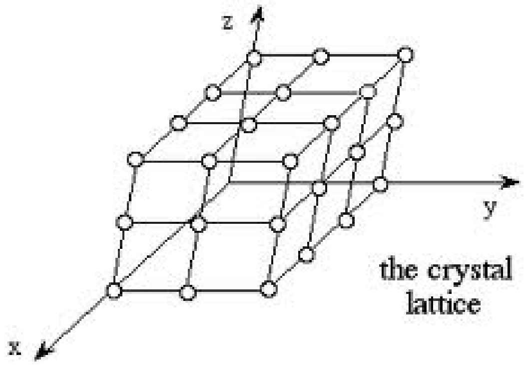

Figure 4.1: A point lattice.

The orientation of planes in a lattice may be represented using a system popularized by the English crystallographer Miller. Generally the orientation of the given plane is obtained by giving the actual distances, measured from the origin, at which it intercepts the three axes. Such coordinates are related to the *Miller indices hkl*), which are defined as the reciprocals of the fractional intercepts which the plane makes with the crystallographic axes. For example, if the Miller indices of a plane are (hkl), then the plane makes fractional intercepts of $1/h$, $1/k$, $1/l$ with the axes. Therefore if a plane is parallel to a given axis, its fractional intercept on that axis is taken as infinity and the corresponding Miller index is zero.

4.2 Crystal diffraction

Diffraction is due essentially to the existence of certain phase relations between two or more waves. Two polarized electromagnetic waves are said to be completely in phase if their electric-field vectors have the same magnitude and direction at the same instant at any point measured along the direction of propagation of the wave. A $wave\ front$ is a surface perpendicular to this direction of propagation.

Without going into details it may be asserted that two rays are completely in phase whenever their path lengths differ either by zero or by a integer number of wavelengths. Differences in the path length of various rays arise quite naturally when we consider how a crystal diffracts X-rays. Figure 4.2 shows a section of a crystal with its atoms arranged on a set of parallel planes A, B, C, normal to the plane of the sheet and spaced a distance d apart. Let us assume a beam of perfectly parallel, monochromatic X-rays of wavelength λ which is incident on this crystal at an angle θ, where θ is measured between the incident beam and the particular crystal planes under consideration. A diffracted beam is defined as a beam composed of a large number of scattered rays mutually in phase. We can imagine a diffracted beam as being built up of rays scattered by successive planes of atoms within the crystal. Therefore, diffraction is essentially a scattering phenomenon in which a large number of atoms cooperate. Since the atoms are arranged periodically on a lattice, the rays scattered have definite phase relations between them.

4.2.1 The Bragg law

It is worth remembering two geometrical considerations:

- The incident beam, the normal to the reflecting plane, and the diffracted beam are always coplanar.
- The angle between the diffracted beam and the transmitted beam is always 2θ. This is known as the diffraction angle.

As already mentioned, diffraction in general occurs only when the wavelength of the wave motion is of the same order of magnitude as the repeat

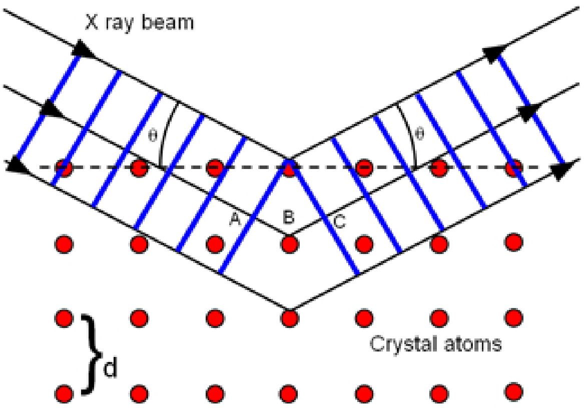

Figure 4.2: Diffraction by a crystal.

distance between scattering centers. From Figure 4.2, it can be easily shown that scattered rays are in phase if:

$$n\lambda = 2d \sin\theta. \tag{4.1}$$

where n is an integer number that gives the diffraction order and d is the lattice distance. This is the Bragg law. For diffraction, the smallest value of n is 1 ($n = 0$ corresponds to the beam diffracted in the same direction as the transmitted beam) and if λ is very small, the diffraction angles are too small to be conveniently measured. Eq. (4.1) is equivalent to the following:

$$2d_{hkl} \sin\theta_B = n\frac{hc}{E}, \tag{4.2}$$

where d_{hkl} is the lattice distance relative to the Miller indices hkl, c is the speed of light and h the Planck constant.

4.3 Mosaic crystals

Mosaic crystals are a kind of crystals which have a degree of imperfection known as *mosaic structure* whose effect on diffraction phenomena is quite noticeable. It is a kind of substructure by which a "single" crystal is broken up into a number of many tiny perfect crystals (*crystallites*) each slightly misaligned one from another (Fig. 4.3). Usually the blocks are oriented around a mean direction and their size is of the order of μm. The maximum angle of misalignment between them may vary from a very small value to as much as one degree, depending on the crystal. If this angle is δ, then diffraction of a parallel monochromatic beam from a "single" crystal will occur not only at an angle of incidence θ_B but at all angles between θ_B and $\theta_B + \delta$.

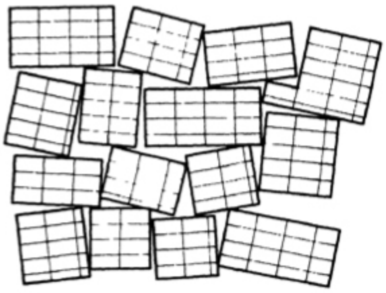

Figure 4.3: The mosaic structure of a real crystal.

The distribution function of the crystallite misalignments from the mean direction can be approximated by a Gaussian function:

$$W(\delta) = \frac{1}{\sqrt{2\pi}\eta} \exp\left(-\frac{\delta^2}{2\eta^2}\right) \tag{4.3}$$

where β=2.35η is the FWHM of the mosaic spread (*mosaicity*).

In transmission configuration and with the diffracting planes perpendicular to the cross section of the crystal tile, the crystal reflectivity $R(\delta,\, E)$ is given by [37]:

$$R\left(\delta, E\right) = \frac{I_d\left(\delta, E\right)}{I_0} = \sinh\left(\sigma T\right) \exp\left[-(\mu + \gamma_0 \sigma)\frac{T}{\gamma_0}\right] = \frac{1}{2}(1 - e^{-2\sigma T})e^{-\mu\frac{T}{\gamma_0}}, \tag{4.4}$$

where I_0 is the intensity of the incident beam, μ is the absorption coefficient per unit of length corresponding to the energy E, γ_0 is the cosine of the angle between the direction of the photons and the normal to the surface, T is the thickness of the mosaic crystal and σ is:

$$\sigma = \sigma(E, \delta) = W(\delta) Q(E) f(A), \tag{4.5}$$

where

$$Q(E) = \left| \frac{r_e^2 F_{hkl}}{V} \right|^2 \lambda^3 \frac{1 + \cos^2(2\theta_B)}{2 \sin 2\theta_B}, \tag{4.6}$$

in which r_e is the classical electron radius, F_{hkl} is the *structure factor*, V is the volume of the crystal unit cell, λ is the radiation wavelength $\left(\lambda = \frac{hc}{E}\right)$ and θ_B is the Bragg angle for that particular energy, while $f(A)$ is given by

$$f(A) = \frac{B_0(2A) + |\cos 2\theta_B| \, B_0(2A \, |\cos 2\theta_B|)}{2A \, (1 + \cos^2\theta_B)} \tag{4.7}$$

where B_0 is the Bessel function of zero order integrated between 0 and $2A$, with A defined as follows:

$$A = \frac{\pi t}{\Lambda_0 \cos \theta_B} \tag{4.8}$$

in which t is the crystallite thickness, and Λ_0 (*extinction length*) is defined for the symmetrical Laue case as [46]:

$$\Lambda_0 = \frac{\pi V \cos \theta_B}{r_e \lambda \, |F_{hkl}| \, (1 + |\cos 2\theta_B|}. \tag{4.9}$$

In general $f(A) < 1$ and converges to 1 if $t \ll \Lambda_0$. In this case we get the highest reflectivity.

Assuming that the range of values of δ, when σ is significantly greater than zero, coincides with the Full Width at Half Maximum β of the Gaussian function, by differentiating the Bragg law (Eq. 4.1), the energy range diffracted by the mosaic crystal is obtained:

$$\frac{\Delta E}{E} \approx \frac{\beta}{\tan \theta} \tag{4.10}$$

where θ is the Bragg angle for the energy E. ΔE, for the energy range and materials considered in this thesis, turns out to be at most about few keV.

4.3.1 The structure factor

The structure factor F_{hkl} is an imaginary coefficient which quantifies the scattering "efficiency" of an elementary cell, i.e considering the diffusion by each atom of the cell. F_{hkl} is related to: the atomic scattering factor and depend on the geometrical factor, that takes into account the interferences between atoms.

The *atomic scattering factor* (f) represents the amplitude of the wave scattered by a single atom, expressed in terms of the contribution from a single electron. f depends on $sin\theta_i/\lambda_0$ and approaches the electron number (Z) for small values of this ratio. The exact calculation of the atomic scattering factor for any $sin\theta_i/\lambda_0$ is usually difficult, but it is much easier (and efficient) to use the following formulas, valid for small incident angles (i.e less than $\approx$ 10 deg, so this condition is always satisfied in the X and gamma ray regimes):

$$f = c + \sum_{i=1}^{4} a_i e^{-b_i(\sin\theta_i/\lambda_0)^2}, \tag{4.11}$$

which is, using the Bragg relation:

$$f = c + \sum_{i=1}^{4} a_i e^{-b_i/4d^2_{hkl}}. \tag{4.12}$$

The coefficients c, a_i and b_i (in Å^2) depend on the crystal material.

The atomic scattering factor gives the intensity of the diffracted beam. Since these atoms are in a crystal lattice, it is necessary to add the waves scattered by all the atoms of an elementary cell. This cumulative effect results in the *structure factor* since it depends on the geometry of the lattice:

$$F_{hkl}(\Delta\mathbf{k}) = \sum_{m=1}^{n} f_m e^{-i\Delta k\cdot(u_m\mathbf{a}+v_m\mathbf{b}+w_m\mathbf{c})}, \tag{4.13}$$

and, using the Laue conditions relation:

$$\Delta k \cdot b = 2k\pi, \quad \Delta k \cdot c = 2l\pi, \quad k, l \in Z \tag{4.14}$$

it becomes:

$$F_{hkl} = \sum_{m=1}^{n} f_m e^{-2i\pi(hu_m+kv_m+lw_m)}, \tag{4.15}$$

where n is the number of atoms per elementary lattice, the mth atom being at the position (u_m, v_m, w_m) in the unit cell defined by the lattice vectors ($\mathbf{a}$, $\mathbf{b}$, $\mathbf{c}$). f_m is the atomic scattering factor of the mth atom. When all the atoms of the lattice are of the same kind (e.g copper, germanium, etc), the structure factor can be written as:

$$F_{hkl} = f \sum_{m=1}^{n} e^{-2i\pi(hu_m+kv_m+lw_m)} = fG \tag{4.16}$$

where G is the $geometrical\ factor$, which only depends on the positions of the atoms in the lattice and on the Miller indexes. The geometrical factor in some cases may be equal to 0, showing that, due to destructive interferences, some crystal planes cannot reflect the beam.

4.4 Primary and secondary extinction

A perfect crystal under reflection condition corresponding to the lattice planes (hkl) gives rise to a reflected ray which may be diffracted again, giving rise to a further reflection. The rigorous derivation of the diffracted wave amplitude, made by Kirchoff [80], points out a phase shift of $\pi/2$ with respect to the incident wave; so the twice reflected beam is perfectly out of phase ($\Delta\varphi = \pi$) with the incident ray. This phenomenon causes the attenuation of the incident beam, in addition to that of the diffracted beam, to which contributions are subtracted (Fig. 4.4). This phenomenon is known as primary extinction.

The greater the perfection of the crystals, the stronger will be the primary extinction. In reality, each mosaic consists of a large number of crystallites relatively small (1-10 μm) arranged in a three-dimensional mosaic (Fig. 4.5) of small perfect blocks, but separated one from another by cracks and irregularities; the individual blocks have different sizes and are misaligned.

In a mosaic crystal secondary extinction occurs when a ray makes diffraction on the (hkl) plane, the incident beam undergoes an attenuation; there-

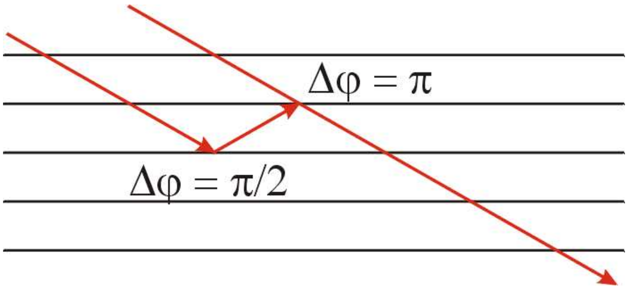

Figure 4.4: Multiple reflections inside a perfect crystal.

fore the deeper regions of the crystal will be irradiated by weaker rays. The attenuation of the diffracting intensity before arriving to a given crystallite give the secondary extinction, and will be more appreciable for those planes with high $|F_{hkl}|^2$ and small value of $sen\theta/\lambda$. This effect will increase for crystals which exhibit big sized crystallites.

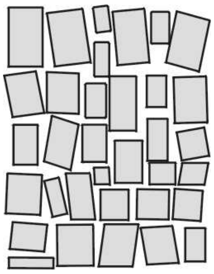

Figure 4.5: Crystallites inside an ideally imperfect crystal.

The primary extinction, as already stated, is the destructive interference between the incident and the scattered radiation and takes place only in a perfect crystal. If the perfect crystal block has a thickness greater than about 5 x 10^{-5} cm, primary extinction is appreciable. Indeed, the condition for negligible primary extinction is given by [46], and occurs when:

$$A = \frac{r_e \lambda t}{V} \frac{|F_{hkl}|}{\cos\theta_0} \ll 1, \tag{4.17}$$

where A is defined in Eq. (4.8). From Eq. (4.17) we can get the thickness of micro-blocks t for a negligible primary extinction:

$$t \ll \frac{V}{r_e \lambda} \frac{\cos\theta_0}{|F_{hkl}|}. \tag{4.18}$$

This equation also shows that for a given micro-block there are always wavelengths that are short enough for the primary extinction to be considered negligible.

Secondary extinction is proportional to the reflection intensity and causes an effect of the same order of magnitude as that of the ordinary absorption in the crystal. Consequently if the crystal is so small that its ordinary absorption for the radiation is negligible (1 or 2 percent), secondary extinction is negligible. The condition for negligible secondary extinction, is the following:

$$\frac{R_{hkl}}{\mu t} \ll 1, \tag{4.19}$$

where R_{hkl} is the *integrated reflectivity*, defined as the integral of the reflectivity, in an angular range $[\theta_{min},\theta_{max}]$. This equation derives from the request that the power loss due to diffraction is much smaller than that due to normal absorption. The ordinary absorption becomes very small in a crystal as its thickness decreases (depending on the material and energy), and secondary extinction may therefore be neglected in measurements upon crystal whose crystallites are smaller than this lower limit.

Small primary and secondary extinction set a tight condition to the value of the micro-blocks thickness t, which is given by:

$$\frac{R_{hkl}}{\mu} \ll t \ll \frac{V}{r_e \lambda} \frac{\cos\theta_0}{|F_{hkl}|}. \tag{4.20}$$

It turns out from this relation that the thickness of crystallite, for which the diffraction theory of the mosaic crystals is valid, is few microns.

4.5 Bent crystals

Diffraction in crystals with curved atomic planes is described by the Takagy-Taupin's theory [81] of strongly distorted crystals, which has an analytical solution in the case of a constant strain gradient, i.e. a crystal with spherically curved planes. In this theory, the crystal distortion is described by the strain gradient β, that, in the case of a uniform curvature, is given by:

$$\beta = \frac{\Omega}{T_0\,(\delta_w/2)} \tag{4.21}$$

where Ω being the FWHM of the angular distribution of diffracting planes (we will call *spread*), T_0 the thickness of the crystal and δ_w the Darwin width. The peak reflectivity R^{max} of a curved crystal is given by:

$$R^{\max} = \frac{I_h(T_0)}{I_0(0)} = \left(1 - e^{-\frac{\pi^2}{2\alpha}}\right) e^{-\frac{\mu T_0}{\cos\theta_B}}, \quad \alpha > 1, \tag{4.22}$$

where α is proportional to the curvature of the diffracting planes multiplied by the square of the energy: $\alpha \propto \frac{\Omega E^2}{T_0}$.

From equation 4.22 it comes out that curved crystals can reach a higher efficiency than mosaic crystals. Indeed, while the diffraction efficiency of mosaic crystals is limited to 50% (eq. 4.4), that of curved crystals can reach 100%. The diffraction profile of a bent crystal has a rectangular shape (Fig. 4.6) whose width is driven by the spread Ω, whereas for a mosaic crystal the diffraction pattern is a Gaussian curve as broad as the mosaicity. Thus curved crystals, given that do not have Gaussian tails, better concentrate gamma-rays [48], [49], [50].

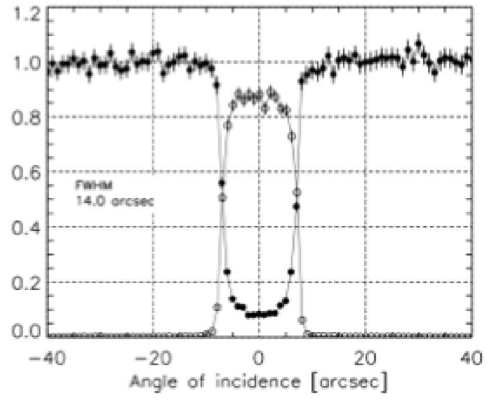

Figure 4.6: Bent Si (111) crystal rocking curve at 150 keV [48].

4.6 The Laue lens concept

The X-ray diffraction theory, shows that with some kinds of crystals, is possible to deviate gamma-ray photons in an energy band that depends on the mosaic spread of the crystal. By properly placing a set of mosaic crystals on a spherical surface it is possible to deviate, through Bragg diffraction, photons of a broad energy band towards a focal point as it is shown in Figure 4.7. The combination of such positioned crystals composes a Laue lens. The crystals have to be positioned with the aim of getting the maximum effective area depending on the available crystal material and gamma-ray energy.

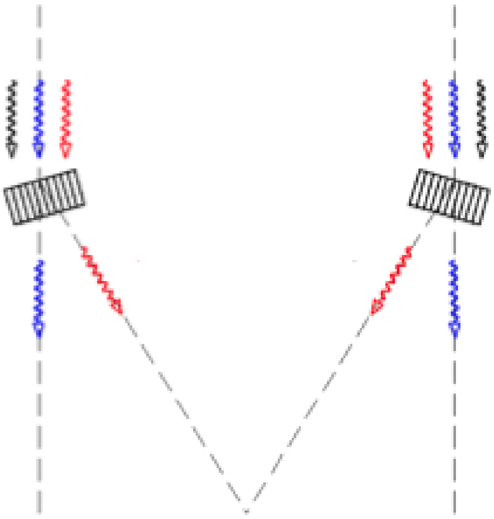

Figure 4.7: Properly oriented crystals can deviate photons towards a focal point by means of diffraction. In the Laue configuration (transmission) only a fraction of the photons are diffracted (*red*). The remaining photons are either absorbed (*black*) or transmitted (*blue*).

4.6.1 Working principle

The Bragg diffraction in transmission geometry (Laue configuration) is the working principle of Laue lenses. As it will be discussed later, the design of the lens exploit the Bragg law (Eq. 4.2) and its consequences. Smoothly varying either the incident angle or the material (d_{hkl}) of a set of crystals properly arranged, it is possible to broaden the energy band of the focused beam (Fig. 4.8). The best way is to place the set of crystals tangent to a spherical surface.

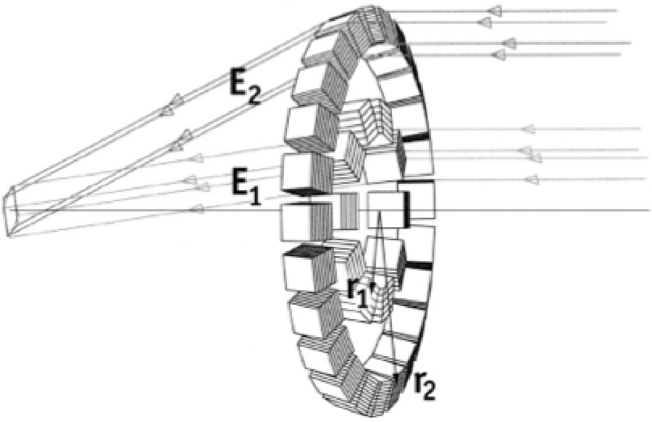

Figure 4.8: Principle of Laue lens. The gamma-rays from a source at infinity are diffracted, to the focal point of the lens, by crystals placed in concentric rings [48].

According to the Bragg equation, the photons of a beam parallel to the z axis (Fig. 4.9), with an energy E in the band ΔE, are being diffracted only by crystals whose lattice planes have an angle θ_B corresponding to the energy E. The relation between the energy band of the lens (E_{min}, E_{max}) and the radii r_{min}, and r_{max} depends on the angles θ_{max} and θ_{min} between the lattice planes of the crystals at different rings and the incident polychromatic beam. From Eq. (4.2) we get:

$$E_{min} = \frac{hc}{2d \sin\theta_{max}} \approx \frac{hcf}{d_{hkl} r_{max}}, \tag{4.23}$$

$$E_{max} = \frac{hc}{2d \sin\theta_{min}} \approx \frac{hcf}{d_{hkl} r_{min}}, \tag{4.24}$$

The most important parameter of a lens is its effective area A_{eff}, defined as the geometric area projected onto the focal plane of the lens multiplied by the reflectivity at given energy E. To make sure that A_{eff} changes very slowly and have, therefore, a continuing response over the lens working band, the

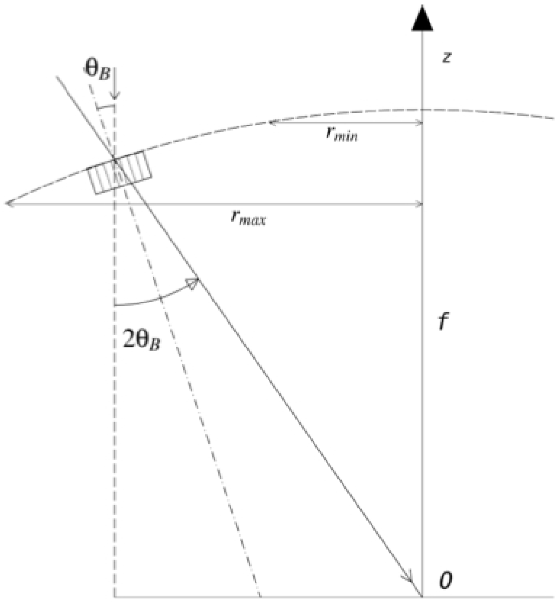

Figure 4.9: Basic principle of a Laue lens in which the crystals are placed on a spherical surface.

crystals material, their disposition and the geometrical configuration must be accurately chosen.

Given that the Laue lens passband for astrophysical measurements (see Sec. 1.5) has to be covered in a continuous way, the energy passband of each crystal (or ring of crystals) must superpose with the contiguous one. Since the acceptance angle $\Delta\theta$ of perfect flat crystals (known as *Darwin width*) is extremely narrow (fractions of arcsec to a few arcsec) such materials are not suitable for astrophysical Laue lenses.

In order to have a wider energy bandpass from individual crystals, one can use flat mosaic or perfect/mosaic bent crystals (see Sec. 4). The mosaic width, or *mosaicity*, of the crystals governs the flux throughput, the angular resolution and the energy bandpass of the crystal lens. The diffracted flux from a continuum spectrum increases with increasing mosaic width of the crystal. Moreover, thanks to the broader energy range that crystals with mosaic structure or bent diffractive planes can reflect, the reflectivity curves of adjacent tiles overlap in order to cover with continuity through the working band of the lens, from the lower energy E_{min}, corresponding to the radius r_{max} of the outer ring of crystals, to the higher energy E_{max}, corresponding to the innermost radius r_{min}. As an example in Figure 4.10 it is shown the reflectivity curve of three contiguous crystals [43].

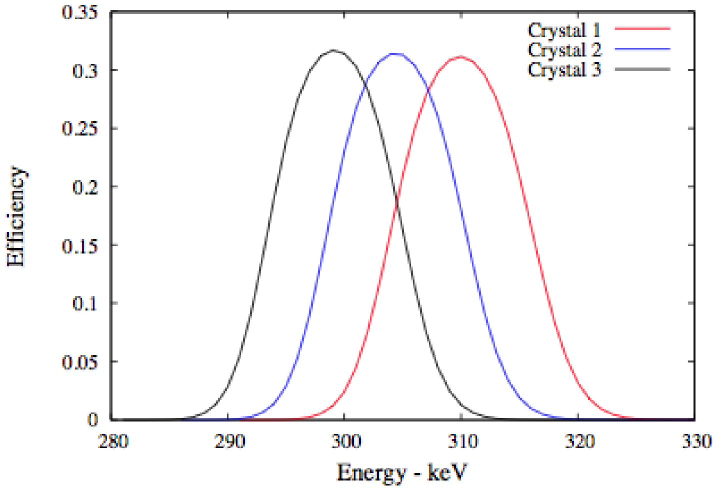

Figure 4.10: Reflectivity curves of three contiguous flat mosaic crystals, with a mosaicity of 1.5 arcmin, on a spherical surface.

By forming the derivative of the Bragg equation in the small angle approximation ($2d_{hkl}\theta_B \approx hc/E$), we get:

$$\frac{\Delta\theta_B}{\theta_B} = \frac{\Delta E}{E}, \tag{4.25}$$

where $\Delta\theta$ is the mosaic width, or angular spread, of the crystal. The energy bandpass ΔE of the crystal becomes:

$$\Delta E = \frac{2d_{hkl}E^2\Delta\theta_B}{nhc}. \tag{4.26}$$

It is worth pointing out that the energy bandpass of a crystal lens grows with the square of energy.

The focal length has a key importance in the case of Laue lenses. Indeed, given that the energy passband of a single crystal is very narrow, the lens radius r at which the photon energy E is reflected in the focus depends on f:

$$r = f\tan(2\theta_B) = f\tan\left[2\arcsin\left(\frac{hc}{2Ed_{hkl}}\right)\right] \approx \frac{hcf}{d_{hkl}E}. \tag{4.27}$$

Thus f is crucial to extend the lens passband. Given that high energy photons are focused by the innermost part of the lens, the lens inner area can be increased only increasing the focal length (the lens area approximately increases with f^2). A gamma-ray lens with a broad continuum coverage from 300 keV to 1.5 MeV was proposed in the 90's by N. Lund [44].

Chapter 5

The HAXTEL Project

The HAXTEL project was devoted to perform a design study and development of a Laue lens prototype. In 2011, when I joined the project, a second upgraded prototype was on going to be realized, which relied on the improvements coming from the previous prototype formerly built and tested. In the second prototype an upgraded version of the tools employed in the building phase made possible performance improvements of the Point Spread Function.

After describing the LARIX A X-ray facility in which the lens prototypes are developed, as in 2011, I will report the development technique adopted for the project along with calibrations, alignment and tests, eventually highlighting the results of the last lens prototype.

5.1 The LARIX facility

The apparatus employed for the HAXTEL project is in the section A of the LARIX (LARge Italian X-ray facility) laboratory at the Physics and Earth Science Department of the Ferrara University.

In Figure 5.1 it is shown the configuration of the LARIX A facility. The main components include an X-ray tube as source of polychromatic X-ray beam working in the energy range (15-140 keV), an helium box where a fixed-exit double-crystal monochromator is installed, a system of collimators plus a Pb shield to stop the scattered radiation in the testing room, a four-axis

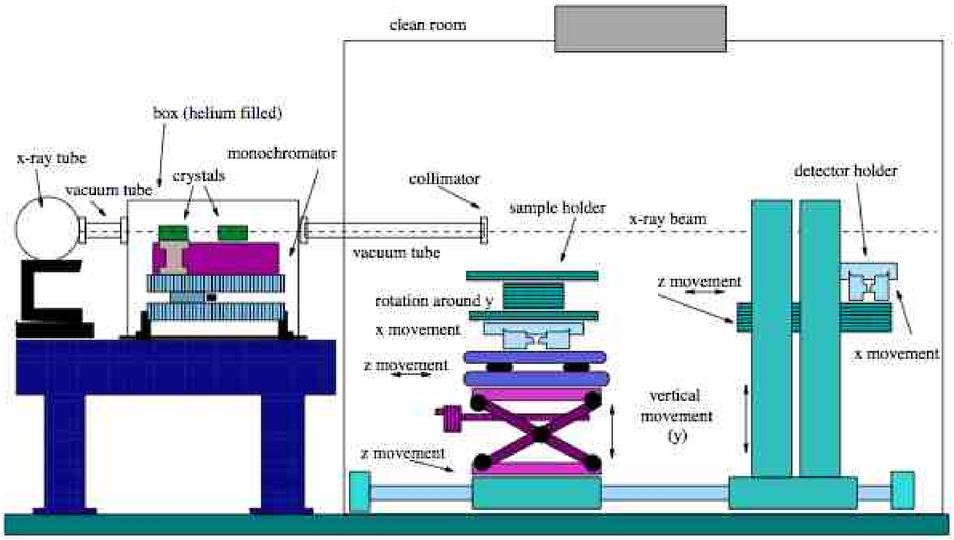

Figure 5.1: Sketch of the configuration, as in 2011, of the Ferrara X-ray facility. From the left: the X-ray tube, the monochromator system, the sample holder and the detector holder.

table used as sample holder, and a three-axis detector holder [36].

5.1.1 X-ray Source

The X-ray source is on an optical table installed in a completely shielding lead box but a hole (Fig. 5.2). The tube is equipped with a Tungsten anode (fine focus of 0.4 mm radius), with its voltage which can be set in the range from 30 to 140 kV and its current from 0.1 to 2.5 mA. Its output window is equivalent to a 1.5 mm thick aluminium foil, fixing the low-energy threshold of the beam to about 15 keV.

5.1.2 Monochromator

The purpose of the double crystal monochromator is to produce a monochromatic beam from the continuum spectrum provided by the X-ray tube. One of its main features is that it provides a fixed-exit beam independently of the photon energy selected. The geometrical configuration of the installed

Figure 5.2: A view of the X-ray generator tube, located in a lead box.

monochromator is a Bragg - Bragg (BB) with fixed exit. In this configuration the diffracting elements, two Si (111) crystals with mosaic structure ($\beta = 30$ arcsec) to get a brighter beam, exploiting the Bragg diffraction and produce a monochromatic beam after two reflections. The first Silicon crystal (B) has the role of selecting the desired wavelength from the incident continuum beam, while the second crystal (D) re-directs the monochromatic radiation along the direction parallel to the incident beam (Fig. 5.3).

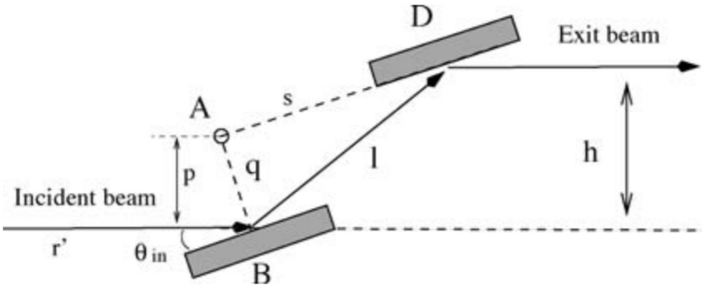

Figure 5.3: Top view of the BB fixed exit configuration: A is the rotation axis, θ_{in} is the Bragg angle and $h = 2 \times p$.

The B crystals is allowed to translate along a radial direction with respect to the rotation axis but constrained to cross the path of the incident beam. The D crystal can be shifted back and forth (Fig. 5.3) to redirect the beam coming from B. Both crystals can be tilted along their two rotation angles, for a fine tuning of the alignment. The diffractometer is tunable over a wide range of X-ray energies (15-120 keV), by rotating B and D around the vertical axis, changing both Bragg angles, and by translating D along the direction parallel to its external surface. The benefits of such a configuration are:

- The exit beam is parallel to the incident one and its direction is fixed i.e., independent of monochromatic energy.
- The crystals dimensions are smaller than those employed in other configurations (monolith Bragg - Bragg or Laue - Bragg), since the system is designed in such a way that the X-ray beam hits the crystals approximately in the same point.
- Considerable versatility since the crystals in use can be easily interchanged to broaden or change the energy band.
- Wide energy range, i.e. the LARIX monochromator can operate between 15 keV and more than 100 keV.

The calibration of the system has been carried out through three phases: determination of the rotation centre of the system, first alignment performed with a laser source, second alignment by using the X-ray beam.

For detecting the rotation center of the monochromator we positioned a laser beam initially horizontal (Fig 5.4) is reflected by a 45° degree inclination mirror to get a vertical beam. This beam is separated by a beam-splitter mirror in two opposite beams, one directed toward the X-ray source output and the other toward the B crystal. Thanks to this equipment installed on the optical bench, it was possible to get an optical beam with the same direction of the X-ray beam. After placing a needle approximately on the rotation centre, we changed its position until the laser beam was steady on it for different angles of rotation of the system. Since the needle lies in the rotation centre its position must be constant as the system rotates. Once the center was found we were able to move the first crystal to its nominal position, as foreseen by the BB configuration.

This first alignment is aimed at obtaining a coarse positioning of the two collimators and of the crystals tilt, by observing directly the reflections of the laser beam on the two crystals.

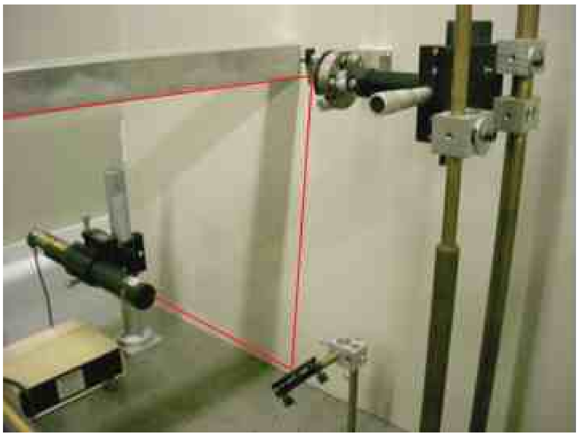

Figure 5.4: The optical alignment system. The laser beam is reflected upward to a *beam splitter* which is appropriately positioned to direct the beam as if it came from the X-rays source. Once the laser is perfectly aligned, it is possible to correct the positions of the collimators and tilts, until the laser beam will be observed at the monochromator exit without changing direction.

The second alignment was performed to determine the corrections to be applied to the crystals translation and tilts, by analyzing with the X-ray imager (see Sec. 3.4) the X-ray beam emerging from the monochromator. To make easier the alignment phase, a program in LabVIEW has been developed, which allows to adjust the position of both the tilt and second collimator (Fig. 5.5).

5.1.3 Sample holder

The sample holder (Fig. 5.6) can be translated in three perpendicular directions (X, Y, Z) and rotated around two orthogonal directions. The minimum step size of the translation stages is 1 μm, with linear speed from 0.025 to 8 mm/s. The translation stages are 300 mm long. The holder can support a sample of about 100 kg, because it was designed to hold the JEM-X experiment on board the INTEGRAL satellite [36]. The above movements are monitored with an external system of optical encoders of 5 μm sensitivity. In this way the true position of the sample and the performances of the XYZ table can be accurately measured. The angular stage has an accuracy of $3.6''$.

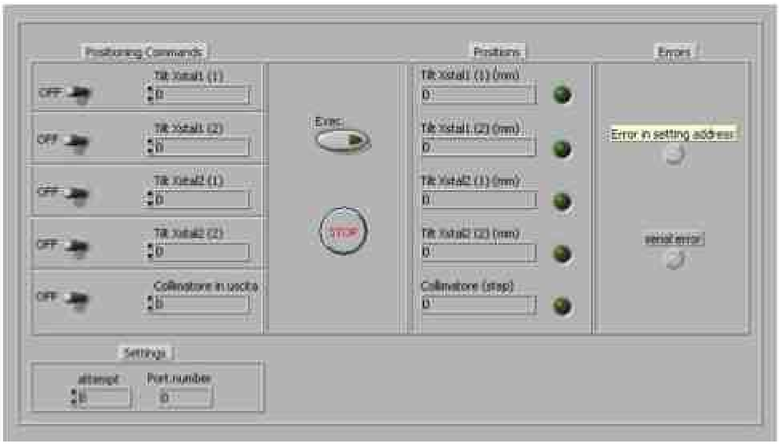

Tilt Xstal1 (1) 0
Tilt Xstal1 (2) 0
Tilt Xstal2 (1) 0
Tilt Xstal2 (2) 0
Collimatore in uscita 0
Tilt Xstal1 (1) (mm) 0
Tilt Xstal1 (2) (mm) 0
Tilt Xstal2 (1) (mm) 0
Tilt Xstal2 (2) (mm) 0
Collimatore (step) 0
attempt 0
Port number 0

Figure 5.5: Controller interface (LabVIEW) for the adjustment of the tilt, monochromator angle and collimator output. It is possible to move individually or at the same time the various motors, specifying the location to achieve in steps or in *mm*.

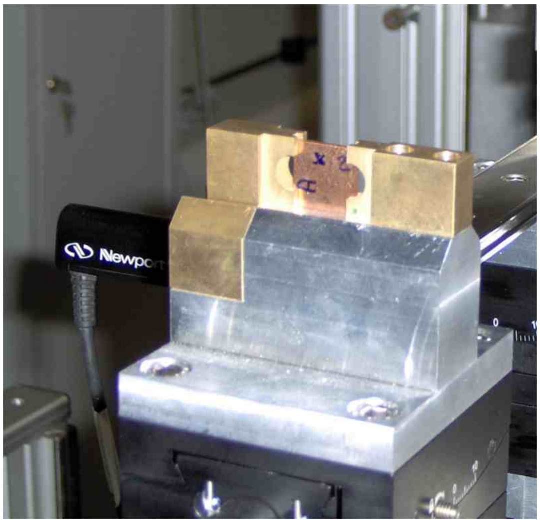

Figure 5.6: The samples holder.

5.1.4 Detectors

Two detectors are available in the LARIX facility: an high purity germanium detector (HPGe) and an X-Ray Image detector, provided by Thales.

The X-ray imaging detector (Fig. 5.7) has already been described in Section 3.4. The high purity germanium detector (HPGe), cooled with liquid nitrogen, has a surface area of about 78.5 cm^2, a thickness of 13 mm and an X-ray entrance window of 0.254 mm Beryllium thickness. This configuration gives an high detection efficiency to the X-rays provided by the facility. The energy resolution is about 0.8 keV at 60 keV.

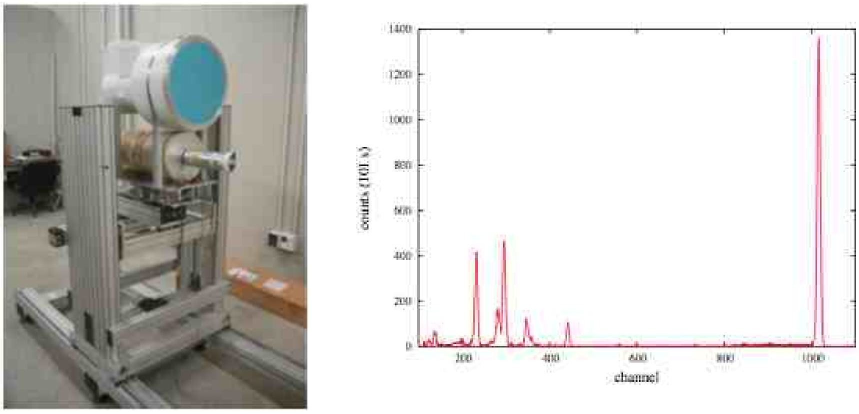

Figure 5.7: *Left*: The two detectors available in the LARIX facility. *Right*: ^{241}Am spectrum obtained with the HPGe detector. Acquisition time $t = 100s$.

5.1.5 X-ray beam collimation

The X-ray facility basically has two fixed collimators, one at the end of the optical bench (2 meters far from the source), and the second close to the sample holder (about 5 meters from the source). The goal of the collimation system is that of parallelizing the X-ray beam coming from the X-ray source. In order to absorb the unwanted X-rays, the material chosen for the collimators is tungsten with enough thickness (4 mm). By decreasing the aperture of the collimators the divergence of the beam can be increased or decreased. The collimators influence the beam intensity as well. Indeed the polychromatic beam has a very high intensity which can be dangerous for our detectors, so it is needed to narrow the collimator aperture.

5.2 Crystal properties

The tiles used for building the lens prototype for the XAXTEL project are mosaic crystals made of Copper with a cross section of 15 × 15 mm^2 and 3 mm thick. The lattice planes selected for the diffraction have Miller indices (111).

Mosaic crystals are characterized by a mosaicity β, a crystallite size t and effective thickness T. As already seen in this chapter, the mosaicity is an intrinsic property of the single tile and in principle is the same for all crystal tiles, if each of them comes from the same ingot. However the cutting process can give rise to different mosaicities. The best cristallite size that provide the best reflectivity should be at most of the order of ten μm (see Sec 4). The mosaicity of the Cu (111) crystals, provided by ILL-Grenoble, is about 2.0-3.0 arcmin.

We estimated the mosaicity of each crystal tile by measuring its reflectivity, after correcting the beam divergence, and comparing it with the expected reflectivity function (for details see [84]). The correction for the beam divergence is crucial. Indeed, due to the beam divergence, the crystal is hit on its surface with different Bragg angles and this affects the response function which is broader than that expected as a result of the crystal mosaicity. If one ignores the correction for the divergence effect, mosaicity values higher than 6 arcmin and crystallite sizes from 200 to 400 μm are derived. By correcting for the divergence effect, the parameters become much more physical and satisfactory (β = 2.0-3.0 arcmin; t_0 = 30-70 μm).

The divergence-corrected results were tested with an experimental procedure. For a subset of crystal tiles, lower and lower beam divergence values, obtained by decreasing the beam size from 10×10 mm^2 to 2×2 mm^2, were obtained and the corresponding reflectivity measured. Without taking into account the correction for divergence, we derived the gross mosaicity (called *equivalent mosaicity*) and its dependence on beam divergence, as shown in Figure 5.8. As can be clearly seen, as the divergence converges to zero (beam size approaching to ~ 0), the equivalent mosaicity reaches the crystal true mosaicity. For three crystals analyzed with the experimental method, we estimated a crystal mosaicity of 2.57, 2.55 and 2.68 arcmin, respectively,

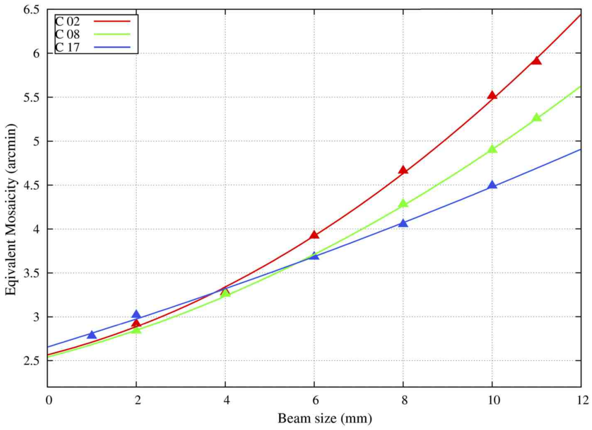

Figure 5.8: The *equivalent mosaicity* as a function of the beam size for a subset of crystal. Superimposed to the experimental data, a polynomial function was used to fit and extrapolate the real value of the mosaicity, at beam size equal to zero.

These values are in good agreement with those obtained by correcting the reflectivity function for the divergence (2.72, 2.48 and 2.84 arcmin).

We have carried out systematic measurements in order to verify the uniformity, in terms of mosaicity and efficiency, of the crystal tiles by testing the samples in different points (9) of the cross section. Figure 5.9 shows the test performed on one of the 28 candidates crystals. The mosaicity values obtained (Table 5.1) show the uniformity of the tested crystal.

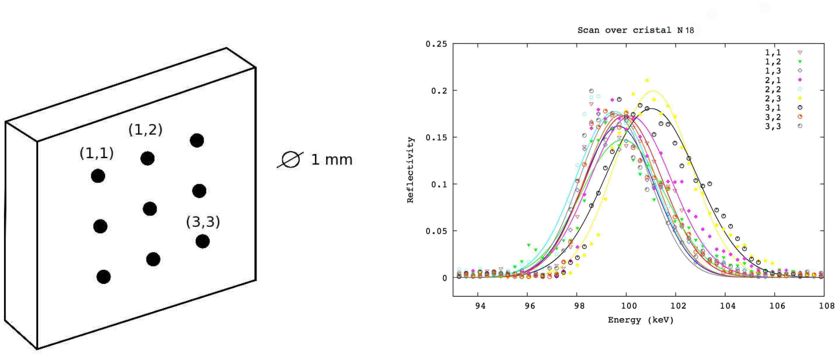

Figure 5.9: *Left*: The tested points. *Right*: RCs best fit for the tested sample.

Table 5.1: Mosaicity values related to one of the tested crystal.

Tested Point	Mosaicity (arcmin)
1.1	1.61
1.2	1.51
1.3	1.43
2.1	1.70
2.2	1.66
2.3	1.84
3.1	1.97
3.2	1.52
3.3	1.50

5.3 Lens assembly technique

The project foresees the realization of a 6 meters focal length Laue lens Prototype Model (PM) based on the technique of the counter-mask. The improved assembling procedure, is currently protected by a patent which is being submitted.

5.4 Lens testing and results

For its testing, the PM (Fig 5.10) is positioned on the sample holder of the LARIX facility located 6 m far from the source. In fact, the PM is designed on the basis of the incoming divergent beam from the X-ray source, placed at 6 m from the lens. The crystal are positioned on the lens frame in such a way that the mean direction of their diffractive planes is parallel to the lens axis. Therefore the incoming photons are reflected, by the set of crystals, by an angle such as to focus on the focal plane, 6 m away from the PM, where the detectors are placed. These can be remotely translated back and forth along the beam axis for finding the best focusing position and for getting, out of focus, the diffracted image of each tile.

Figure 5.10: The second prototype after the assembling phase and mounted on its support ready to be tested.

To avoid direct radiation to arrive on the focal plane detector, the entire inner region of the lens frame is covered by a lead layer 3 mm thick. The upper panel of Figure 5.11 shows the focal spot of the first PM [38] when the polychromatic beam irradiates the entire lens. The dark circular region shows the expected spot. This spot was obtained with Monte Carlo techniques, taking into account the mosaicity of the crystals and an ideal lens with diffraction from perfectly aligned crystals. The first light of the last PM is shown in Figure 5.11 (lower panel).

We carried out the spectral analysis of the focused beam, and the results are shown in Figure 5.12. The lens prototype was designed for giving a spectral peak at 100 keV at the focal point. In the left panel is shown the spectrum obtained collecting only the photons coming in the central region of the focus, while in the right panel, it is shown the spectrum of all the photons reflected by the lens and collected on the focal plane. In both cases the exposure time was 1000 seconds. As can be seen, in the central region the peak is at 98.89 keV. The centroid of the spectrum of the central region achieves an intensity level 0.8 times that of the peak spectrum of all reflected photons.

To better figure out the improvement made with the last prototype, the cumulative distribution of the number of photons collected along the radial

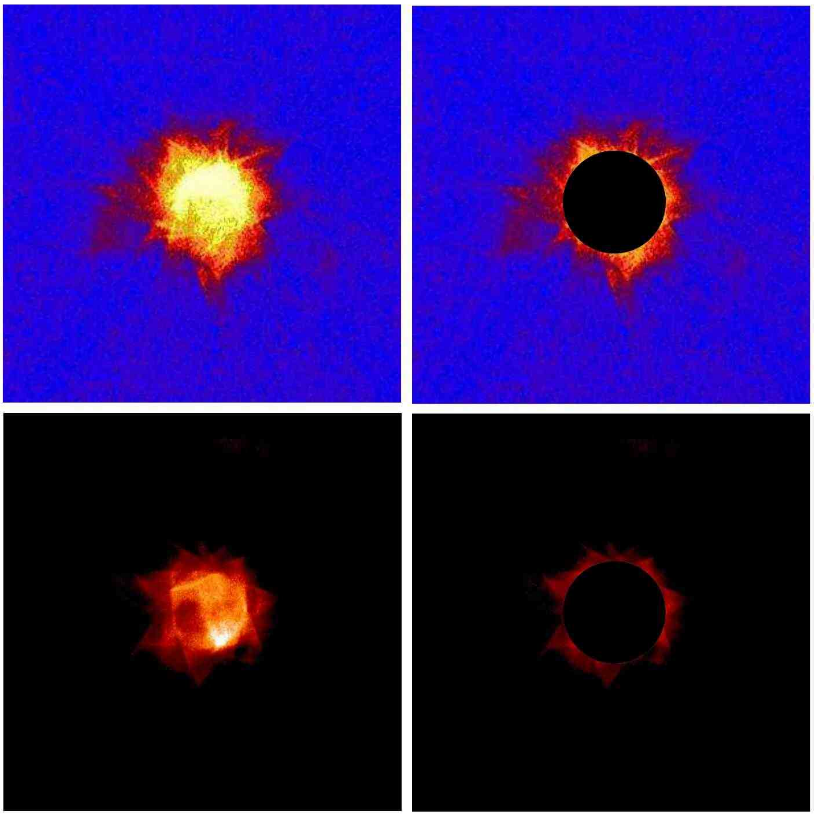

Figure 5.11: PSF Comparison between the first (*top*) and the second PM (*bottom*). The black circle represents the spot expected from Monte Carlo simulations assuming each crystal perfectly positioned and diffracting in the expected focal area.

distance from the focal point has been carried out. As can be seen, while the expected half power radius (HPR), i.e. the radius within which 50% photons are collected, is 9 mm, the measured HPR was 17.4 mm for the first prototype [38], and 13.9 mm for the last prototype (Fig. 5.13). There is an improvement of about 42% with respect to the first prototype, considering theoretical value of the radius (9 mm) as the target. Thus this represents a significant improvement with respect to the first one. It can be also seen that, at the radius (16.00 mm) at which the saturation occurs for the expected cumulative distribution, the fraction of collected photons is around 0.7. For comparison, the first prototype showed a fraction less then 60%.

By shielding all the lens crystals but one, and measuring the barycen-

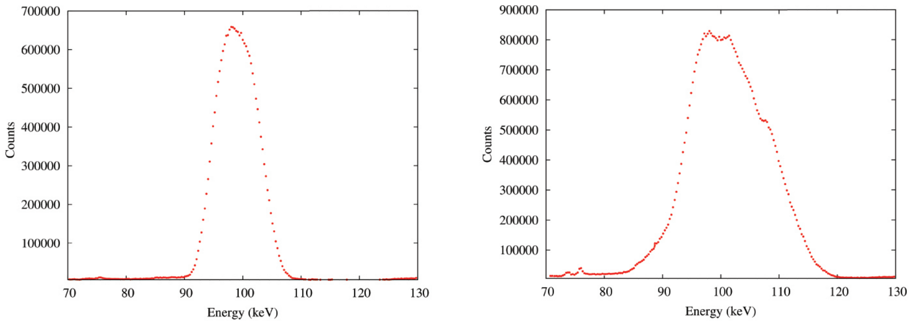

Figure 5.12: *Left*: Spectrum of the total photons reflected on the focus. *Right*: Spectrum of the total photons reflected by the lens in the region in and around the focus, on the focal plane.

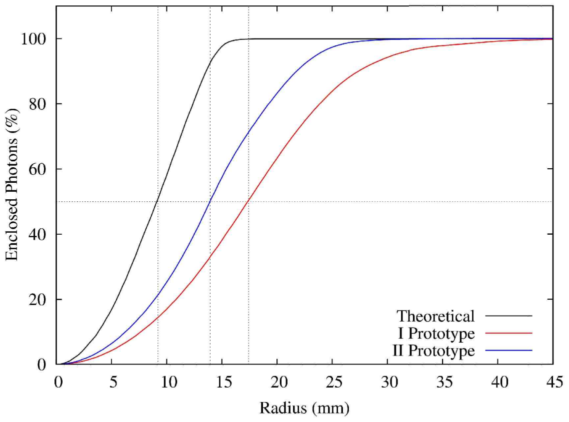

Figure 5.13: Cumulative distribution of the focused photons along the radial distance from the focal point. The *black line* corresponds to the expected distribution in the case of a perfect alignment of the crystals. The *red line* shows the photon distribution obtained in the first prototype while the blue line shows photon distribution for the second prototype.

ter coordinate of each diffracted spot, we have determined also the angular misalignment for each lens crystal. Figure 5.14 shows the deviation of each crystal, from their expected perfect position. For the total set of tiles, this deviation is within 6 arcmin (for the first prototype it was 15 arcmin).

Compared to the first prototype, the performance in terms of imaging capability has been improved, as the maximum angular deviation of the crystal tiles from their nominal ones has decreased from 15 arcmin to 6

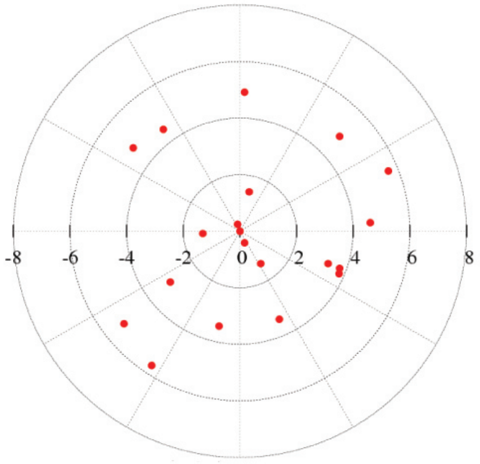

Figure 5.14: Angular deviation of each crystal on the second prototype with respect to the perfect alignment.

arcmin.

After evaluating the contribution of each step to the overall error budget, we attributed the 6 arcmin of mismatch between real and expected positioning of the crystals to the mechanical insertion of the pins in the counter-mask and to the successive separation process of the entire lens from the counter-mask.

In order to improve further the lens PSF, the only way we see is that of adopting a different assembling technique, in which each crystal tile is directly glued on the lens frame under a gamma-ray beam control. This is the goal of the LAUE project supported by the Italian Space Agency ASI, which will be presented in the Chapter 7.

Chapter 6

Bent Crystals for Laue Lenses

Bent crystals can improve the Point Spread Function of a Laue lens, with a consequent increasing of sensitivity and angular resolution.

In this chapter I report the first measurements performed on bent crystals with the goal to select the best crystal samples in terms of the thickness and efficiency for Laue lenses.

6.1 Introduction

The copper crystals selected for the building of the Laue lens prototype discussed in Section 5 showed a mosaicity of the order of 3-4 arcmin (FWHM) [33]. This value turned out to be too large for a long focal length Laue lens, as the dimension of the focal spot strongly depends on the crystal angular spread. Using curved crystals it would be possible to build a Laue lens with high reflection efficiency and very narrow PSF, thus significantly increasing the signal to noise ratio, and consequently leading to a sensitivity leap with respect to the existing non focusing telescopes.

There are different method to obtain curved crystalline planes, e.g. by growing a two-component crystal whose composition varies along the crystal growth axis, through a pure mechanical bending, or by applying a thermal gradient to a perfect single crystal. One of the main phases of the Laue project has been the choice of crystal materials to be employed for the lens.

6.2 Germanium and Silicon bent crystals

Silicon (111) and Germanium (111) mono-crystals have been bent at the University of Ferrara by the Sensor and Semiconductor Laboratory (LSS), thanks to a set of parallel superficial indentations on one of the tile cross section [51], [52], [54]. This technique relies on irreversible compression of the crystal beneath and beside the indentations. In this way a deformation is produced in the crystal with no need for an external device, resulting in a uniform self-standing curvature within the crystal. The curvature so obtained depends on the blade characteristics and the indentations sizes.

The bent crystals of Ge (111) and Si (111) produced in this way give rise to a quasi-mosaic (QM) inner structure. This quasi-mosaicity is an anisotropic effect that manifests itself when a properly oriented crystal plate is bent along a given direction, i.e., quasi-mosaicity depends on the crystallographic direction of the plate under bending (Fig. 6.1). Thus, a primary curvature imparted to a crystal along some given diffracting planes, results in a secondary (quasi-mosaic) curvature along a different direction [55].

Quasi-mosaicity is fully understood in the framework of the theory of linear elasticity. A square crystal plate subject to a couple of mechanical momenta applied along two perpendicular directions undergoes primary deformation (for more detail see [56]). For a Laue lens Ge (111) plates are well suited, because of their excellent reflectivity at high energies (>100 keV). Bending Ge tiles along $(11\bar{2})$ plane as a primary curvature, results in secondary curvature of (111) diffracting planes. Ge crystals can be accommodated as tiles on the spherical surface of a Laue lens, in such a way to have the diffracting planes (111) aligned with the radial direction. It is important to point out the presence of a relation between the primary and secondary curvature. The ratio between quasi-mosaic curvature (R_{QM}) and primary curvature (R_P), is shown to be the following [53]:

$$\frac{R_{QM}}{R_P} = 2.4 \tag{6.1}$$

By giving to the crystal a primary curvature equal to that required by the lens it will be possible to focus the photons onto a smaller focal spot (compared to that produced by a flat crystal with the same cross section)

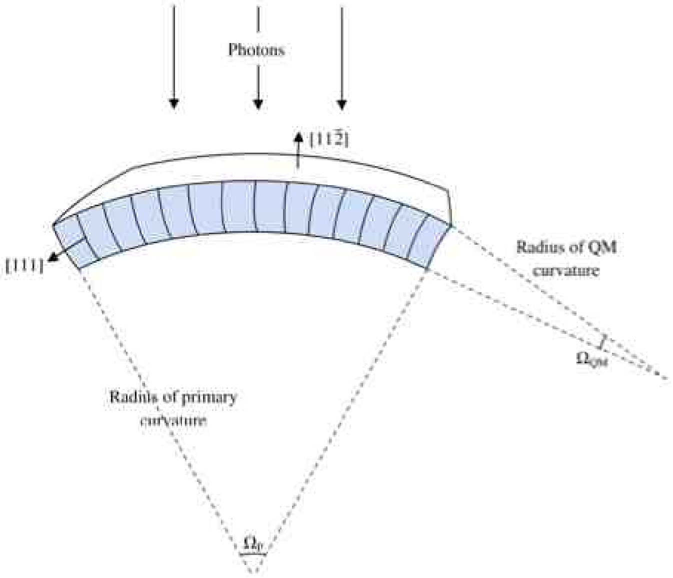

Figure 6.1: The primary curvature of a properly oriented crystal leads to a secondary curvature owing to quasi-mosaicity. In this configuration the Ge (111) and Si (111) diffracting planes are perpendicular to the main surface of the plate, thus positioning of the crystals in the lens would be the same as for mosaic crystals. Ω_P and Ω_{QM} are primary and secondary bending angles, respectively. [53].

as its size is only driven by the quasi-mosaic curvature within the crystal. Therefore the advantage of using QM crystals comes directly from their focusing capability as well as their wide passband thanks to the quasi-mosaic curvature, which perfectly match the requirements of Laue lenses.

6.3 Gallium Arsenide bent crystals

The mosaic crystals of Gallium Arsenide are grown at CNR-Institute of Materials for Electronics and Magnetism (IMEM) of Parma by the Liquid Encapsulated Czochralski method, as described in [58]. The bending can be achieved by a controlled surface damaging, which introduces defects in a superficial layer of few microns in thickness undergoing a highly compressive strain. The controlled surface damaging were obtained by means of a mechanical lapping process on one side of planar samples [57]. The samples are mounted on a plate with paraffin, the plate is then positioned upside down in the machine facing the sandpaper plate. The two components rotate independently on two different axes, so that the sample abrasion should be completely uniform on the entire surface of the sample plate. The rotation speed of the sandpaper plate can be manually regulated; the sandpaper is usually lubricated with water. The samples are lapped with different large grain sandpapers: P180, P400, P600, P1000, P1200, P2500, and P4000 (European P-series); the length of the treatment is ranging from 30 seconds up to 3 hours.

Some preliminary tests have been performed by IMEM group in order to characterize the GaAs crystals [59], [60]. Figure 6.2 shows the diffraction and transmission curves of bent GaAs (400) crystal obtained with a synchrotron source at energy E=120 keV in transmission geometry (thickness t=8 mm and the curvature radius R=16.5 m). The square shape of the diffraction curve is that expected for a bent crystal (Fig. 6.2 $left$).

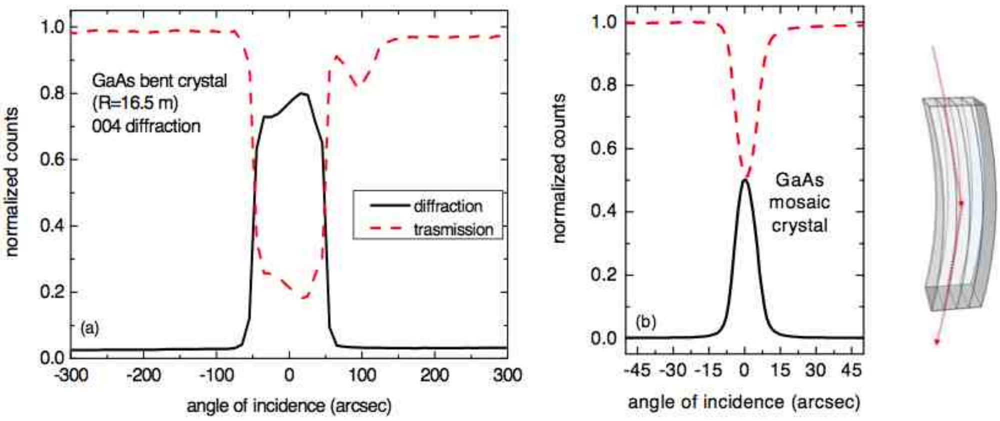

Figure 6.2: *Left*: GaAs (400) Laue diffraction (black solid lines) and transmission (red dashed lines) profiles measured at E=120 keV on a uniformly bent crystal obtained by surface treatment. *Right*: Reflection profile measured with a flat mosaic GaAs crystal. The sketch on the right shows the measurement geometry [60].

It is reported, for comparison, the diffraction and transmission (400) profiles measured at the same energy when a flat mosaic GaAs crystal is used. The crystal mosaicity is about 15 arcseconds with a peak efficiency of 50%.

With respect to the flat mosaic crystal, the diffraction efficiency of the bent sample reaches a value of about 71% with peak width related to the curvature of the diffracting planes. Therefore the integrated intensity, that is the area under the reflectivity curve, appears strongly enhanced. The results obtained by IMEM show that the lapping procedure is effective to obtain the crystal bending, the curvature radii are reproducible and fully dependent on the sample thickness and treatment characteristics. The efficiency results obtained by IMEM are promising, but cannot be applied for Laue lens case, since the crystal tiles are accommodated on the lens frame with a different configuration (geometry 2) (see. Sec. 6.4).

6.4 First tests of bent crystals

In the framework of the Laue project (see Sec. 7), one of the main goals is the development of a technology for the production of big quantity of bent crystals, provided by LSS Ferrara and IMEM Parma, with the required characteristics, in terms of curvature, efficiency, mosaicity. We have performed, at the LARIX facility, reflectivity measurements of bent crystals in different configurations, to confirm the expected results and to select the best crystal samples. Another goal was to optimize the thickness of the crystal tiles to be used for the Laue project.

A sketch of the apparatus is shown in Figure 6.3.

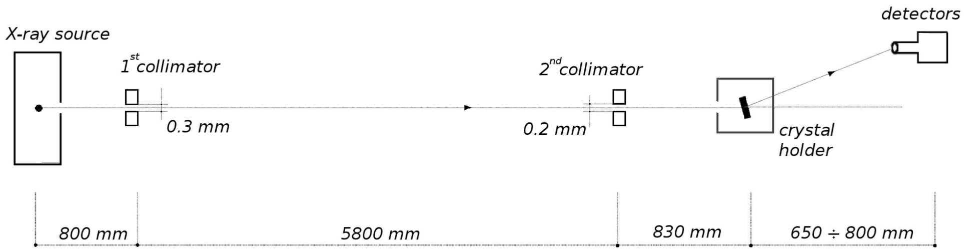

Figure 6.3: Top view of the apparatus used for the crystal testing.

By means of the motorized crystal holder, it is possible to translate the crystal samples along 2 directions perpendicular to the beam and to rotate the samples around three orthogonal axes. The X-ray beam coming from the source travels across two collimators with adjustable aperture, the former at 80 cm from the X-ray source, the latter at a distance of 83 cm from the crystal to be tested. The distance between the collimators is 580 cm. The direct and reflected beams are analyzed thanks the two detectors (X-ray imager and HPGe spectrometer) discussed in Sec. 5.1.4. The main properties of each sample are obtained by measuring the FWHM of the Rocking Curve (RC) and the reflectivity value. The measurements have been performed using the fluorescence $K\alpha_1$ line at 59.2 keV of the X-ray tube Tungsten anode (Fig. 6.4).

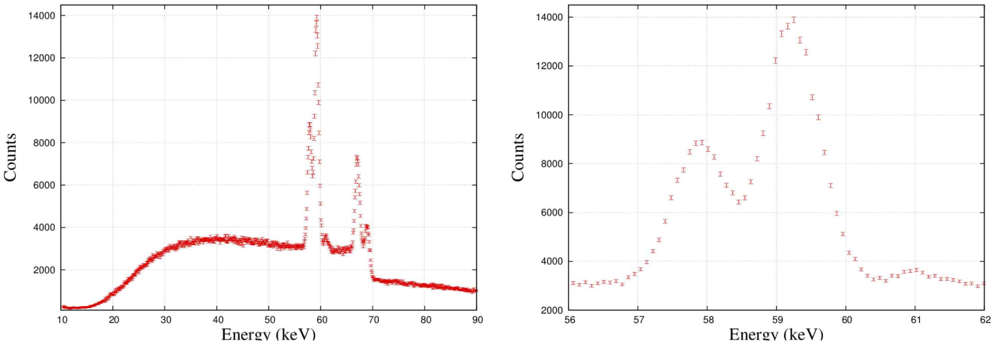

Figure 6.4: *Left*: Polychromatic spectrum of the X-ray tube. *Right*: $K\alpha_1$ line of the spectrum after removing the Bremsstrahlung background.

After measuring the rocking curve of a perfect flat Silicon crystal (111) for various values of the collimator slit aperture and comparing it with the expected value, we have also estimated the beam divergence. By setting the horizontal aperture of the collimator 1 to 0.3 mm and that of the collimator 2 to 0.2 mm (Fig. 6.3), keeping the vertical aperture of both collimators to 2 mm, we have found a good compromise between the brightness of the beam that is impinging on the crystal and the divergence level. With this configuration the resulting divergence value is estimated to be $\mathrm{FWHM}_{\mathrm{div}} = 11 \pm 2$ arcsec, in agreement with the estimate based on geometrical considerations (Fig. 6.6 and Fig. 6.7).

In order to estimate the sample reflectivity at 59.2 keV, we compare the count rate of the incident beam (naturally integrated over all divergence

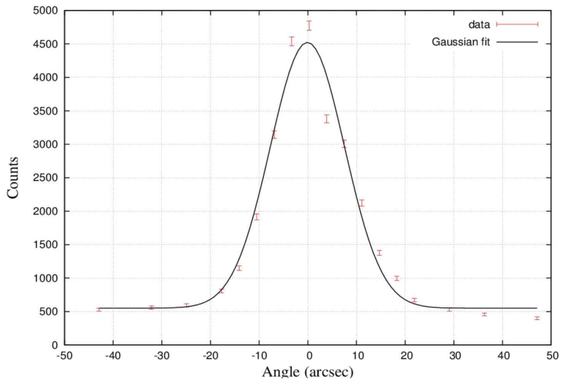

Figure 6.5: Beam divergence corresponding to collimator aperture of 0.3 × 0.2 mm.

angles) with the count rate derived from the crystal Rocking Curve, obtained by rotating the sample in Laue configuration. The crystal samples (Table 6.1) have been tested by setting the X-ray tube voltage to 120 kV with a current of about 1.2 mA. For each sample, both the intensity of the transmitted beam through the crystal and the Rocking Curve are measured. The direct beam is also periodically monitored for possible intensity variations with time.

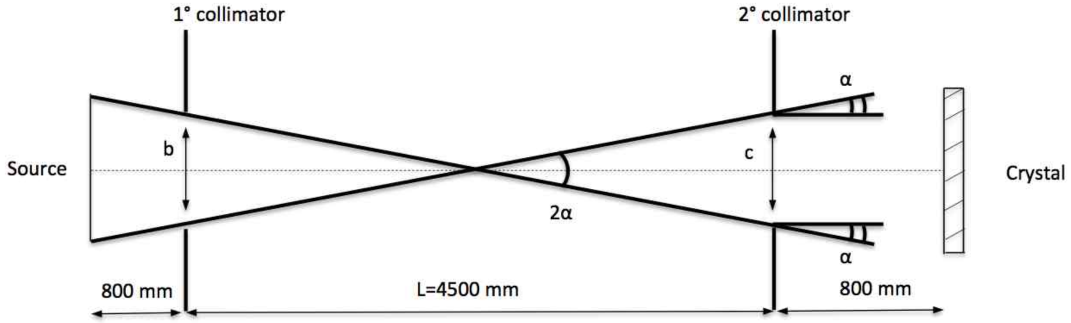

$$\alpha = \arctan\left(\frac{b/2 + c/2}{L}\right)$$

Figure 6.6: Sketch showing the geometrical evaluation of the X-ray beam divergence.

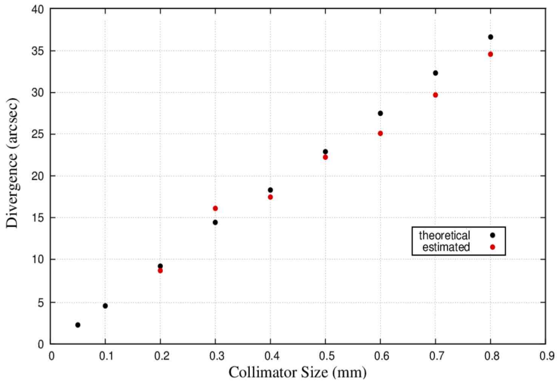

Figure 6.7: Geometric value of the divergence as a function of the collimators aperture.

Two configurations of the crystals have been investigated: *geometry* 1 and *geometry* 2. In *geometry* 1 the beam is impinging on the lateral side of the crystal tile, i.e., the surface in which one of the two sizes is the crystal thickness. Instead, in *geometry* 2, the X-ray beam is impinging on the cross section of the crystal tile. The *geometry* 2 is used for testing the flat and bent mosaic crystals, and the bent perfect crystals in Laue configuration, where a secondary internal curvature of the lattice planes (quasi-mosaic) arises as described above.

Table 6.1: Tested samples

Sample Number	Material	Dimensions mm × mm × mm	Geometry
1	Silicon (100)	15 × 15 × 0.75	Flat perfect
2	Silicon (100)	15 × 15 × 0.75	Perfect bent via surface damaging, 60 m curvature radius
3	Silicon (100)	15 × 15 × 0.75	Perfect bent via surface damaging, 27 m curvature radius
4	Gallium Arsenide (111)	15 × 15 × 2	Flat mosaic
5	Gallium Arsenide (111)	Rounded shape × 2	Bent via surface damaging mosaic
6	Silicon (111)	25 × 25 × 1	Bent via indentation, 60m curvature radius
7	Silicon (111)	25 × 25 × 1	Bent via indentation, 8m curvature radius
8	Silicon (220)	45 × 10 × 3	Stack of 3 bent tiles, 110m curvature radius

Two crystal holders are available. The first is a clamp support (Fig. 6.13), which is employed for testing square or rectangular crystal tiles with a length ranging from 10 to 20 mm and a thickness from 5 to 3 mm. This crystal holder is used for geometry 2 configuration. The other holder is suitable for testing crystals in *geometry* 1. The holder is made of a steal base, on which it is positioned an aluminum wall (Fig. 6.8) that can be moved back and forth along the base, depending on the crystal dimensions. In this way it is possible to rotate the analyzed crystal around the axis of the holder base and to get it within the beam axis.

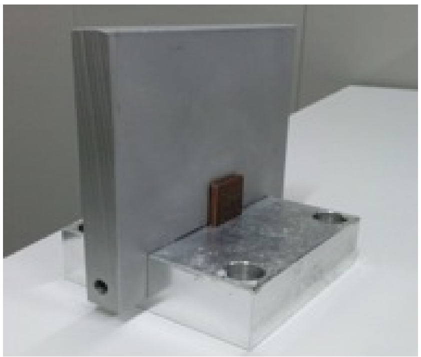

Figure 6.8: Crystal holder for geometry 1 tests.

6.5 Measurements and results

The samples provided by IMEM are listed in the upper part of Table 6.1, whereas the crystals supplied by LSS are listed in the lower part of the same table.

6.5.1 Flat (100) and Bent (100) Silicon crystals (IMEM)

The flat perfect Silicon sample and the two bent Silicon samples (60 m and 27 m curvature radii) provided by IMEM, have the same dimension of 15 × 15 × 0.75 mm^3 with diffracting planes in geometry 2 being the (100). All the samples come from the same ingot, therefore the measurements provide a good comparison of their properties.

We have carried out the integrated reflectivity for each sample by dividing the area under the reflectivity curve, measured using the $K\alpha_1$ line of the incident beam, by the $K\alpha_1$ line total number of photons. The bremsstrahlung background lying under the $K\alpha_1$ line, has been removed for the calculation of

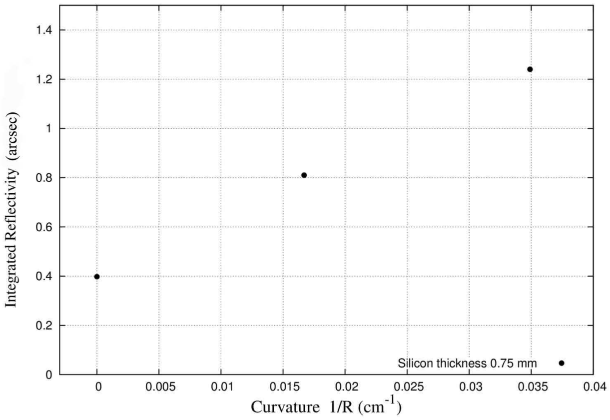

Figure 6.9: Plot of the Integrated Reflectivity, normalized to the incident beam, as function of the crystal curvature for different curvature radii: R=∞,R=60m,R=27m.

the integrated reflectivity (Fig 6.10). As shown in Figure 6.9, the integrated reflectivity at 59.2 keV increases linearly as a function of the crystal curvature, demonstrating that the lapping technique can improve the reflectivity of a flat perfect crystal. For a 60 m and 27 m curvature radius the integrated reflectivity increase by a factor 2 and 3, respectively, with respect to that of the flat crystal. These results appear to be in agreement with those shown in Figure 6.11, where Si crystals in the same geometry are tested by IMEM [61].

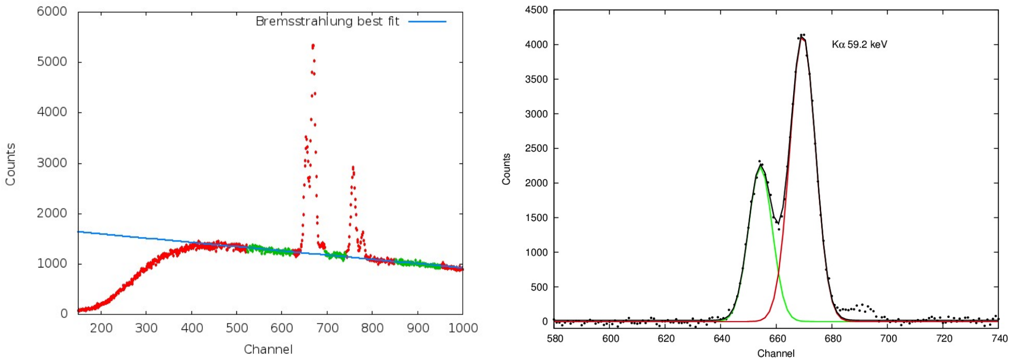

Figure 6.10: *Left*: Best fit of the Bremsstrahlung background of the incident photons spectrum. *Rigth*: Gaussian fit of the $K\alpha_1$ used to estimate the area under the line.

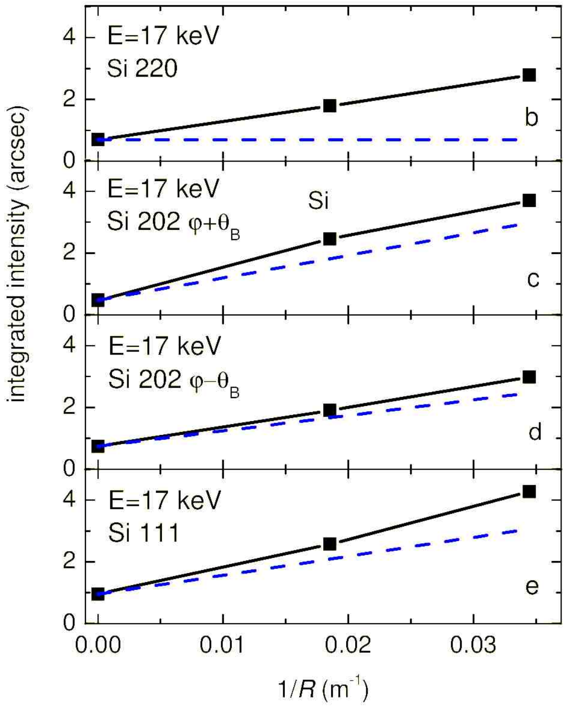

Figure 6.11: Experimental integrated intensities of a flat and two bent Si crystals as a function of crystal curvature 1/R (dots) compared to the linear increase given by the theory for perfect bent crystals [61].

6.5.2 GaAs (111) flat mosaic crystal in transmission configuration (IMEM)

Two GaAs (111) samples were tested, using the clamp crystal support (Fig. 6.13). The tested samples are known to have a mosaicity of about 25 arcsec. Their cross-section is square with dimensions of 15 × 15 mm^2 and thickness of 2 mm. The measurements are found to be consistent with the expectations [59], with a peak of the reflectivity value at 59.2 keV of about 35% and a mosaicity of about 25 arcsec (Fig. 6.12).

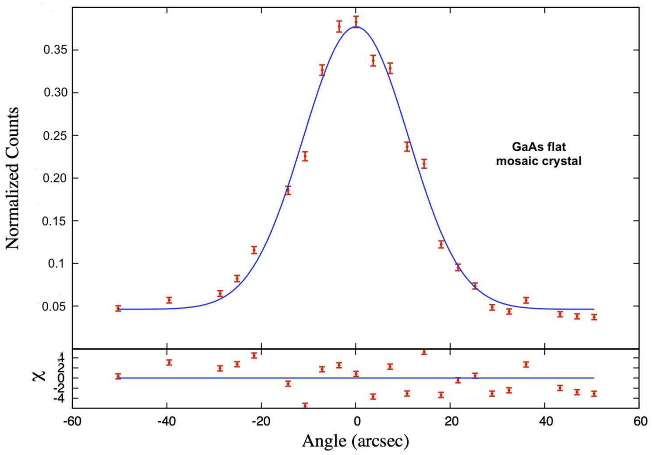

Figure 6.12: *UpperPanel* : The reflection profile of the flat GaAs (111) crystal. *LowerPanel* : The residuals between data and model are shown in units of sigma.

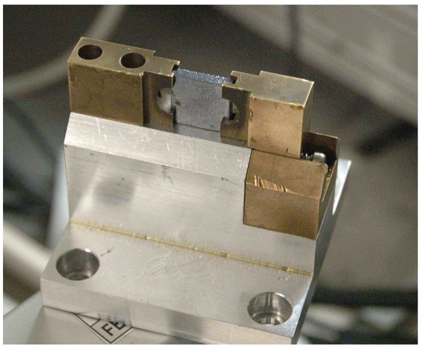

Figure 6.13: GaAs flat mosaic sample mounted on the support.

6.5.3 Bent mosaic crystal of GaAs (111) in transmission configuration (IMEM)

The sample n.5 has a rounded shape with a radius of 35 mm while its curvature radius is 40 m. The tile was mounted on a support and analyzed in the central region in Laue configuration, being (111) the diffracting planes. The measured efficiency (Fig. 6.14) is about 45%, slightly higher than that of the flat sample, consistent with a small increase of the angular spread with respect to the flat GaAs crystal (24.9 arcsec). The curvature does not affect the internal structure and the local mosaic spread does not change, whereas it influences the global behaviour of the sample allowing the focusing effect.

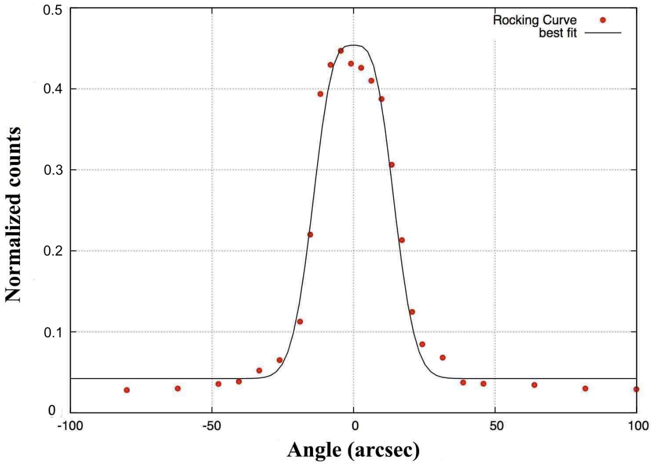

Figure 6.14: Diffraction curve of the GaAs sample (40 m radius) bent crystal.

6.5.4 Stack of bent Silicon (220) crystals (LSS)

The stack is composed of three Si (220) bent crystals, with 110 m bending radius, a front surface of 45 × 10 mm^2 and a thickness of 3 mm. The corresponding plane curvature is 84.4 arcsec. The stack was tested in order to check the misalignments of the crystals with each other. Their bending is obtained by indentations method which, as already mentioned, for some lattice planes gives rise to a secondary curvature (quasi-mosaic) (see Sec. 6.2).

We have tested the sample in two geometries (see Sec. 6.4): 1 and 2.

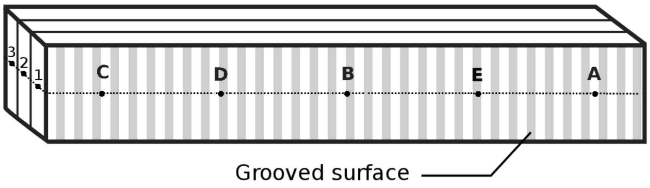

Figure 6.15: Drawing of the Silicon stack with the points tested.

Testing of geometry 1

The configuration of the crystal support adopted for the tests in geometry 1 is shown in Figure 6.16. The diffractivity of the (111) planes (at 59.2 keV) was tested in different points of the lateral surface 10 × 3 mm^2. The incident X-ray beam enters the stack at different distances from the outermost grooved surface (regions 1, 2, 3, see Fig. 6.15 and Table 6.2). The gaussian fit of the measured RCs are very broad and are consistent with the sum of three Gaussian functions (Fig. 6.18). We expected to see a broad peak with FWHM of the order of the crystal curvature, about 84 arcsec. The results reported in Table 6.2 show a similar FWHM value for regions 2 and 3. These values are in agreement with stack angular spread. Instead, for region 1 the FWHM is considerably lower (45 arcsec). We explain this discrepancy in terms of different path crossed by the direct X-ray beam, especially for point 1, where the radiation does not cross completely the stack thickness due to the curvature. When the radiation hits the points 2 and 3, this effect is not present (Fig. 6.17).

Table 6.2: FWHM of the RCs performed.

Region analyzed	Distance from the grooved surface (mm)	FWHM (arcsec)
1	0.4	45.87
2	1.5	87.46
3	2.3	79.12

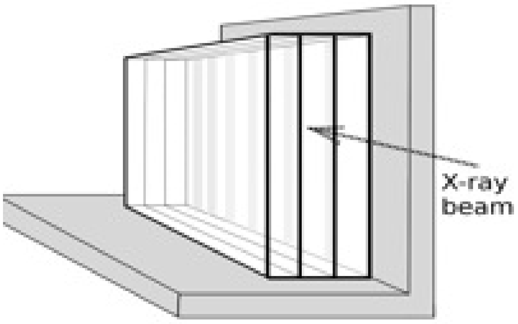

Figure 6.16: Adopted configuration for geometry 1 test.

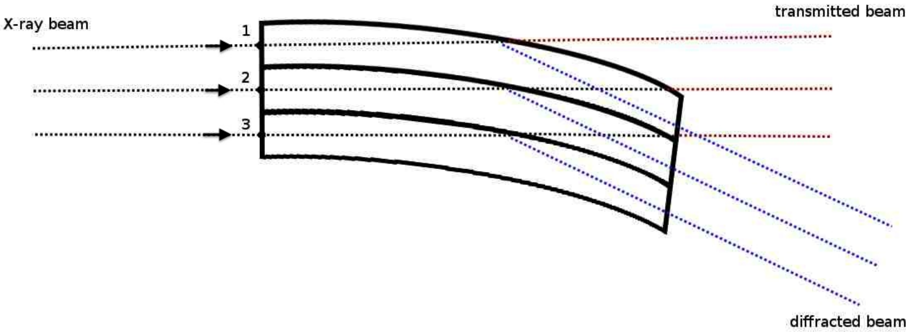

Figure 6.17: Top view of the bent Silicon stack. The different paths crossed by the radiation are also visible.

Testing of geometry 2

The stack in geometry 2 has been also tested. In this case the beam is incident on the grooved surface, with (220) as the diffracting planes, which does not show the quasi-mosaic structure of the (111) planes since, as discussed in Section 6.2, quasi-mosaicity manifests itself only along some diffractive planes depending on the bending direction. The thickness in this case is only 3 mm. Five regions of the cross-section (A, B, C, D, E, in Figure 6.15) have been irradiated.

The test results, (Fig. 6.19) show that the layers of the stack are not perfectly aligned with each other, with the maximum misalignment being

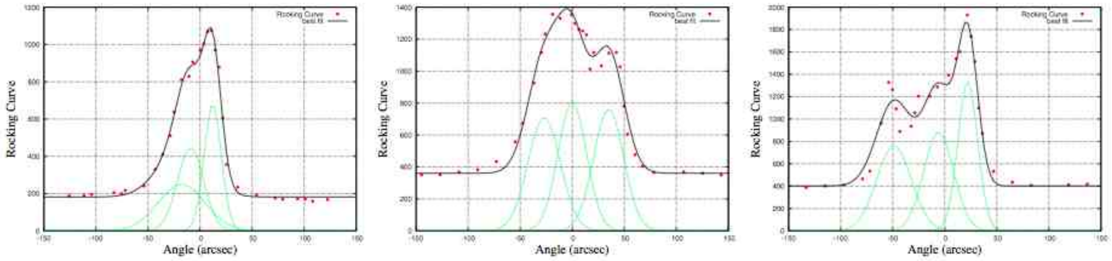

Figure 6.18: RCs (Geometry 1) of the Silicon stack measured in the regions 1 (left), 2 (center), and 3 (right). The RCs have been fit using 3 Gaussian functions, due to the imperfect alignment of the crystals in the stack and to the depth traveled by the direct beam across the layer tested.

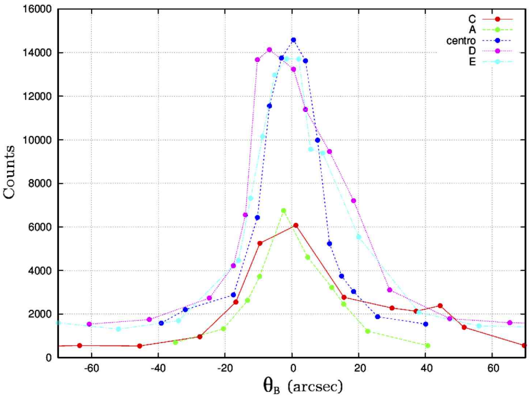

Figure 6.19: Diffracted counts (geometry 2) from different regions (Fig.6.15) of the stack.

more relevant in the external regions (C and A).

6.5.5 Quasi-mosaic Silicon (111) samples in geometry 2 (LSS)

We have also characterized two bent samples via indentation (n.6 and n.7) with a square surface of 20 × 20 mm^2 and thickness of 2 mm, with two different primary curvature radii R_P: 60 and 8 meters, respectively (Fig. 6.20). The diffracting planes (111), in transmission configuration, are orthogonal to the square surface. From the dynamical theory of bent crystals diffraction, the ratio between the internal curvature radius R_{QM} and R_P is equal to 2.4, with a consequent QM curvature of the diffracting (111) planes of 145 and 20 meters, respectively.

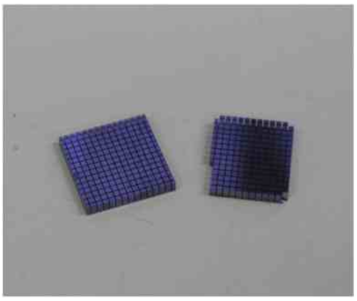

Figure 6.20: The grooved Silicon crystals tested in quasi-mosaic configuration.

From the measured rocking curve we derived an angular spread of 11 ± 2 arcsec for sample n.6. This value is in agreement with the convolution of the bent crystal diffraction profile (box-shape function whose width is driven by the angular spread), FWHM of 2.5 arcsec with the gaussian function of the beam divergence. The measured reflectivity at 59.2 keV is about 80%. Instead, for the sample n.7 which exhibited an angular spread of 20.6 arcsec, a RC width of 21 ± 2 arcsec and a reflectivity value of 25% have been obtained (Fig. 6.21).

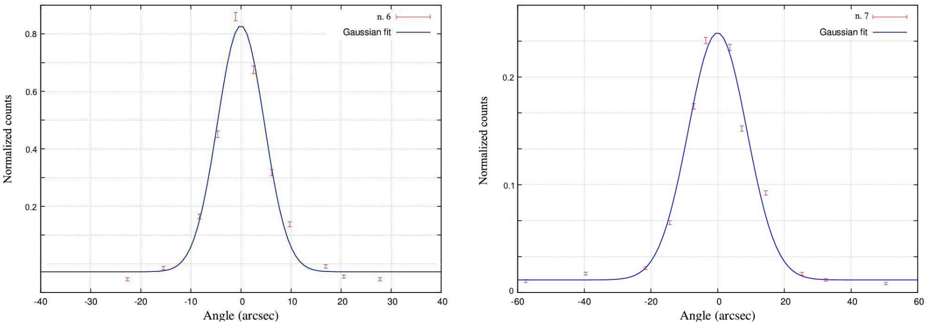

Figure 6.21: Diffraction curves of the Silicon samples n.6 and n.7 respectively.

6.5.6 Discussion of the results

The test of Silicon crystals provided by LSS with different curvature radii and thicknesses have allowed us to establish that Silicon crystals could be successfully employed for the LAUE project.

In order to optimise the crystal thickness in the lens petal passband, simulations of crystal best thickness have been performed. Figure 6.22 shows the best thicknesses, obtained from the crystal diffraction theory [37], as function of the energy along different diffracting planes for both Silicon and Germanium crystals. It can be observed that the best thickness for the Si (111) crystals at 200 keV is $\sim$ 20 mm, whereas the Ge (111) best thickness at the same energy is roughly 6 mm.

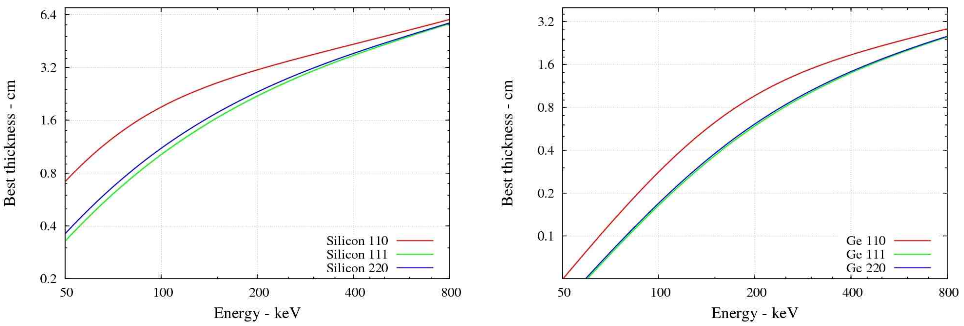

Figure 6.22: *Left*: Bent Si best thicknesses simulated for different diffracting planes. *Right*: Best thicknesses simulation for Germanium bent crystal.

However, the current technological limitations to bend crystals with thickness greater than 2 mm prevent to use them. Germanium tiles, on the other hand, are more appropriate to be used for the LAUE project, given that 2 mm thickness of this material is almost sufficient to achieve the needed diffraction efficiency at high energies (>200 keV). LSS laboratory is able to provide Ge (111) crystals with the required curvature and efficiency.

All the analyzed GaAs samples provided by IMEM show a high-efficiency diffraction, with an average mosaicity that satisfies the requirements of the LAUE project. The curvature radii are in agreement with the theoretical expectations.

Chapter 7

The LAUE Project

As discussed above, Low-energy focusing telescopes up to $\sim$ 70-80 keV have been successfully built or are under development (e.g. NuSTAR and ASTRO-H), but beyond 100 keV an efficient way to focus photons is the use of diffraction techniques from crystals. Laue lenses appear the best solution to focus photons in the hard X-/soft gamma-ray ($<$ 1 MeV) domain. With these lenses, we expect a big leap in both flux sensitivity and angular resolution.

In the following chapter I will present the LAUE project devoted to develop an advanced technology for building a Laue lens with broad energy band (70/100-600 keV) and long focal length (up to 100 m), for space astrophysics. Along with the project description also its main results will be shown. I also describe the developed γ-ray facility, the lens assembly technique adopted, the instrumentation and the measurements performed during the last year of my PhD.

7.1 A focusing lens for soft γ-rays

The LAUE project, supported by the Italian Space Agency (ASI), is a follow-up of the HAXTEL project and is devoted to create a technology to build a Laue lens with long focal length (20-100 m) able to focus photons in the 80-600 keV energy range, unreachable with multilayer telescopes. The experience acquired from the HAXTEL project has shown that, for focal length (FL) longer than 10 m a new assembling technique is needed. Furthermore, a new generation of crystals must be developed for Laue lenses, given that the Point Spread Function (PSF) of a flat crystal is related to the size of the crystal itself. On the basis of these requirements, the LAUE project was conceived to face the following challenging goals:

- to develop an advanced lens assembly technology with a cumulative error budget lower than 10 arcsec, leading to a sensitive Laue lens with long focal length (at least 20 m);
- to solve the still long standing and difficult issue of developing crystals suitable for Laue lenses: explore the use of bent crystals, and their massive production;
- to build a lens petal made of these newly developed crystals;
- to perform a feasibility study of a space lens made of petals.

Concerning the first item, based on the experience acquired with HAXTEL, in order to decrease the cumulative error budget, we decided to develop an apparatus to correctly orient and fix each crystal to the lens frame under the control of a gamma-ray beam. For the same reason, we also decided to keep the lens petal fixed and to move the gamma-ray beam parallel to the lens axis.

Regarding the second item, the development of bent crystals was considered of key importance, in order to increase the reflection efficiency and to obtain a better focusing of the photons.

As of the last two items in the LAUE project, an industrial accommodation study of a modular lens was included. As a result, it appears that an entire lens can be made of petals, and that each petal can be made of sub-petals (or petal sectors). The crystal tiles are accommodated in the petal sectors.

To achieve the first goal of the project, the apparatus sketched in Figure 7.1, where also the reference axes are shown, has been designed. A large distance between X-ray source and lens petal was set to get a low divergence beam. Each diffracting crystal can be translated and oriented in order to focus the beam photons on the lens focal plane. Then it is glued upon the lens frame.

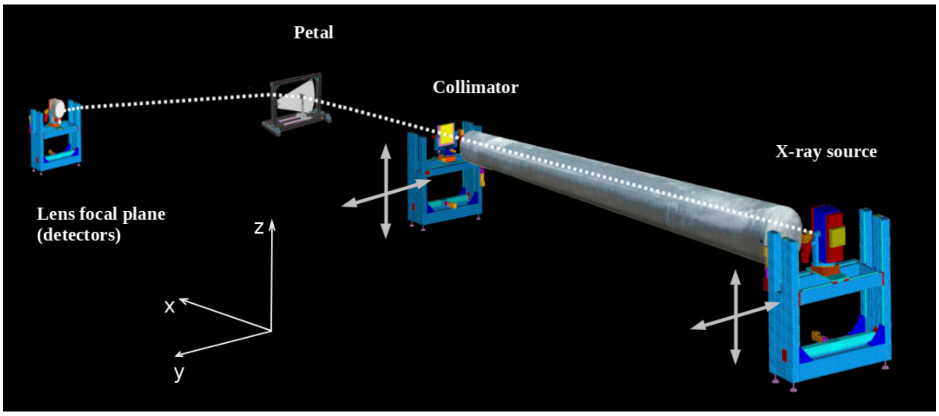

Figure 7.1: Layout of the LAUE apparatus at the University of Ferrara.

7.2 The project apparatus and its location

The entire apparatus for both assembling and testing the lens was designed to be installed in the LArge Italian X-ray laboratory (LARIX) located at the Physics and Earth Sciences Department of the University of Ferrara. The laboratory includes an experimental room (LARIX A) with a 12 m long facility and a 100 m long tunnel.

The 12 m long facility has been already described (see Sec. 5.1). As we have seen, It is also used in the framework of the LAUE project, to qualify each crystal tile in terms of reflectivity and curvature radius for the lens petal to be assembled. The 100 m long tunnel is instead the ideal place for the LAUE project. It allows to obtain a small divergence of the beam impinging on each crystal and to build Laue lenses with long focal length. In Figure 7.2 it is shown a sketch of the tunnel and the relative distances between the installed sub-systems.

The complete apparatus consists of the following sub-systems.

- Gamma-ray source system;
- Beam-line with vacuum environment;
- Clean room with temperature and humidity control;
- Adjustable mechanical slit;

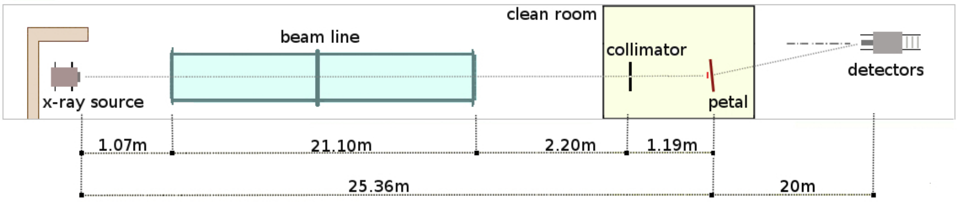

Figure 7.2: Sketch of the tunnel with the relative distances between the sub-systems.

- NaI(Tl) scintillator detector for the incident X-ray flux monitoring;
- Hexapod positioning device and crystal holder;
- Focal plane detectors;
- Translation and rotation systems for the motion of each subsystem (source, collimator slit, crystals);
- Hardware and software needed for the remote control (Ground Support Equipment, GSE).
- Petal frame.

In the following sections I will describe these apparatus components and their implementation.

7.3 The Gamma-ray source and its aperture

A portable betatron and hard X-ray generator are available. The betatron has a maximum electron energy that can be regulated between 1 and 2.5 MeV and could be exploited for testing Laue lenses with nominal passband of 80-600 keV. However for the assembling phase, in the current configuration, is not so bright. Therefore, for the lens petal prototype we have adopted a hard X-ray generator with a maximum voltage of 320 kV, and an X-ray tube with a Tungsten anode (fine focus of 0.3×0.4 mm^2) on which the accelerated electrons impinge for producing bremsstrahlung radiation. The maximum releasable power is ∼1800 W. The expected photon spectrum from the hard X-ray generator and for the current betatron are shown in Figure 7.3.

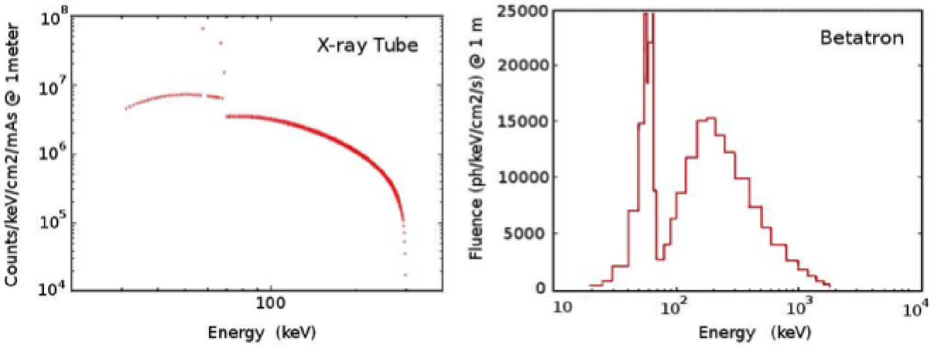

Figure 7.3: Expected photon spectrum (in photons keV^{-1} cm^{-2} s^{1}) at 1 m distance of the X-ray tube (*left*) and from the betatron (*right*).

To reduce the beam width, a 20 mm thick Tungsten shield with a 3 mm diameter hole has been installed in front of the aperture of the X-ray tube. A further collimation is obtained with a drilled (1 mm diameter) 50 mm thick lead collimator on the top of the Tungsten collimator (Fig. 7.4). Source plus collimators can be moved on the plane Y-Z (X being the beam axis). Thanks to the overall collimation, the beam size has been led to an acceptable width and the background level due to the source is also acceptable.

The main properties of the adopted X-ray generator are reported in Table 7.1.

7.4 Beam-line and clean room

The photons coming from the gamma-ray source through the initial collimator, enter into a 21 m long beam-line. This is made of seven 3 m long tubes of stainless steel with an internal diameter of 60 cm. A set of vacuum pumps guarantees a vacuum of at least 1 mbar inside the tubes. The X-ray entrance and exit windows of the beam-line are made of carbon fiber 3 mm thick. The prospect is to extend the beam-line up to 70 m. A view of the already installed beam-line is shown in Figure 7.5.

Figure 7.4: *Left*: The X-ray source that is being used for assembling and testing the lens petal. *Right*: A detail showing the 1 mm lead collimator placed in front of the X-ray tube aperture.

Table 7.1: Main properties of the X-ray tube that is being used for the assembling phase.

RX Tube Type	MRX-320HP/11AX
Nominal Tube Voltage	320 kV
Continuous rating	800W /1800 W
Focal spot size	d = 0.4 mm/ d = 1.0 mm
Filament current, max	4.1 A / 4.6 A
Filament voltage, typical	2.3 V / 6.8 V
Inherent filtration	3 mm Be
Target material	W
Target angle	11^o
Radiation coverage	40^o × 30^o
Leakage radiation, max	5 mSv / h
Cooling medium	Oil
Cooling medium flow, min	14 l / min
Temperature at inlet	50 ^{o}C
Weight	40 Kg

Once the gamma-ray beam exits from the beam-line, it enters in a clean-room (class better than 105, US FED STD 209E Cleanroom Standards). The clean-room is endowed with a thermal control (within 1°C accuracy) and an hygrometric control (relative humidity $\phi = 60\%$ within an error of

Figure 7.5: The 21 m beam line in which is carried out the vacuum for avoiding absorption and scattering.

10%). Components inside the clean-room are the final collimator, the lens petal and the crystal positioning system.

7.4.1 Slit collimator

After the beam-line, the beam impinges on a collimator equipped with a slit with variable aperture to artificially reproduce the presence of a source coming from the infinity. It can be moved together with the X-ray generator along the Y-Z axes. The goal is to have an X-ray beam always parallel to itself and to the lens axis while it is impinging on every crystal tile during the crystal assembling phase. Therefore the collimator is equipped with motors that can translate it in the Y-Z plane and it is provided with three motors to rotate the slit around the X, Y and Z axes.

The collimator has also another important role. It has to shield the beam coming from the source, except that around the beam axis. The shielding is achieved by a lead panel with 200 × 200 mm^2 cross section and 50 mm thick. In the center of the panel it has a 30 × 30 mm^2 aperture window. In correspondence of this window a motorized slit with variable aperture is located. The variable aperture is obtained by means of four crossed and independent 20 mm thick blades made of Tungsten Carbide (density 15.6 g/cm3, 1 % transparency @ 600 keV).

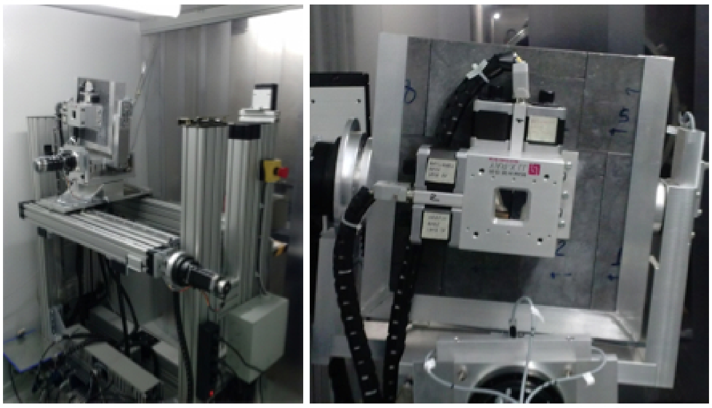

Figure 7.6: Collimator and carriage (*left*) and a detail of the motorised collimator mounted on the 200 × 200 mm^2 lead panel (*right*).

7.4.2 Lens petal frame

The lens petal frame holds the lens crystal tiles. The crystals are properly aligned and placed in the correct position, then glued and fixed on the petal frame. Its total thickness (2.3 mm) is realized with a superposition of 10 layers of carbon fiber. Assuming an interdistance between contiguous crystals of 0.2 mm, we have designed the cell in which each crystal has to be positioned on the frame (Fig. 7.7). In the center of each cell, the frame is drilled, and through the hole the resin is injected for fixing the crystals to the frame. From the location of the cell and the assumed focal length of 20 m, the expected energy in correspondence of the center of each cell is computed.

7.4.3 Crystal orientation and positioning system

The orientation and the positioning of each crystal on the carbon fiber petal frame is performed with a 6-axis hexapod system (Fig. 7.8). The rotation and the linear motion uncertainties are 1 arcsecond and 1 μm, respectively. While the coarse translations along the Y and Z axes are provided by the carriage on which the hexapod is positioned, the hexapod is mainly used for the three fine rotations. The first is the rotation around the beam axis (X) to place each crystal at the nominal position. The other two rotations around the Z' and Y' axes of the crystal rest frame, which in general do

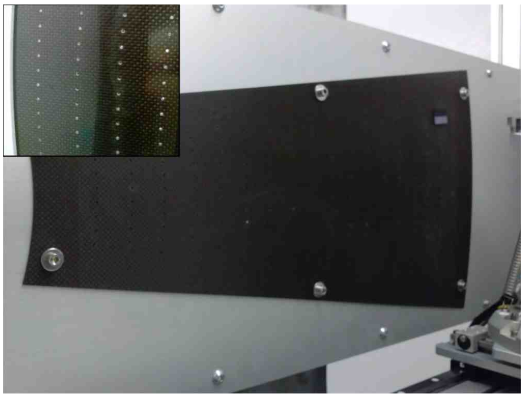

Figure 7.7: The petal frame used as a support for the Laue lens. In the small box is visible a small portion of the petal with the holes through which the adhesive is inject from the back side.

not coincide with the laboratory reference system Y and Z, allow to find the proper diffraction angle. The hexapod is also provided with a further axis (along X) to approach (separate) the crystal to (from) the petal frame. The crystal tile holder has been developed in order to firmly hold the tile and, at the same time, to keep free most of the front and back faces of the crystal, where the incident beam arrives and the diffracted beam is produced. In order to fill as much as possible the lens frame with crystals, the left side of the tile is left bare (see Fig. 7.9).

7.5 Focal plane detection system

A gamma-ray detector system allows to establish the correct orientation of each crystal tile. It is made of two focal plane detectors (a γ-ray imager and a solid state spectrometer) (Fig. 7.10) placed on a carriage at the focal distance of 20 m from the petal frame. The carriage placed on a 15 m long rail, can be translated along the X axis, allowing to place the detectors either on the focal plane or close to the petal structure. The carriage allows also the translation of the detectors in the Y-Z plane with an uncertainties of $\pm$ 0.5 mm in each direction. The X-ray imaging detector (see Table 7.2) has useful area 20 × 20 cm^2, with a spatial resolution 200 μm and an operational energy

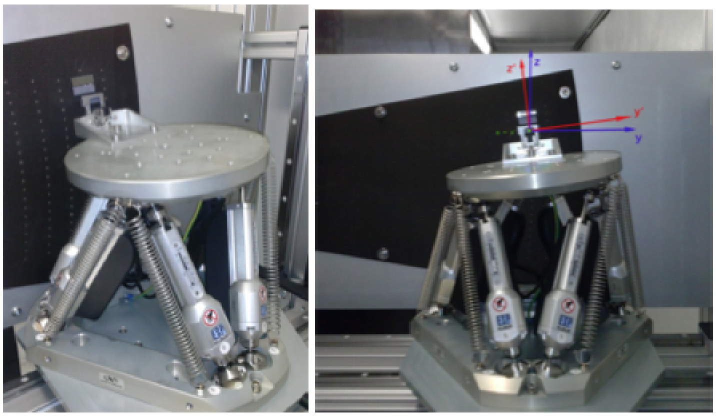

Figure 7.8: *Left*: The hexapod system that is used to tilt and place each crystal in the proper position for the diffration. *Right*: Back view. The reference axes Y, Z and the principal axes of rotation Y', Z' are also reported, referred to a generic crystal slot (position 25).

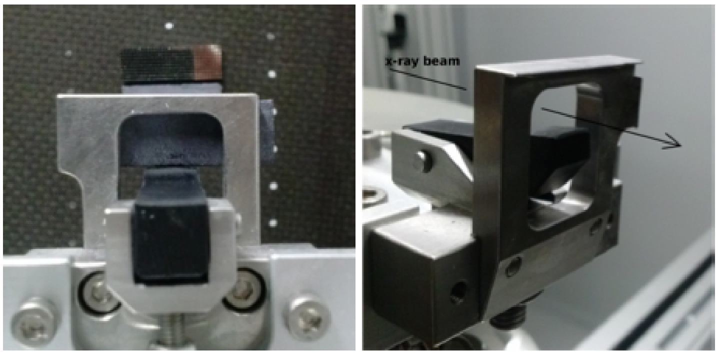

Figure 7.9: Details of the holding system with one crystal made of Gallium Arsenide mounted on it (*left*). A particular of the anchoring borders and the pivot clamping from the bottom (*right*).

range from 20 keV to 15 MeV. It is a flat panel based on a CsI scintillator (0.8 mm thick) that converts the X and gamma-rays into optical light that is afterwards converted into an electric signal from an array of photodiodes. The imager allows to detect the space distribution of the photons in the focal plane, diffracted by each crystal.

The spectrometer is a cooled HPGe detector with 2.5 cm diameter and an energy resolution about 500 eV at 122 keV (see Table 7.3). The spectrometer allows to establish the energy diffracted by each crystal on the lens, given that the centre of each crystal has to diffract a well defined energy. The spectrometer also allows to have a control of the direct and transmitted beam through the crystals, to get an estimate of their reflection efficiency.

Figure 7.10: The focal plane detectors used in the LAUE project: the flat panel detector is positioned below the HPGe detector.

Table 7.2: Main characteristics of the imager detector.

Energy range (keV)	40 keV -15 MeV
Spatial resolution (μm)	200
Active area (cm2)	20.48 × 20.48
Active pixel number	1000 × 1000

Table 7.3: Main parameters of the HPGe detector used for the LAUE project.

Energy range	3 keV - 1 MeV
Resolution FWHM at 122 keV (eV)	537 at amplifier time constant 6 μs
Peak shape FWTM/FWHM	1.86
Semiconductor material	P-type High-Purity Germanium
Dewar capacity	3 l
Static holding time	48 hr
detector cool down time	6 hr
Detector active diameter (mm)	25
Detector sensitive depth (mm)	13
Size (mm^2)	325
Be window thickness (mm)	0.254

7.6 Alignment of the facility

The alignment of the apparatus is crucial for the accurate positioning of the crystal tiles on the lens, thus achieving a fine focusing of the reflected photons. The apparatus alignment was performed through the following three steps:

- **Mechanical alignment**

  The petal frame has been placed within the projection of the beamline cross section (in the Y-Z plane) and perpendicularly to its direction (X-axis). Also the source and the collimator slits have to move within the same cross section. Finally, the detectors have been placed perpendicularly to the X-axis at 20 m from the petal frame. The carriage holding the detectors was designed in such a way that both direct and diffracted beam can be visible.

- **Optical alignment**

  The optical alignment was performed using the beamline without X-ray entrance and exit windows. An horizontal optical laser and an optical equipment that includes a beam-splitter, is positioned between the end of the beamline and the final slit (Fig. 7.11). The optical beam from the laser is first reflected by a mirror to get a vertical beam. Then this beam is incident on the beam-splitter in such a way that opposite beams travel horizontally along the X axis. It is therefore possible to determine the zero positions of the following components: center of the gamma-ray source collimator, final collimator slit, reference hole on the lens frame and focal plane imager and spectrometer zero positions. From the last position, it is possible to determine the lens focus.

The optical alignment ensures that the ideal line connecting the source and the collimator slit is parallel to the lens axis. It also guarantees an excellent precision in the positioning the center of the gamma-ray imager in correspondence of the lens focus.

- **Gamma-ray alignment**

  The gamma-ray alignment performs a fine tuning of the previous alignment process. It has been carried out by means of two Tungsten cross wires (200 μm diameter), one positioned on the center of a dummy crystal located on the crystal holder, and the other on the aperture center of the slit. The position of the reference crystal holder was determined in such a way that the image of the Tungsten cross centre is superimposed on the reference hole image of the lens frame.The final adjustment of the reference positions gave the result shown in Figure 7.12 (right panel).

7.7 Calibration of the incident beam monitor

The monitoring of the beam intensity at the exit of the beamline, before impinging on the slit collimator, is performed using a NaI(Tl) scintillator integrated with a photomultiplier (PMT) plus preamplifier supplied by BICRON, USA (see Fig. 7.13). The detector has a thickness of 4 mm with an X-ray entrance window of 0.2 mm Al, and an energy resolution of about 15% at 122 keV. The strategy was that of measuring the rate between two thresholds, by using a Single Channel Analyzer (SCA). Then, what is needed is the calibration of the SCA lower and upper thresholds. To do that, we used the following electronic chain.

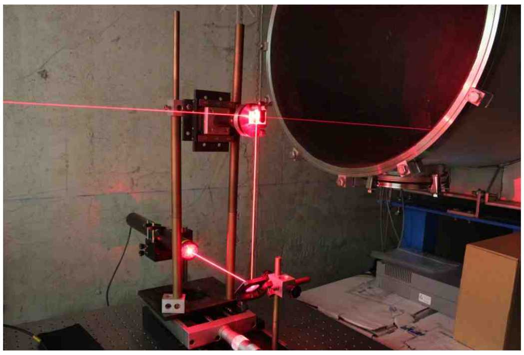

Figure 7.11: The laser equipment adopted for the optical alignment of the LAUE apparatus. The optical beam is made horizontal by a 45° mirror, and the beam splitter provides two antiparallel horizontal beams.

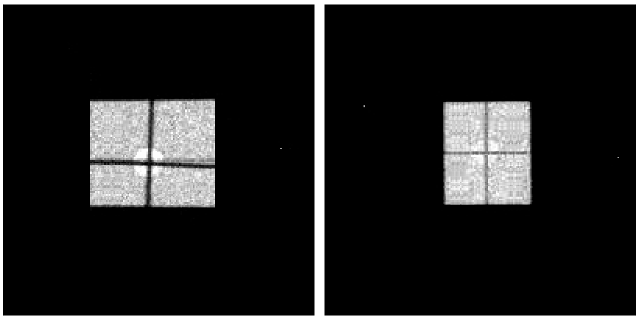

Figure 7.12: Images obtained of the two Tungsten crosses before the fine tuning (*left*) and when the apparatus is fully aligned (*right*). The imager pixel size is 200 μm.

The PMT is powered with a voltage of 0.5 kV by an high voltage power supply (Bertan 353 High Voltage Power Supply), while the preamplifier (PA) is powered to ± 12 V from a ow voltage power supply (EG & G ORTEC Model 4002P Portable Power Supply). The output from the PA is connected to a chain which includes a standard NIM Single Channel Analyzer (SCA Ortec Model 850 Quad Single-Channel Analyzer), an amplifier (EG & G ORTEC Amplifier Research Model 450), an ADC Silena (Mod 7423/UHS 8K ULTRA-HIGH SPEED ADC spectroscopy, series 875), the latter giving the possibility for a coincidence counting between the analog signal and the output signal from the SCA, and a data acquisition card for the digitalized signals (ORTEC MCS-pci plug-in card and MCS-32 software), which allows

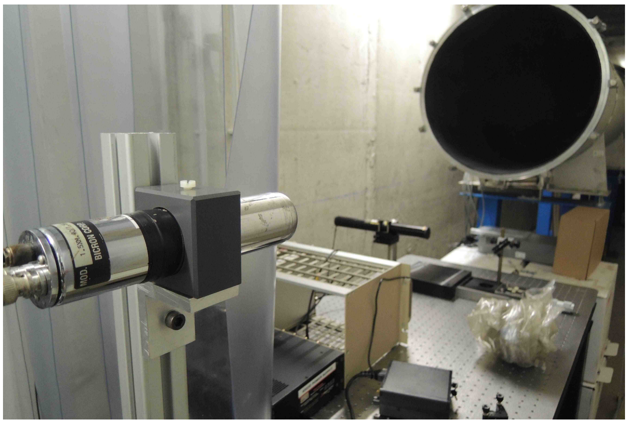

Figure 7.13: The monitor of the incident gamma-ray beam.

the spectral analysis.

The block diagram of the electronics adopted for the calibration of the SCA is shown in Figure 7.14.

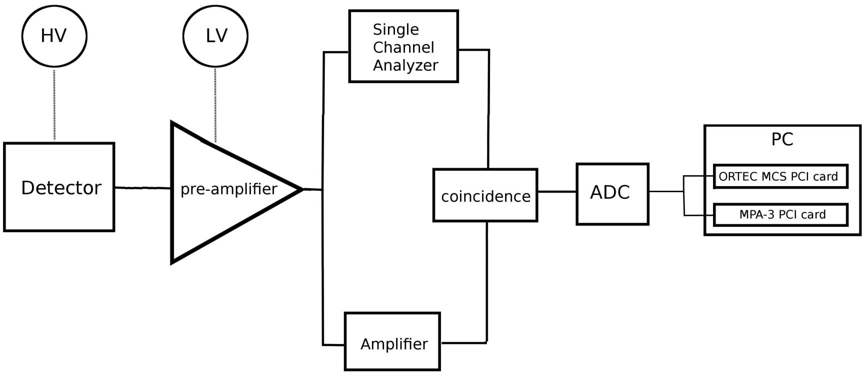

Figure 7.14: Block diagram of the instrumentation.

Essentially, the signal from the PA is sent out to the SCA and, in parallel, to the amplifier. The output signal from the SCA, whenever it exceeds the lower threshold, is being coincided with the output signal from the amplifier. The coincidence events are sent to the ADC Silena, in order to digitizing only the signals from the SCA that exceed the lower threshold. In this way, we get the spectrum detected by the NaI (Tl), whose amplitude is above the lower threshold of the SCA, while the upper threshold of the SCA was set to the maximum value (10 V).

The detector was previously calibrated using a source of ${}_{56}Ba^{133}$ (lines 80.997 keV, 303.09 keV) and ${}_{27}Co^{57}$ (lines 122.06 keV, 136.47 keV). These lines, being defined and strong, present a clear energy profile. With this calibration, the energy-channel relation is found to be:

$$E_i = 0.51 \cdot Ch_i - 4.1. \tag{7.1}$$

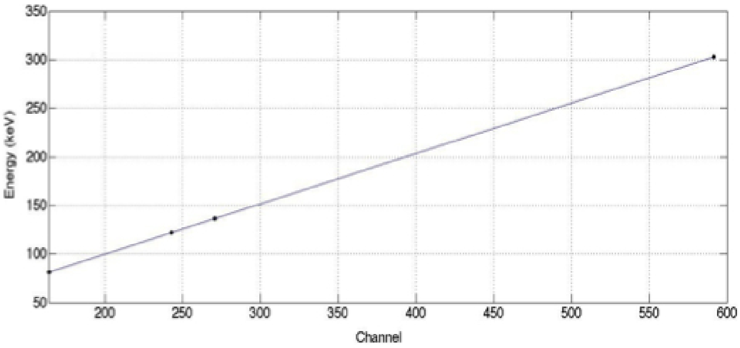

Figure 7.15: The channel-energy calibration.

The calibration of the SCA lower threshold, was performed by changing the voltage of the SCA lower threshold, which is adjustable between 10 mV and 9.99 V (step = 0.01V). The count rate spectrum, of the Ba^{133}, was measured for different values of the lower threshold. Table 7.4 shows the correspondence between threshold voltage and energy.

To calibrate the upper threshold, the counting rate between two adjacent lower thresholds was measured, and found the value of the upper threshold such to obtain the same count that was found between the two lower thresholds.

Figure 7.16 shows that photon energy changes linearly with the lower threshold over the entire range of energies, whereas the upper threshold is linear only in the range 130-300 keV. This non-linearity is not a limitation since the energy band involved in the developing of the project (90 keV - 300 keV) lies almost entirely in the linear region.

Table 7.4: SCA lower threshold calibration.

LOWER THRESHOLD (V)	ENERGY (keV)
0.01	48
0.02	60
0.03	83
0.04	101
0.05	119
0.06	137
0.07	160
0.08	188
0.10	224
0.11	244

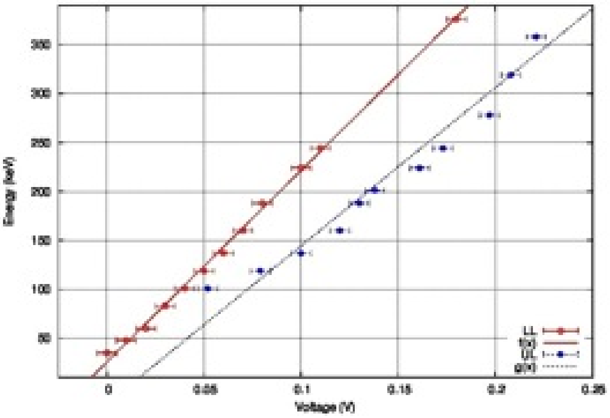

Figure 7.16: Trend of the lower (*red*) and upper (*blue*) threshold as a function of energy. The lines do not pass through zero, as they have an offset of about 0.01 V.

7.8 Ground support equipment

Each sub-system is equipped with a set of linear and rotational stages of motion:

- X-ray source: motorized Y and Z translations, R_Y and R_Z rotations;
- Collimator: motorized Y and Z translations, R_X , R_Y and R_Z rotations;
- Hexapod carriage: motorized Y and Z translations;
- Hexapod: motorized 6 d.o.f. (X translation is allowed manually);

- Detectors: motorized Y and Z translations, R_X , R_Y and R_Z rotations (X translation is allowed manually).

All the motorized carriages are remotely controlled from the control room. For the control of each sub-system, a proper LabVIEW code has been developed [68]. The front-end of the remote management suite is shown in Figure 7.17. A selection of light indicators, e.g. selection of the crystal position on the lens petal, makes the X-ray beam (source and collimator slit) and hexapod/crystal holder automatically moving to the desired position. The remote control of the hexapod is obtained exploiting a dedicated software.

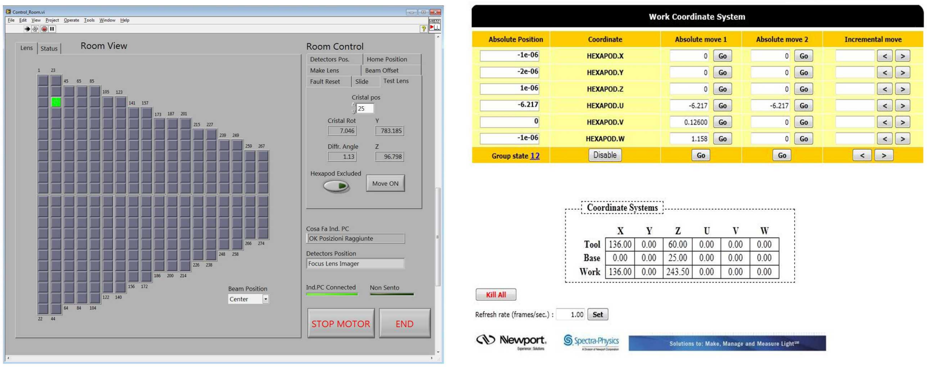

Cristal pos: 25
Cristal Rot: 7.046
Y: 783.185
Diffr. Angle: 1.13
Z: 96.798
Cosa Fa Ind. PC: OK Posizioni Raggiunte
Detectors Position: Focus Lens Imager
Beam Position: Center

Work Coordinate System

Absolute Position	Coordinate	Absolute move 1	Absolute move 2	Incremental move
-1e-06	HEXAPOD.X	0 Go	0 Go	< >
-2e-06	HEXAPOD.Y	0 Go	0 Go	< >
1e-06	HEXAPOD.Z	0 Go	0 Go	< >
-6.217	HEXAPOD.U	-6.217 Go	-6.217 Go	< >
0	HEXAPOD.V	0.12600 Go	0 Go	< >
-1e-06	HEXAPOD.W	1.158 Go	0 Go	< >
Group state 12	Disable	Go	Go	< >

Coordinate Systems

	X	Y	Z	U	V	W
Tool	136.00	0.00	60.00	0.00	0.00	0.00
Base	0.00	0.00	25.00	0.00	0.00	0.00
Work	136.00	0.00	243.50	0.00	0.00	0.00

Refresh rate (frames/sec.) : 1.00

Figure 7.17: *Left*: Front-end of the LabVIEW management software for the remote control of each carriage. *Right*: The dedicated software for the hexapod control.

7.9 Petal features and crystals selection

The lens petal is designed in such a way as to diffract photons in the 90-304 keV energy band. The upper threshold is due to the maximum energy of the photons available with the X-ray tube adopted. The lens petal passband is defined by the inner and outer radius of the lens petal. The crystals will be positioned and glued on the frame so that to focus the diffracted beam at a distance of 20 meters. The width of the designed lens petal subtends an angle of 18°. It is being covered with bent crystal tiles of Ge (111) and GaAs (220) as shown in Figure 7.18. Its main properties are reported in Table 7.5.

Table 7.5: Parameters of the petal that is being build in the LARIX facility.

Parameter	Value		
	section of GaAs(220)	section of Ge(111)	Entire petal
Focal length	20 meters	20 meters	20 meters
Energy range	148 – 304 keV	90 – 267 keV	90 – 304 keV
No. of Rings	14	18	18
Innermost radius	40.66 cm	28.40 cm	28.40 cm
Outermost radius	83.47 cm	83.47 cm	83.47 cm
No. of crystal tiles	119	155	274
Crystal size	$30 \times 10 \times 2$ mm^3	$30 \times 10 \times 2$mm^3	$30 \times 10 \times 2$ mm^3
Crystal mass (total)	2.5 g × 119 = 297.5 g	2.07 g × 155 = 320.85 g	618.35 g

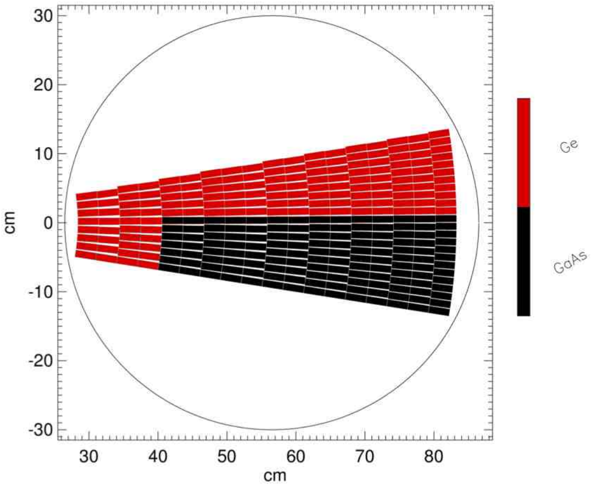

Figure 7.18: The upper part of the petal (*red*) will be filled with Ge (111) tiles while the bottom part (*black*) will be filled with GaAs (220) tiles.

The bent crystal tiles of Ge (111) are supplied by LSS l whereas the bent crystal tiles of GaAs (220) are provided by IMEM.

7.10 Crystal characterization for the LAUE project

In this section I will report the measurement technique which we have developed, to estimate the exact curvature of each tile, within a few percent of uncertainty, and their angular spread or mosaicity. The results obtained are presented. The measurements have been performed with the LARIX A facility.

7.10.1 Adopted method for the curvature measurement

To estimate the value of the primary curvature (also called main curvature) of a sample, we adopted the following method. The sample is held by the moving system that can translate the crystal perpendicularly to the direction (horizontal) of the incident X-ray beam, and rotate it around a vertical axis perpendicular to the beam and passing through the center of the tile itself. Then the crystal diffraction of the monochromatic radiation at 59.2 keV due to the Kα_1 fluorescence of the X-ray tube with Tungsten anode, is analyzed in several crystal points. From the comparison of the spectra of the diffracted beams from each point it is possible to estimate the curvature.

In particular, in the first step it is determined the Bragg angle α, in the point A of the crystal (Fig. 7.19). The crystal is then moved parallel to itself so that the beam impinges on the crystal in a different point B, with distance AB well known. Since the tile is bent, the point B needs a different angle to diffract the same energy as the point A. To get the same diffracted energy (59.2 keV) in correspondence of the point B, we have to rotate the sample by an angle $\Delta\alpha$ which represents the angular aperture between the points A and B. Applying the same procedure to a set of points along the crystal, it is possible to investigate the angular aperture with continuity along the tile, obtaining the mean curvature radius of the crystal itself.

The estimation of the curvature radius is made by performing a linear fit to the different rotation angles measured. Indeed the angular coefficient of the straight line gives the curvature of the sample (Fig. 7.22).

The uncertainty on the curvature radius is mainly related to two uncertainties: the error in the determination of the distance between the contiguous points where the energy of the diffracted beams are measured, and the

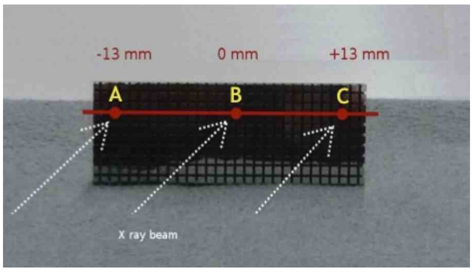

Figure 7.19: The sample is analyzed along several points lying on the same horizontal plane. The same test is performed by raising and lowering the sample, to investigate different areas of the crystal.

error in the determination of the Bragg angle corresponding to the $K\alpha_1$ line. Being Δl the distance between the points, and $\Delta\theta$ the difference between the Bragg angles of the points diffracting the same energy, the curvature radius R and its uncertainty ΔR are given by:

$$R = \frac{\Delta l}{\Delta\theta}, \qquad \Delta R = R\sqrt{\left(\frac{\sigma_l}{\Delta l}\right)^2 + \left(\frac{\sigma_\theta}{\Delta\theta}\right)^2} \tag{7.2}$$

The uncertainty σ_l in the estimation of the distance between the two points is related to the accuracy of the translational stage which moves the crystal and allows the beam to impinge on two adjacent points of the sample. As written above, this accuracy is 1 μm, whereas the typical distance between two successive points is 4-5 mm. It follows that:

$$\left(\frac{\sigma_l}{\Delta l}\right) \sim 2.5 \times 10^{-5} \tag{7.3}$$

Regarding the angular uncertainty, the actuator used has an accuracy of 10^{-4} degrees but the Bragg angle estimation necessary to diffract the desired energy is determined by a Gaussian fit of the rocking curve, which reduces the error to $\sigma_\theta = 2 \times 10^{-5}$ degrees. The variation of the angle $\Delta\theta$ between two adjacent points, being dependent on the distance between the points and the curvature to be measured (approximately 40 m), is of the order of 0.02°:

$$\left(\frac{\sigma_\theta}{\Delta\theta}\right) \sim 0.025 \tag{7.4}$$

From eqs. 7.3 and 7.4 it is evident that the main error comes from the angular uncertainty, while the translational stage error is negligible. The accuracy in determining the angle variation obviously increases if the points to be compared are farther from each other. In this case the difference $\Delta\theta$ between the Bragg angles relative to the points analyzed is greater, whereas the uncertainty in the determination of each point is the same, improving the estimation of the curvature radius. Based on the above considerations we can estimate the curvature radius with an error of about 2 m, for those samples which exhibit a bending radius of 40 meters.

7.10.2 Facility set-up

The measurements have been carried out in the LARIX A facility described in Section 6.4. However, some changes have been made to get more accurate results. In particular, the translation and rotation stages of the crystal holder have been upgraded, achieving an accuracy of 1 μm along a direction perpendicular to the incident beam, and of 3 arcsec for the Bragg angle determination (Fig. 7.20). These movements are monitored with optical encoders. In this way the true position of the sample and the position of the XYZ holder (X being the beam direction) can be accurately measured. The two beam collimators have been adjusted in such a way to provide a beam size of 0.5 mm (along y) × 3 mm and a divergence value of about 18 arcsec. The first collimator does not significantly influence the size of the beam but affects the beam intensity, whereas the second collimator is crucial to get the size of the spot needed for the specific application.

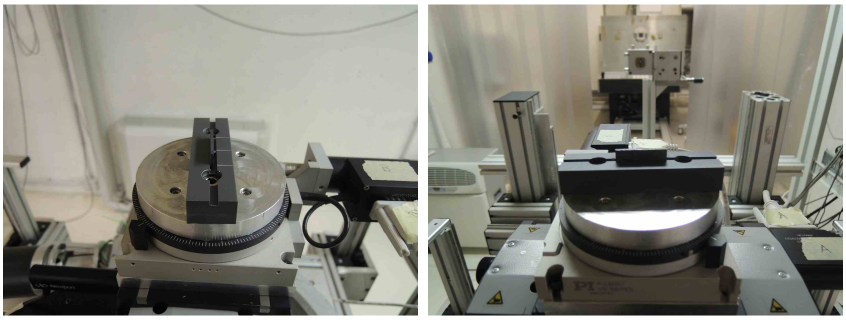

Figure 7.20: The new platform with the upgraded motors

7.10.3 Lens petal crystals

With the developed setup, it is possible to analyze the curvatures of both set of crystals. The crystal tile size of both crystal types as required for the Laue project is 30 mm × 10 mm, with a thickness of 2 mm (Fig. 7.21).

For the lens petal prototype, which is being assembled, LSS has provided all the bent Ge (111) crystal tiles (about 150) with a nominal angular spread of 4 arcsec. 45 of the crystals have been analyzed (see Table 7.6) in order to test the curvature of the indented Ge (111) crystals. The curvature is preliminary measured by the LSS staff means of a profilometer, obtaining a curvature radius of about 40m. However, it is important to take into account that the measured curvature just estimates the profile of the external surface of the single crystals. Instead we have carried out, diffraction tests in transmission geometry, to better investigate the real curvature of the lattice planes. The indented Ge samples are found to show an excellent accuracy in thickness (2÷2.01 mm) and thus in weight (2.06÷2.08 g).

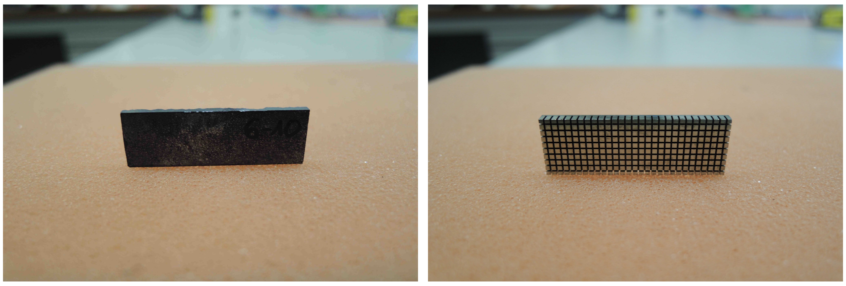

Figure 7.21: *Left*: Gaas (220) crystal tile. *Right*: Ge (111) crystal tile

IMEM has supplied 2 sets of bent crystal tiles of GaAs (220). In order to check the validity of the adopted bending method, the first set of tiles is composed of 10 samples of GaAs (220) with variable thickness (0.45÷0.55 mm) and square cross section (15 mm × 15 mm). The crystal curvature was already measured by IMEM with a Bragg diffractometer, in reflection geometry, making use of a Cu Kα fluorescence line ($\sim$ 8 keV). This set was useful to compare the results obtained by them with those obtainable with the LARIX facility. We found that the samples coming from the same ingot resulted to exhibit a uniform mosaicity (mosaic-spread $\sim$ 15-18 arcsec). In addition, each sample resulted to show two different curvatures along the orthogonal axes x and y.

Concerning the curvature, even if the IMEM team was able to estimate the curvature radius with an accuracy of 5%, this curvature was obtained by the shallow layers of the sample, as their 8 keV beam did not irradiate the deeper regions of the crystal, while adopting transmission configuration, as it can be carried out in the LARIX facility, the results are more reliable.

The second set of 18 GaAs (220) crystals (with mosaicity of 25 arcsec) provided by IMEM, has instead the crystal size required by the Laue project (30 mm × 10 mm × 2 mm). We found that these crystals show a variable crystal weight (2.40÷2.85 g). This is likely due to the different amount of material removed by the lapping procedure.

7.10.4 Curvature measurement results

7.10.4.1 Germanium (111) crystal tiles

All the Ge (111) crystal tiles show a bending radius extremely uniform throughout the crystal, even if in some cases we found a discrepancy between the expected and the measured curvature (Table 7.6). In these cases, if the curvature radius is greater than expected, it has been experimentally demonstrated by LSS that, by increasing the grooves depth the curvature radius can be decreased. On the other hand, if the curvature radius is smaller than expected, the crystals can be further exposed to an etching procedure to relax the stress and increase the tile curvature radius. Therefore the crystal curvature can be refined achieving an accuracy of 5%. Some examples of the crystal curvature measured by us are given in Fig. 7.22. Figure 7.23 shows one of the rocking curves that have been carried out for some Ge samples, in order to investigate their angular spread.

Table 7.6: Curvature radii of the Ge (111) samples analyzed for the LAUE project.

Sample Number	Measured curvature Radius (m)	Crystal Number	Curvature Radius (m)	Crystal Number	Curvature Radius (m)
8	44.7	29	43.0	58	41.8
9	44.2	30	40.5	68	42.8
10	37.4	31	37.4	71	43.7
11	44.3	32	26.0	72	44.7
13	44.7	33	40.5	73	43.1
14	37.3	34	43.3	80	37.9
15	40.5	35	42.7	81	38.4
16	38.5	36	38.0	82	44.2
17	41.8	37	33.0	83	30.4
21	39.5	47	54.5	92	40.9
24	46.4	48	45.7	94	52.6
25	51.1	49	39.4	94	52.6
26	47.7	50	41.3	119	39.3
27	43.5	51	42.3	126	47.0
28	41.5	56	41.2	153	44.3

7.10.4.2 Gallium Arsenide (220) crystal tiles

The first set of crystals supplied by IMEM (not for lens petal) has shown a good agreement between the results obtained using the reflection diffractometer and the transmission geometry adopted in the LARIX facility. Table 7.7 reports the results obtained by IMEM compared with those obtained in the LARIX. With the exception of the curvature along the y axis measured for the sample number 3 (whose curvature radius is very small, therefore unsuitable for the project) for which we obtain a discrepancy between the two measures greater than 10%, the measured curvature radii, along both x and y axes, agree with each other within an uncertainty of 5%.

The set of crystals provided by IMEM for the Laue project are listed in Table 7.8, where the results obtained at IMEM and LARIX laboratory are also reported. An example of rocking curves obtained by us, which is used to estimate the crystal mosaicity, is shown in Fig. 7.25. As can be seen from Table 7.8, the discrepancy between the LARIX and IMEM estimates for this set of crystals, is greater. This discrepancy likely is due to the fact that IMEM measures the reflected beam, while we measure the diffracted beam in transmission geometry, and also to the non-uniform curvature of

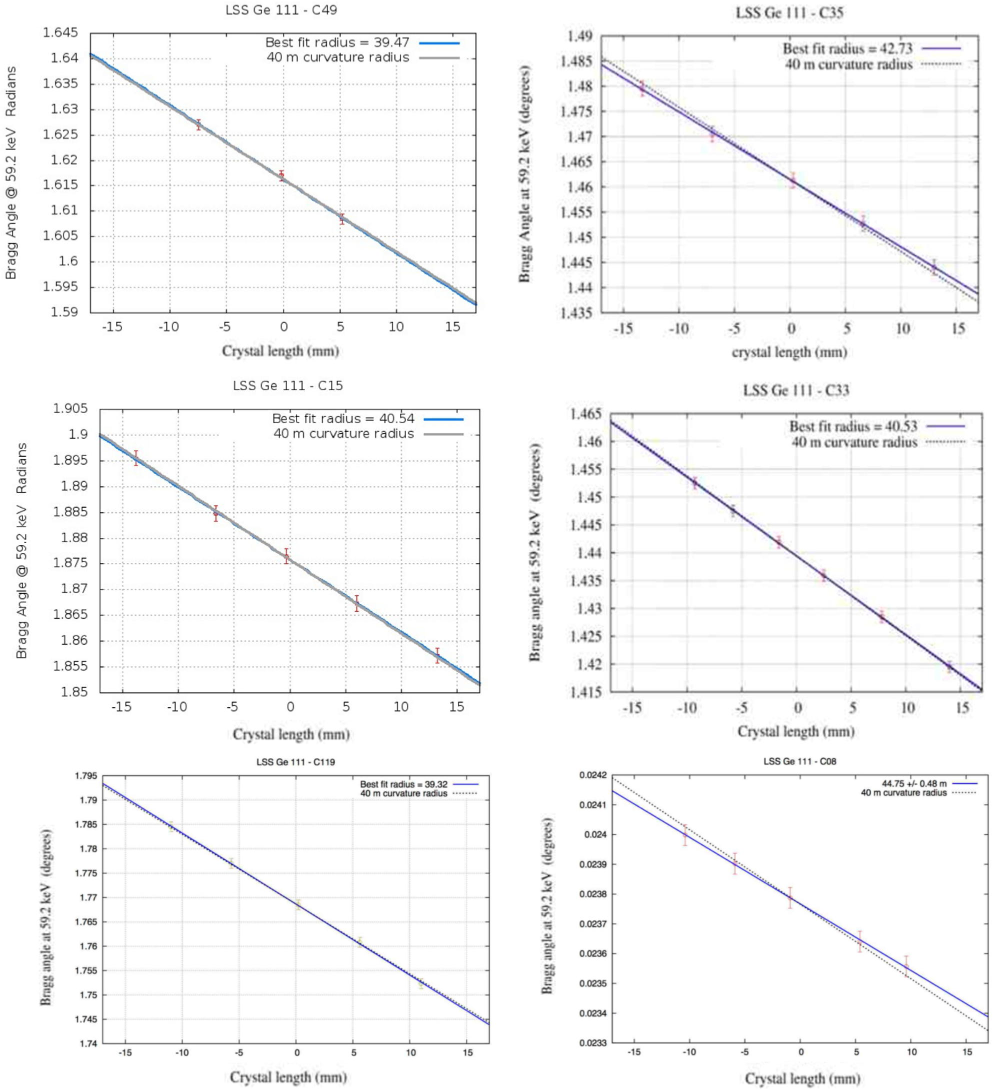

Figure 7.22: Bending estimations for different samples of Germanium. The measured radii are compared with the expected curvature (40 m). The x and y axes show respectively the distance from the center of the crystal (zero), and the angle required to diffract the 59.2 keV photons.

the GaAs samples due to the presence of dislocations. Furthermore, a non-uniformity for some of the GaAs samples is observed at the edges of the tiles (an example is the crystal C03 in Figure 7.24), if compared to the Germanium samples. Figure 7.25 shows the rocking curve of a GaAs crystal.

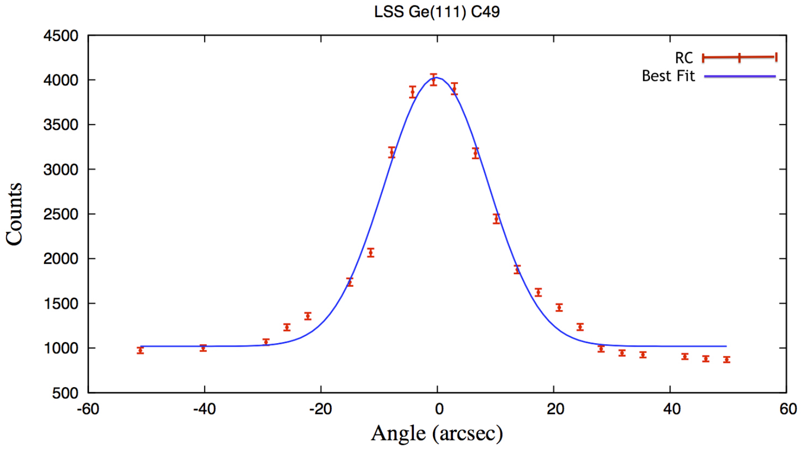

Figure 7.23: Bent Ge (111) rocking curve as recorded at the LARIX facility. The FWHM of the gaussian fit turned out to be 24.6. The broadening of the diffraction profile (FWHM 4 arcsec) is mainly due to the beam divergence (18 arcsec), which is also responsible of the gaussian shape.

Table 7.7: GaAs(220) bending radii of the samples analyzed for the LAUE project (n.t. means "not tested").

Sample	Thickness	Grain-paper	IMEM		LARIX		Deviation (%)	
			Rc x	Rc y	Rc x	Rc y	IMEM-LARIX	
Number	(mm)		(m)	(m)	(m)	(m)	x-axis	y-axis
1	0.495	P2500	13.8	66.7	14.3	67.9	3.5%	1.8%
2	0.440	P600	6.0	23.3	n.t.	22.8	-	2.1%
3	0.460	P320	5.2	16.2	5.8	n.t.	10.9%	-
4	0.502	P4000	20.3	60.0	20.6	59.6	1.5%	0.7%
5	0.420	P180	3.1	7.4	n.t.	n.t.	-	-
6	0.445	P1200	7.4	29.2	n.t.	30.3	-	3.6%
7	0.435	P400	5.6	10.6	n.t.	11.0	-	4.1%

The profile of the recorded rocking curve is the convolution between the beam divergence function and the intrinsic diffraction profile of the crystals. By deconvolving these two function it is possible to get the intrinsic rocking curve, corrected for the beam divergence. In this way we have estimated the mosaicity for some samples, and the results are in agreement with the expectations (Table 7.8).

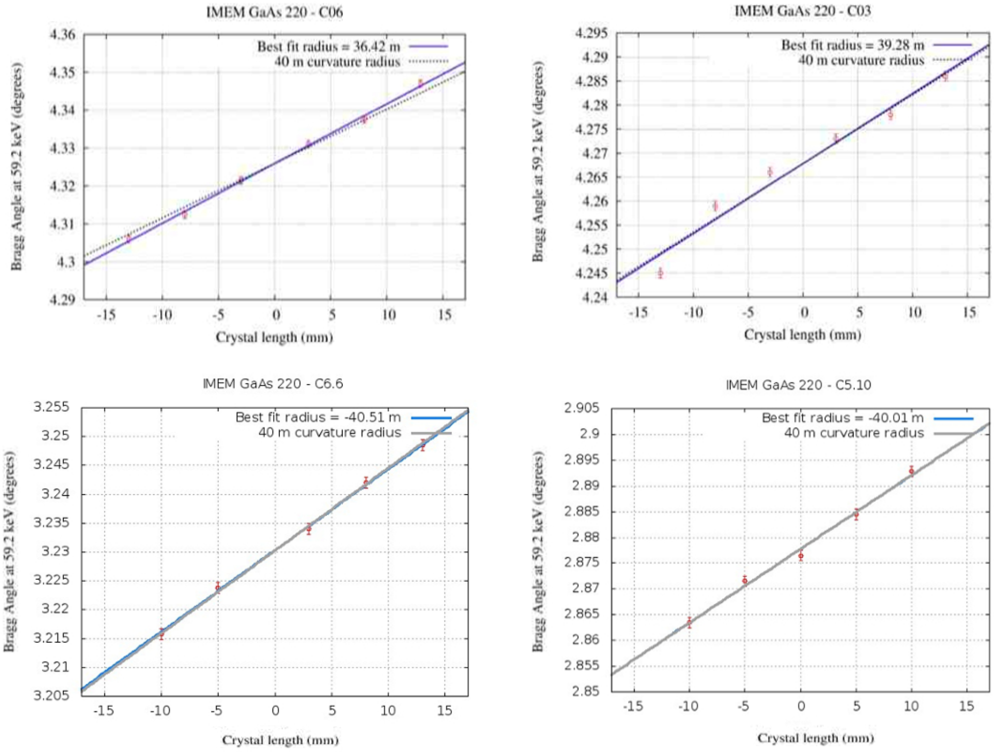

Figure 7.24: Bending estimations for some samples of GaAs. The measured radii are compared with the expected curvature (40 m). The x and y axes show respectively the distance from the center of the crystal (zero), and the corresponding 59.2 keV Bragg angle.

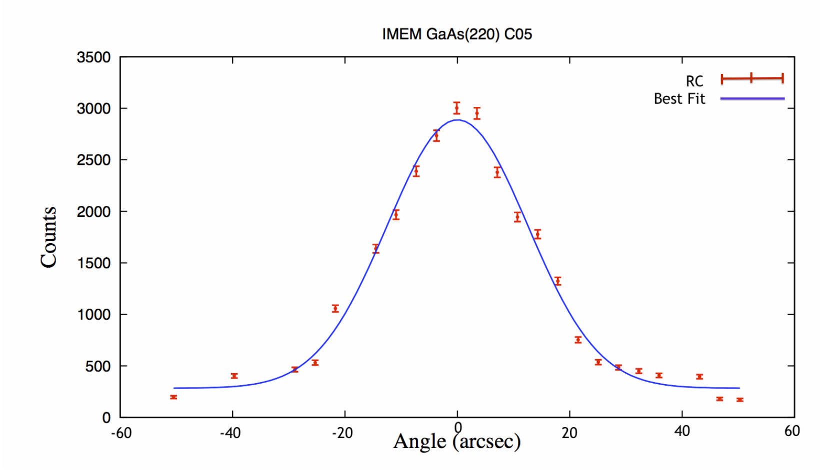

Figure 7.25: Mosaic GaAs (220) rocking curves as recorded at the LARIX facility. The FWHM (31.2 arcsec) of the gaussian fit in this case, as we expect, is greater than Ge (111) crystals. After the correction of the beam divergence, the mosaicity value obtained was ∼ 25 arcsec.

Table 7.8: Curvature radii of the second set of GaAs (220) samples provided by IMEM.

Sample Number	Weight (g)	Rc IMEM	Rc LARIX	Deviation (%) IMEM-LARIX	Mosaicity (arcsec) LARIX
1	2.40	40.3	35.0	13.9%	25.5
2	2.05	42.4	39.5	7.3%	27.4
3	2.66	41.9	39.3	6.5%	23.6
4	2.67	38.8	39.2	1.1%	21.2
4.8	2.55	39.4	35.9	8.75%	-
4.9	2.62	38.7	36.3	6%	-
5	2.85	40.0	38.2	4.5%	25.2
5.2	2.35	40.0	39.9	0.2%	-
5.10	2.42	40.0	40.0	-%	-
6	2.60	40.0	36.5	9.2%	23.4
6.4	2.65	40.0	38.9	0.2%	-
6.6	2.62	42.0	40.5	3.75%	-
6.10	2.52	38.8	36.8	5.0%	-
6.11	2.60	38.6	34.7	9.7%	-
6.12	2.55	41.1	42.38	3.2%	-

7.10.5 Discussion of the results

With the performed curvature measurements, we have established the real curvature of the crystals produced for the lens petal prototype.

Concerning Ge (111) crystal tiles, we have found that only 36% of the tested tiles have a curvature radius of 40 m within 5% as requested, while 60% of the tiles have a curvature radius of 40 m within 10%. In Figure 7.26 it is shown the distribution of the measured curvature radii. For those crystals with a curvature radius that does not satisfy the requirement, a further refining step is requested.

Concerning GaAs (220) crystal tiles, due to the small number of tested crystals it has not been possible to make a similar statistical analysis to make an inference about the goodness of the tiles provided (see Fig. 7.27). However, from the results obtained we can see that 44% of the samples tested have a curvature of 40 m within 5%, whereas the curvature of 83% of the tiles is 40 m within 10%.

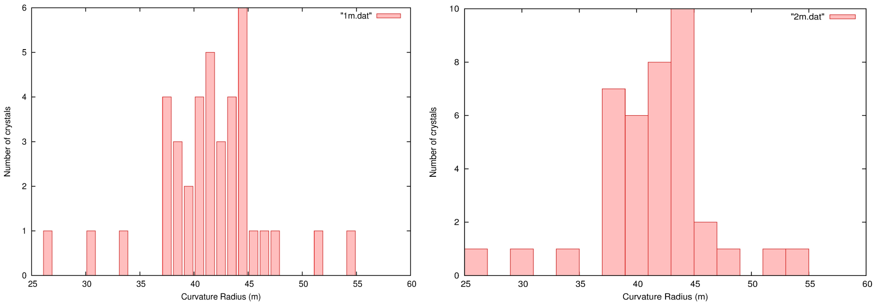

Figure 7.26: Distribution of the bending radii of the 39 Ge (111) samples analyzed, with a rebinning of 1m (*Left*) and 2 m (*Right*).

Together with the measurements of the crystal samples, a series of simulations were performed [69] in order to determine the maximum acceptable radial distortion with respect to the nominal curvature radius. In Figure 7.28 it is shown the dependence of the Full Width at Half Maximum (FWHM) of the Point Spread Function (PSF) on the crystal deviation from the nominal curvature (40 m), for a lens entirely made of either Ge (111) (red curve) or GaAs (220) (green curve) crystals. The simulation shows that for a distortion equal to zero (the ideal case), the FWHM is equal to 0.6 mm in the

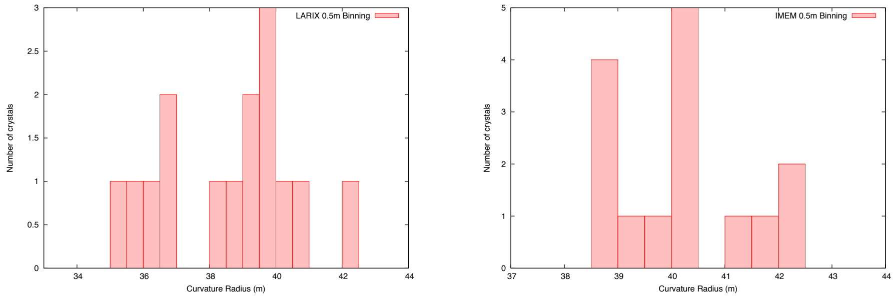

Figure 7.27: *Left*: Distribution of the bending radii of 15 GaAs (220) samples as estimated at LARIX facility. *Right*: Distribution of radii as obtained at IMEM Parma.

case of Ge perfect crystals, whereas it is equal to 3.4 mm using mosaic GaAs (220) tiles. Despite the Germanium PSF rapidly grows with the increasing distortion, it is always smaller than that of GaAs whose size seems to be almost constant. Therefore a small distortion is needed for a lens made of Ge (111) crystals.

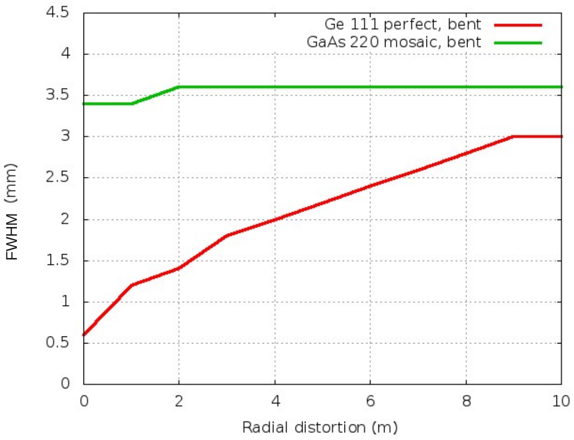

Figure 7.28: PSF size (FWHM) of an entire Laue lens (focal length of 20 m) having a 50-600 keV passband, composed of Ge (111) (red curve) or GaAs (220) (green curve) crystals as a function of the deviation of the crystal curvature from the 40 m bending radius.

7.11 LAUE project first results

The first results from the lens petal prototype concern the diffracted beam coming from two crystals (one of Ge (111) and the other of GaAs (220)), assembled on the petal frame. On the petal frame 274 cells, distributed over 18 rings, are available where to place crystal tiles. Each crystal tile belonging to a given ring, diffract photons with the same energy band. The selected crystal cells #24 and #25, are part of the ring n. 2 (Fig. 7.29), whose nominal diffracted energy centroids are 96.14 keV and 157.10 keV for Ge and GaAs, respectively.

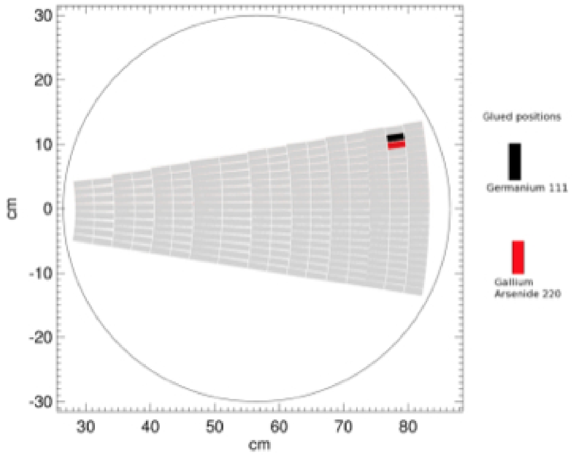

Figure 7.29: The tested Ge (111) and GaAs (220) crystals positioned in the cells #24 and #25 on the lens petal.

Through the spectral analysis we have checked whether the correspondence between the expected and diffracted energy by the tiles is correct. As can be seen from Figure 7.30 (left), the diffracted spectrum of the tested Ge (111) tile, has its peak at $\sim$ 96 keV. This value is what we expected for a crystal positioned in such a cell. The same result was obtained for the contiguous GaAs (220) crystal Fig. 7.30 (right).

A systematic monitoring of the diffracted beam was performed during the gluing phase. The spectrum was acquired every 15 minutes after the resin injection. Figure 7.31 shows that the effect of the glue polymerization does not produce any significant deviation of the centroid energy with respect to

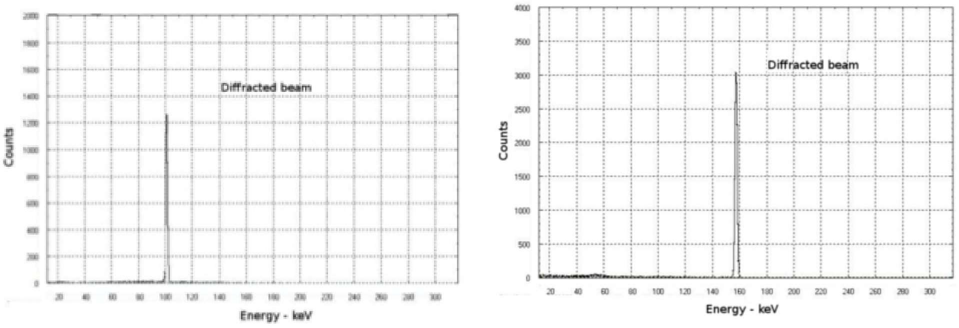

Figure 7.30: *Left* : Diffracted spectrum by the Ge (111) crystal. *Right* : Spectrum of the diffracted photons from the GaAs (220) tile.

the nominal energy expected for the GaAs (220) placed in the cell #25.

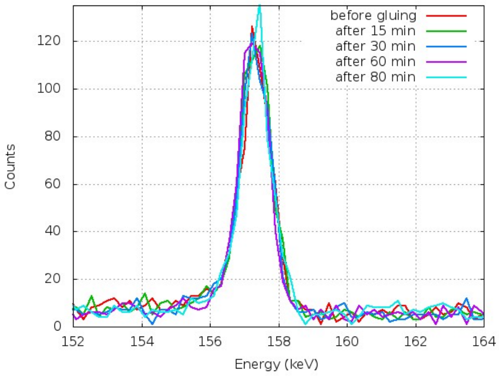

Figure 7.31: GaAs (220) spectra obtained during the 80 minutes monitoring.

After the glue polymerization we have verified whether the holder removal, which is the most critical phase, introduces some change in the energy centroid. Actually a shift, less than 1 keV, in the centroid energy has been observed, corresponding to a changing of $\sim$ 20 arcsec in the crystal orientation. Figure 7.32 shows the measured spectra before and after the holding removal. The effect is mainly related to the angular tilt between the petal frame and the glued crystal plane. The tilt produces an asymmetric glue distribution over the crystal, giving origin to the observed energy change. The same effect was also observed during the preliminary resin tests in which the orientation of 20 muck-up tiles of 30 × 10 mm^2 cross section was monitored during their polymerization phase. A systematic deviation of 20-30 arcsec was found. This systematic error is being taken into account during the assembling phase of the crystal tiles on the petal frame.

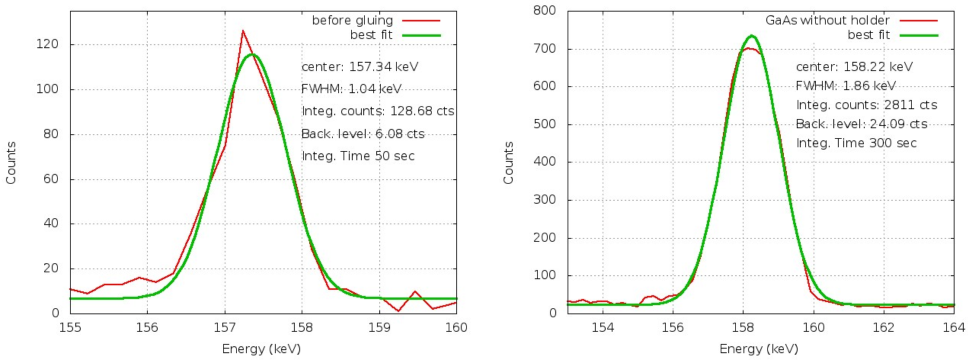

Figure 7.32: Diffracted spectra of the GaAs (220) before (*left*) and after (*rigth*) the mechanical release of the holder. The difference is visible in terms of energy deviation from the nominal position. After the holding removal the energy deviation was within 1 keV, corresponding to ∼ 20 arcseconds.

The diffracted beam by the crystals has also been observed through the imager detector placed in the nominal lens focus. After setting the slit aperture to 4 × 6 mm^2 in order to reduce the divergence (few arcsec), the image of the diffracted beam shows the distinctive focusing effect of bent crystals. The tile focusing capability can be observed in Figure 7.33 in which the radial dimension has decreased from 4 mm in correspondence of the crystal to 2 mm at the detector level due to the focusing capability of the lens. In the orthogonal direction, a non focusing effect is expected and, indeed, in this case the beam increases from 6 mm to 12 mm as expected due to the beam divergence.

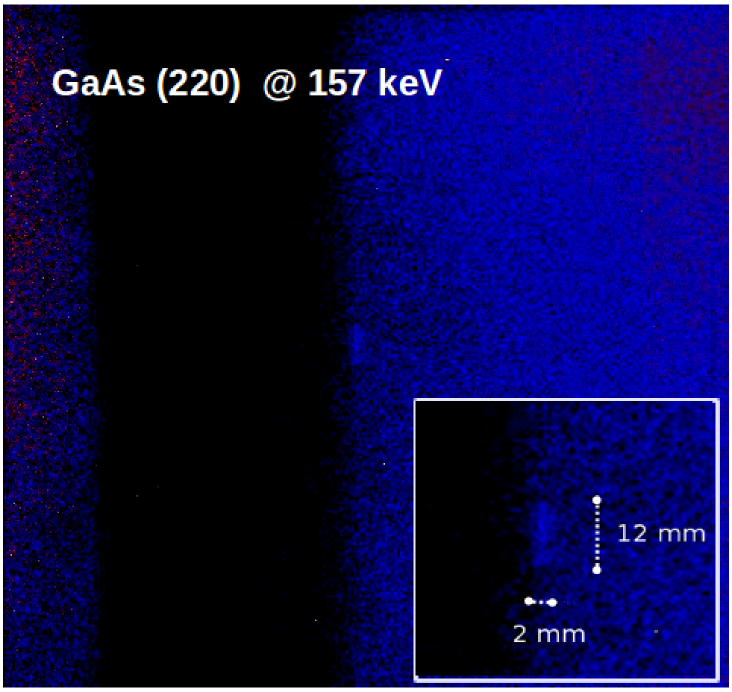

Figure 7.33: GaAs (220) diffracted image. The focusing effect along the horizontal direction is visible.

Chapter 8

Conclusions and Prospects

The LAUE project results are very promising for the prospects of the hard X-ray astronomical observations (up to 600 keV). The accuracy with the adopted lens assembling method has turned out to be what we expected, allowing the building of a Laue lens petal with a precision in the crystal positioning of 10 arcsec.

Also the tests of the bent Ge (111) and GaAs (220) crystals, for the first time used for a γ-ray focusing telescope, are consistent with the expectations, opening a new window in the realization of a Laue lens for astrophysical applications thanks to their high efficiency and focusing capability.

I have reported some possible astrophysical open issues that can be faced by a satellite mission based on Laue lens, showing that for the first time we can achieve unprecedented goals and make unexpected discoveries thanks to the high sensitivity, which is expected to be about 2 orders of magnitude better than the current instrumentation at the same energy [64].

In the framework of the LAUE project, a feasibility study has demonstrated that a Laue lens made of petals is feasible. Another advantage of the Laue lenses is their very low weight, much lower than that of the direct view instruments currently adopted and focusing telescopes based on grazing reflection.

Further improvements in Laue lens building are expected in the crystal bending techniques, that can extend the thickness of bent crystals to values greater than 2 mm. Thicker bent crystals could extend the passband of Laue lenses up to about 1 MeV, with a great increase in sensitivity for nuclear astrophysics.

Appendix A

Research Activity at ESRF

A.1 Introduction

In order to deepen experimental aspects of diffractometry and its most advanced applications, during the last year of my PhD I have carried out, for three months, a research activity at the European Synchrotron Radiation Facility in Grenoble. I have been working at ESRF as a Research Fellow within the framework of a collaboration agreement between the "Universita Degli Studi di Ferrara" and the ESRF, under the scientific supervision of Dr. Roberto Verbeni. The collaboration was with the group Detector & Electronics of the Experiments Division.

In the following section I will present the activity carried out at the ESRF which mainly focused on the installation and commissioning at beamline ID20, and on the realization of spherical crystal analysers, with the opportunity to have practical experiences on the X-ray related instrumentation.

A.2 The ID20 upgrading project (UPBL06)

In the period I have been at the ESRF I took part to the installation and commissioning of the beamline ID20, which was being upgraded (UPBL06 project) for the inelastic X-ray scattering (IXS) programme dedicated to the study of electronic excitations. The main idea of the upgraded design is to strengthen the advantages of IXS providing:

- two spectrometers for studies of electronic excitations optimized for high efficiency with medium energy resolution (flexible in the range 300 meV - 1 eV) and for high energy resolution applications (100 meV), respectively;
- an intense, stable beam focused down to 8×16 microns (V × H) leaving at the same time enough free space around the sample for complex sample environments;
- an optical scheme to extend the energy range of applicability of the technique for studies of electronic excitations from the 6-10 keV interval used today to the 5-20 keV range.

The high-efficiency, medium energy-resolution spectrometer will be optimized for X-ray Raman Spectroscopy (XRS), a rapidly developing, powerful technique in chemistry, physics, and materials science. More specifically, XRS can be used in circumstances where soft X-rays are unusable, e.g. high pressure studies. This will be of particular interest for geophysical investigations.

The high-resolution spectrometer foreseen within the UPBL06 project will instead be optimized for resonant IXS (RIXS) in the hard X-ray range. Indeed, RIXS is a powerful tool for studying electronic excitations in solids giving access to site, element, and orbital selective information.

Another very important aim of the UPBL06 project is to push non-resonant IXS experiments towards energies higher than those where they are currently performed (6-10 keV). The present limitations are imposed by technical reasons (mainly energy resolution), and can be overcome by the development of crystal-analyzers made of Ge, thus allowing the technique to be pushed to the 20 keV energy.

A.3 General layout

Inelastic X-ray scattering (IXS) and X-ray emission (XES) spectrometers can provide optimal performances on undulator beamlines capable of providing an intense X-ray beam fixed in position and characterized by a bandwidth and a spot size which can be chosen as freely as possible.

The optics dedicated to focusing the beam consist of four mirrors: i) a vertically collimating mirror placed in the white beam; ii) a pre-focusing mirror that produces a secondary source; iii-iv) a double mirror setup in KB geometry to focus the beam to the sample stage. The layout proposed here was to design the focusing optics so that not less than 200 mm of free space is left around the sample position, i.e. comparable to the free space left by the spectrometer design. It also allows in addition to easily reach a spot size of $\sim 8 \times 8$ μm^2 (V×H) FWHM by simply slitting down the secondary source horizontally to half of its size (at the expense of 50% loss in intensity).

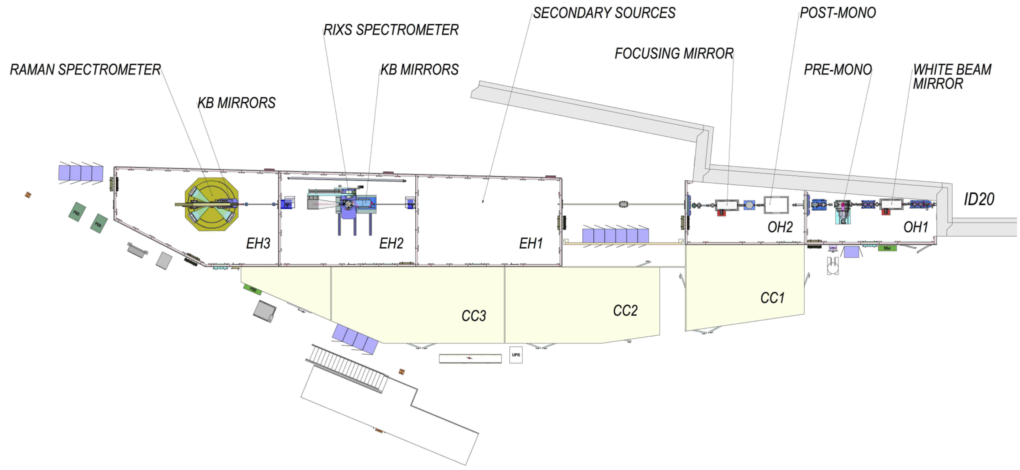

Figure A.1: UPBL06 all beamline layout (top view).

The optics dedicated to selecting the bandwidth (a fixed-exit double crystal pre-monochromator, DCM, and a four-crystal post-monochromator, 4CM) are installed after the beam has been collimated in order that the vertical divergence plays as small a role as possible in the monochromatization stage.

Finally, in order to make the operation of the beamline as efficient as possible, two experimental stations (UPBL06-A and UPBL06-B) are foreseen, optimized for non-resonant/resonant emission experiments respectively, with each station hosting one spectrometer.

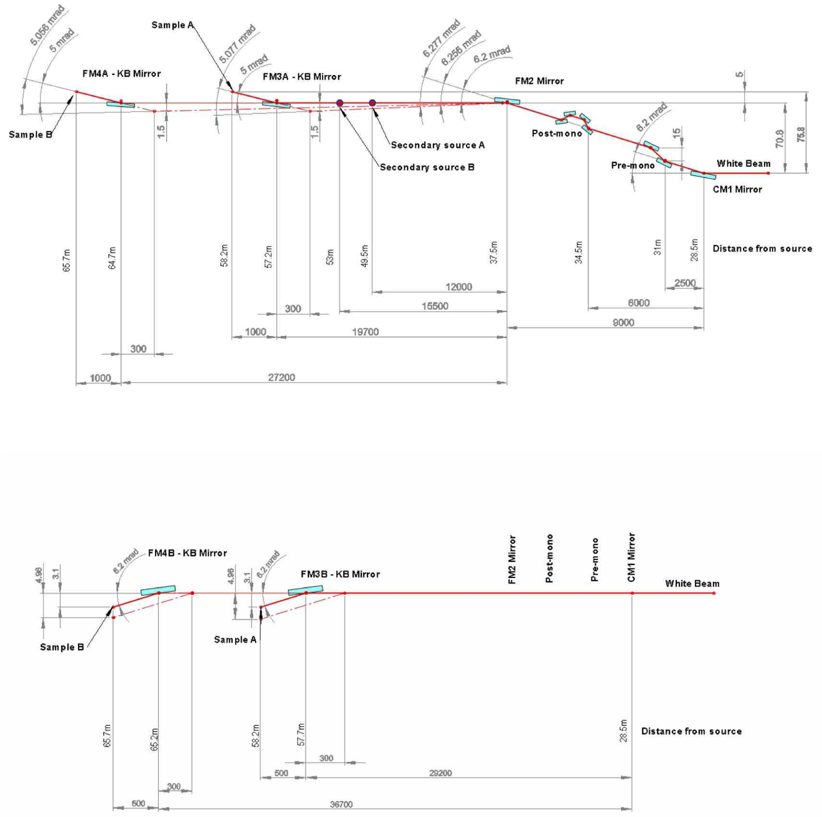

Figure A.2: UPBL06 optical layout principle. The vertical configuration is presented at the top of the figure, the horizontal one at the bottom. Distances from the source are in meters.

A.4 Design of end station

In this section I will ofcus on the activity I have been involved in. Mainly, I participated to the realization of spherical crystal analyzers for inelastic X-ray scattering experiments (IXS) using a new manufacturing technique. In the following paragraphs I will introduce the crystal analyzers which are the key elements in IXS, as most of the spectrometers are based today on crystal analyzers operating in Rowland-circle geometry, which allows for a simultaneous focusing and energy analysis of the X-rays emitted by a point source.

The main motivation for the UPBL06 project is to build a beamline optimized for electronic-excitation spectroscopy. The new beamline will feature two separate spectrometers optimized for different scientific tasks:

1. High-resolution IXS spectrometer in Experimental Hutch 2 (EH2)

2. Large collection angle IXS spectrometer (in EH3)

Both spectrometers are multiple-analyzer-crystal instruments and are based on the symmetric Rowland-circle geometry [70] with spherically bent analyzer crystals. The spectrometers are optimized for energy resolutions in the 5-200 meV range (EH2) and in the 300-1000 eV range (EH3), and will be operated in the 5-20 keV energy range.

This chapter is dedicated to describing the expected optic performance of these spectrometers.

A.4.1 EH2: high-resolution spectrometer

EH2 is dedicated to the housing of the high-resolution spectrometer. This spectrometer is specialized in energy resolutions $<$100 meV for non-resonant IXS experiments and of 100-200 meV for resonant IXS ones. The accessible energy range covers the typical K edges of the 3d transition metals, L edges of lanthanides and many of the corresponding emission lines.

The spectrometer for EH2 is shown in Figure A.3 and consists of a 2θ arm which houses several analyzer crystals. The spectrometer is mounted on a marble block which lies on rails (perpendicular to the beam) making it possible to move the KB+spectrometer assembly in and out of beam. The spectrometer arm is a 2-circle goniometer with two external rotations, one for θZ and one for θY. The arm itself is 2 m long and can accommodate analyzers at distances of either 1 m or 2 m from the sample position. The analyzer housing is an aluminum frame containing individual goniometers for up to 5 analyzer crystals. The analyzers are curved or diced wafers of Si or Ge, 100 mm in diameter, that are fixed to concave glass forms which are 15 mm thick.

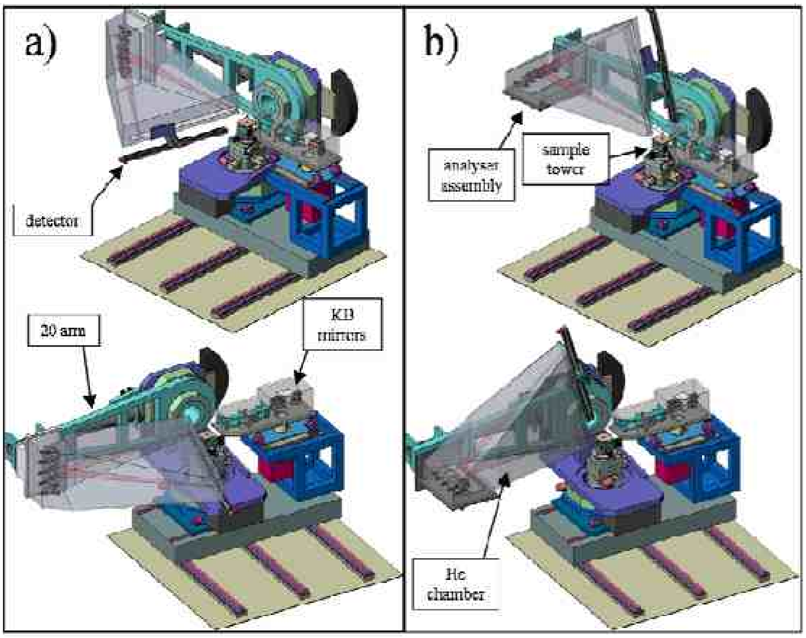

Figure A.3: Different spectrometer configurations for RIXS experiments. (a) Spectrometer ready for vertical- q operation; (b) Ready for horizontal-q operation. In this picture the analyzers are located at distance R=2 m from the sample.

The analyzers monochromatise the scattered radiation with a Bragg angle in the 70-90° range. At the same time, the analyzers focus the collected radiation on a detector which is mounted on its own positioning system. The purpose of the detector motorization is to keep the analyzers on the Rowland circle when the analyzer angles are tuned during an E_2 scan.

The detector is an ESRF-developed 5 x Medipix2 chip.

Johann-geometry aberration

The ideal spectrometer conceived by DuMond and Kirkpatrick [71] requires two conditions for the reflecting lattice planes: they should 1) be curved so that their normals converge to a point (the center of curvature) located on the Rowland circle; and 2) that the crystal surface should coincide with the Rowland circle. However, the second condition is not as compelling as the first and within a reasonable approximation it can be relaxed, leading to the so-called Johann geometry where the reflecting crystal planes are parallel to the crystal surface, both being curved into a cylindrical shape with a curvature radius twice that of the Rowland circle. This approximation is widely used today, but in certain cases causes a non-negligible effect on the resolution function for RIXS experiments. The angle of incidence of the rays arriving at the crystal is smaller for the ray i arriving at the centre of the crystal (the nominal angle) than for a ray j that arrives at another part of the crystal. If ϕ is the largest angular difference in the dispersing direction between the rays i and j, then the Johann aberration can be estimated as:

$$\Delta\theta_j \approx \frac{1}{2}\cot\left(\theta_B + \alpha\right)\varphi^2. \tag{A.1}$$

An example of the dispersion of the photon energies reflected by a Si (551) diced analyzer crystal in conditions for a RIXS experiment at the Ni K-edge (diameter 100 mm, R=1000 mm, θ_B = 78.05° , E_1=E_2=8.332 keV) is reported in Figure A.4. There it is shown that an efficient way of reducing the Johann aberration in the case of round analyzer wafers is to mask the edges.

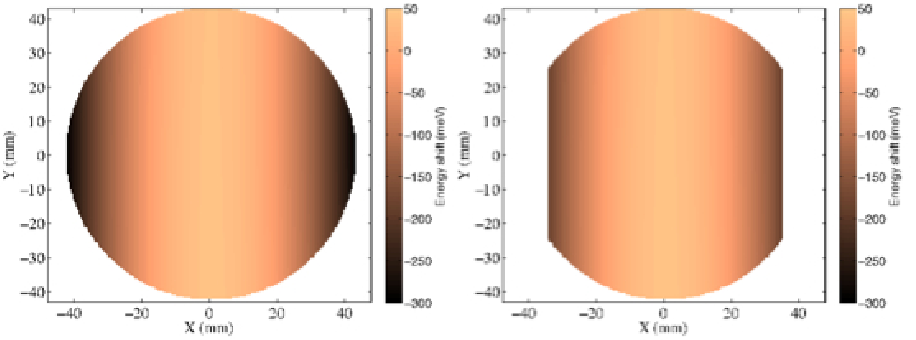

Figure A.4: *Left*: Distribution of photon energy shifts on a Si (551) analyzer crystal with nominal Bragg angle θ_B =78.05°. *Right*: An efficient way of reducing the spread is to use an active analyzer area shown on right.

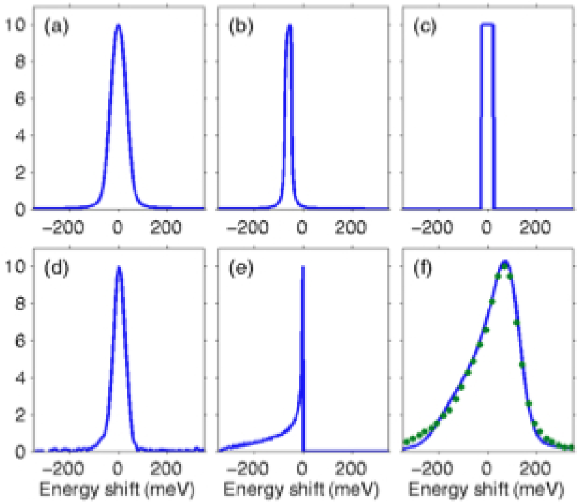

Figure A.5: Contributions to the energy resolution in a RIXS experiment at Ni K-edge. (a) Incident bandwidth from a Si (111)+Si (444) monochromator ensemble; (b) Darwin width of the Si (551) analyzer (note the refraction correction leading to a shifted profile); (c) contribution from the finite pixel size of the Medipix2 detector; (d) from the incident-beam focal spot size on the sample; (e) from the Johann-geometry aberration; (f) total (theory: line and experiment: dots).

A.4.2 EH3: large solid angle spectrometer

EH3 is dedicated to the spectrometer optimized for non-resonant IXS experiments with an energy resolution of $\sim$ 0.3-1 eV, and covers a large solid angle for the collection of the scattered radiation. This spectrometer is specialized for X-ray Raman spectroscopy measurements from a variety of samples. The aim of its design is to concentrate a large number of analyzer-crystals in positions corresponding to a well defined momentum transfer q.

The final arrangement of the units, and the number of analyzers (eight to twelve) in each unit will be finalized at the end of the detailed design study of the spectrometer and will depend on the progress that is made in the construction of Ge analyzers and on the availability of CdTe detectors. In this spectrometer the angles of the analyzers will not be scanned during the experiment (after they have been aligned) and the detector will be at a fixed position (of course after it has been aligned as well). The design shown in Figure A.6 is based on six units housing 12 analyzers each.

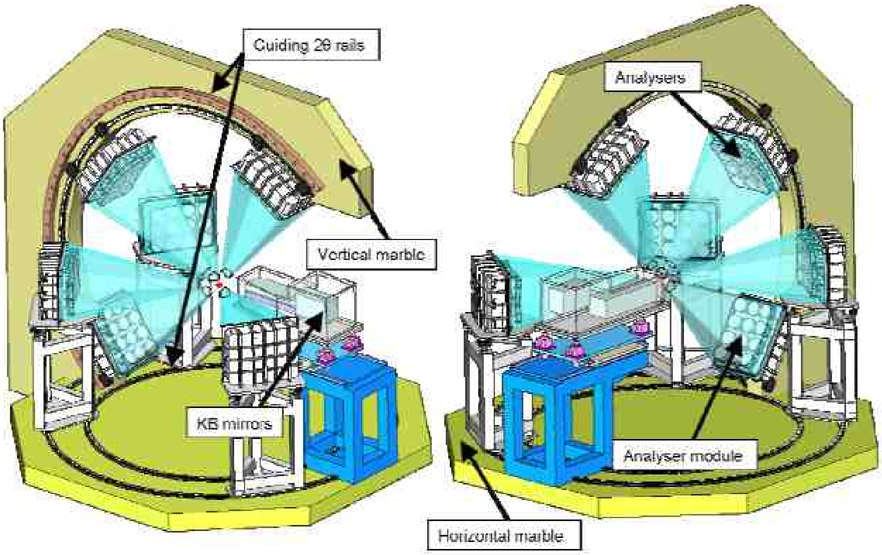

Figure A.6: Overall view of the EH3 spectrometer with six modules carrying 12 analyzer crystals each.

Figure A.7: Picture of the unit for the housing of 12 analyzer crystals.

Figure A.8 shows the pre-design of a module housing 8 analyzer crystals in two rows each carrying four analyzers. As shown in Figure A.8, the radiation scattered by the sample enters the module through an entrance window (kapton) and is monochromatised by the analyzers. The chamber wall material is composite carbon fiber. The chamber is evacuated to avoid absorption and scattering by air in the sample-analyzer-detector flight path. The analyzers simultaneously focus the collected radiation on a detector which is placed near the entrance window. Each module will carry one unit of the 256x256 pixel Medipix2 CdTe detector.

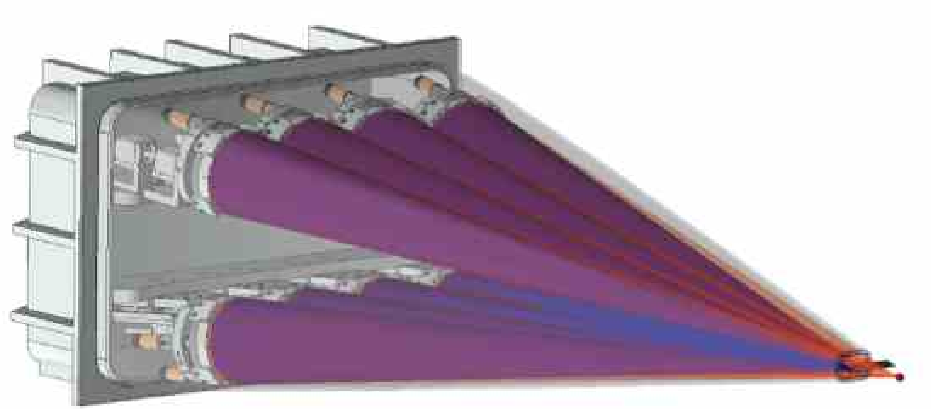

Figure A.8: Design of an analyzer-crystal module carrying 8 analyzer crystals.

Off Rowland contribution

Since 1) this spectrometer will be operated with Bragg angles close to 90°, 2) at the same time it will be necessary to reserve a certain amount of space for sample environment and 3) it is also necessary to tune the analyzer-detector distance to conditions where the foci of the analyzers are fully captured by the detector, we will place the detector in- or outside the Rowland circle by a distance of $2z$ and move the analyzers correspondingly by a distance z. This causes the Bragg angles to vary across the analyzer to generate a dispersion:

$$\frac{\Delta E}{E} = \frac{zD}{R^2} \cot \theta_B. \tag{A.2}$$

Here D is the diameter of the analyzer (100 mm). This dispersion is called the off-Rowland contribution to the resolution function and it may become important for the spectrometer operation conditions. To minimize the off-Rowland contribution, the relative offset z/R should be kept as small as possible, the individual-analyzer opening D/R should be kept small and θ_B as close to 90° as possible.

A.5 Analyzer crystals

All of the IXS experiments foreseen on the beamline are based on crystal-analyzer Rowland-circle spectrometers. The analyzer crystal is a curved Bragg monochromator which is placed downstream of the sample. A typically used analyzer crystal is based on the Johann geometry, i.e. in the dispersive plane it has a circular shape with a radius equal to the Rowland circle diameter R.

A.5.1 Bent-wafer analyzers

Bent analyzers (Fig. A.9) are based on large (4" diameter) monolithic wafers which are bonded on a curved glass substrate. While taking the form of the substrate, the bending causes elastic deformations. This modifies the reflectivity curve of such an analyzer and in general the bandwidth becomes larger than the Darwin width. An approximate dependence of the reflected bandwidth on the curvature radius and Bragg angle is given by:

$$\frac{\Delta E}{E} \approx \frac{t}{R} \left|\cot^2\theta_B - n\nu\right| . \tag{A.3}$$

Here t is the absorption length within the crystal and ν is the Poisson ratio of the crystal material. The parameter n = 1 for cylindrical or n = 2 for spherical bending.

To minimize this bandwidth, it is possible to minimize the probing depth of the X-rays (using high-Z materials such as Germanium or choosing the lowest X-ray energies compatible with the experiment), to increase the bending radius R, or to choose a Bragg angle close to the condition $\cot^2\theta = \mathrm{n}\nu$. The current choice of B materials of Si and Ge together with bending radii R=1-2 m corresponds to a reasonable compromise between available technologies, collected solid angles, and experimental bandwidths.

A.5.2 Diced analyzers

To avoid the elastic-deformation broadening of the analyzer reflectivity, analyzer crystals consisting of a collection of single crystal cubes (size 0.7 mm × 0.7 mm, thickness ∼ 1-2 mm) fixed on a spherical substrate are used (Fig.

Figure A.9: An anodic bonded elastically bent analyzer.

A.10). The shape of the crystal in this case follows the ideal curved shape only approximatively. The Bragg angle varies on the surface of a crystal cube of size c creating a dispersion given by:

$$\frac{\Delta E}{E} = \frac{c}{R} \cot \theta_B. \tag{A.4}$$

The cube-size contribution has this far been considered to be inevitable. The only ways of minimizing the effect have been to reduce the cube size c, to increase the Rowland circle diameter R and to increase the Bragg angle to as close to 90° as possible. Reducing the cube size faces mechanical limitations, and a part of the crystal is inevitably lost because of sawing and etching. Thus the smaller the cube size, the lower the efficiency of the analyzer. Increasing the Rowland circle diameter reduces the solid angle over which the photons are collected, the observed intensity decreasing as $1/\mathrm{R}^2$.

A method (Fig. A.11) has been developed to eliminate the cube-size error by using a two-dimensional position-sensitive pixel detector (PSD) and performing a dispersion-compensation correction to the data recorded by individual pixels [72]. The method was applied in an experiment with an incident photon energy of 9.9 keV, a diced Si (555) crystal in a 1 m Rowland geometry [73] and a Medipix2 detector. The 190 meV cube-size contribution to the resolution function was eliminated and a final resolution of 23 meV was achieved.

Diced analyzers are used in particular when the broadening of the band-

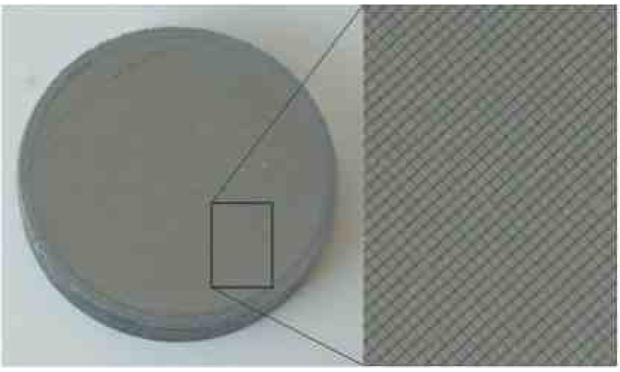

Figure A.10: Diced crystal analyzer for high-resolution applications, thickness 2 mm and a cube size 0.7 mm.

width due to bending is too large. Their energy resolution is very high, down to 10 meV. The main disadvantage of diced analyzers is that they do not offer point-to-point focusing. Also, for medium energy-resolution applications the bandwidth of a diced crystal can be too narrow and a larger intensity is often welcome, which is achieved using bent analysers.

Currently most of the analyzers are made out of Silicon due to the good availability of high-quality material and to its properties under bending. Ge is of interest for two main reasons: 1) it is a necessary choice in several relevant energy ranges; 2) due to its higher Z, the effect of the curvature on its bandwidth is smaller. The last point makes Ge especially interesting since it is expected to retain its narrow bandwidth up to relatively high energies, whereas bent Si crystals start to have bandwidths far beyond what is acceptable for typical IXS experiments.

A.6 Realization of spherical crystal analyzers

Throughout my stay at the ESRF I took part in the construction of spherical elastically bent crystal analyzers for the IXS experiments. In the following section I will present the technique adopted to produce silicon analysers for electronic excitations [74], thanks to the anodic bonding procedure.

The energy resolution required for IXS experiments is usually not very high (ΔE=0.2÷1.5 eV). For this reason the spherical analyzers employed in

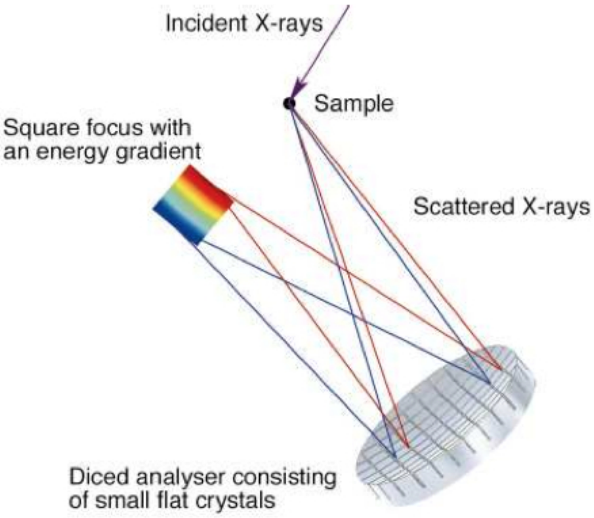

Figure A.11: The working principle of the removing cube-size error method.

such experiments are usually elastically bent and not diced. In order to produce an elastically bent analyzer, the most common procedure is to glue a thin silicon wafer onto a spherical substrate, with the difficulty of distributing the glue uniformly. Given that dust particles may negatively affect the processes, all the operations have been done in a clean room environment.

To avoid the problems associated with the glue uniformity and presence of dust particles, has been developed by the group led by R. Verbeni the anodic bonding technique.

Basically, the anodic bonding is a is a process which allows for the bonding of silicon to glass well below the softening point of the glass. The bond is typically performed between a sodium-bearing glass (borosilicate glasses) wafer and a silicon wafer. The bonding procedure is fairly simple. Once the surfaces are perfectly clean and the wafer is in contact with the substrate with the help of a small applied pressure, the wafer plus the substrate are heated up to a temperature in the range of 200÷450 °C. In these conditions the bond is realized by the application of an external electric field with a voltage of the order of 1500÷4000 V. The glass substrate is the cathode and the silicon wafer is the anode. Under such a high field and elevated temperature, the mobile NaC ions in the glass migrate away from the bonded interface, leaving behind fixed charges in the glass that create a high electric field across the bond interface with image charges in the silicon. The variables that control the process are temperature, time and voltage.

The anodic bonding is also an irreversible process in the sense that it is impossible to separate the wafer and substrate by applying an inverse electric field at high temperature.

The following procedure has been adopted for the realization of bent analyzers.

The analyzers are obtained from silicon wafers of 100 mm diameter (Fig. A.12) and 500 or 300±20 mm thickness, which are cut from an ingot produced by the float zone technique. The IXS spectrometers for electronic excitations studies at the ESRF require a curvature radius of 1.0 or 2.0 m.

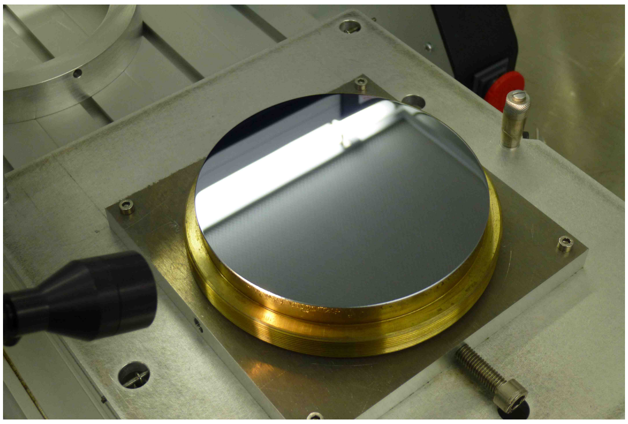

Figure A.12: Double-side polished silicon wafer (10 cm diameter) in the clean room before the cleaning.

The wafers characterization is accomplished using a precise interferometer (Fig. A.14) to measure the figure error and the focal distance. A selection of the crystals is done by studying their shape and subsequently discarding all the wafers with an irregular dislocations. Some examples are shown in Figures A.13.

After the selection, the silicon wafers and the spherical Pyrex substrates are cleaned in a clean room with acetone and ethanol (Fig. A.15). To remove the residual organic compounds we use the ultra-violet ozone cleaning procedure.

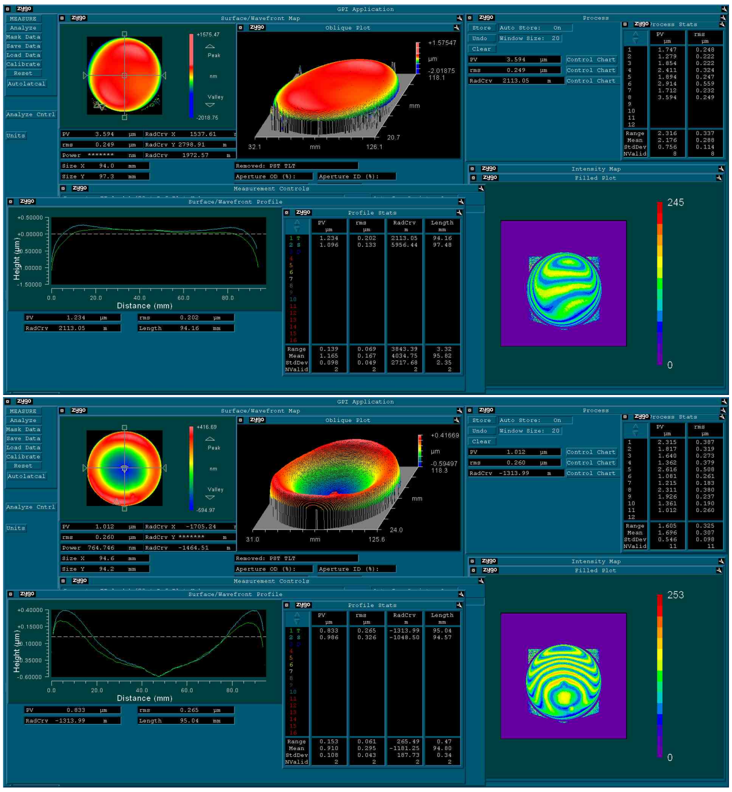

PV 3.594 µm
rms 0.249 µm
Power ******* nm
RadCrv X 1537.61
RadCrv Y 2798.91 m
RadCrv 1972.57 m
Size X 94.0 mm
Size Y 97.3 mm
Removed: PST TLT
Aperture OD (%):
Aperture ID (%):

Auto Store: On
Window Size: 20
PV 3.594 µm
rms 0.249 µm
RadCrv 2113.05 m

	PV µm	rms µm
1	1.747	0.248
2	1.279	0.222
3	1.854	0.222
4	2.411	0.324
5	1.894	0.247
6	2.914	0.559
7	1.712	0.232
8	3.594	0.249
9		
10		
11		
12		
Range	2.316	0.337
Mean	2.176	0.288
StdDev	0.756	0.114
NValid	8	8

	PV µm	rms µm	RadCrv m	Length mm
1 T	1.234	0.202	2113.05	94.16
2 S	1.096	0.133	5956.44	97.48
3 D				
4				
5				
6				
7				
8				
9				
10				
11				
12				
13				
14				
15				
16				
Range	0.139	0.069	3843.39	3.32
Mean	1.165	0.167	4034.75	95.82
StdDev	0.098	0.049	2717.68	2.35
NValid	2	2	2	2

PV 1.234 µm
rms 0.202 µm
RadCrv 2113.05 m
Length 94.16 mm

PV 1.012 µm
rms 0.260 µm
Power 764.746 nm
RadCrv X -1705.24
RadCrv Y ******* m
RadCrv -1464.51 m
Size X 94.6 mm
Size Y 94.2 mm
Removed: PST TLT
Aperture OD (%):
Aperture ID (%):

Auto Store: On
Window Size: 20
PV 1.012 µm
rms 0.260 µm
RadCrv -1313.99 m

	PV µm	rms µm
1	2.315	0.387
2	1.817	0.319
3	1.640	0.273
4	1.362	0.379
5	2.616	0.508
6	1.081	0.261
7	1.215	0.183
8	2.311	0.380
9	1.926	0.237
10	1.361	0.190
11	1.012	0.260
12		
Range	1.605	0.325
Mean	1.696	0.307
StdDev	0.546	0.098
NValid	11	11

	PV µm	rms µm	RadCrv m	Length mm
1 T	0.833	0.265	-1313.99	95.04
2 S	0.986	0.326	-1048.50	94.57
3 D				
4				
5				
6				
7				
8				
9				
10				
11				
12				
13				
14				
15				
16				
Range	0.153	0.061	265.49	0.47
Mean	0.910	0.295	-1181.25	94.80
StdDev	0.108	0.043	187.73	0.34
NValid	2	2	2	2

PV 0.833 µm
rms 0.265 µm
RadCrv -1313.99 m
Length 95.04 mm

Figure A.13: *Top*: Silicon wafer with a flat profile. *Bottom*: Discarded wafer with irregular shape.

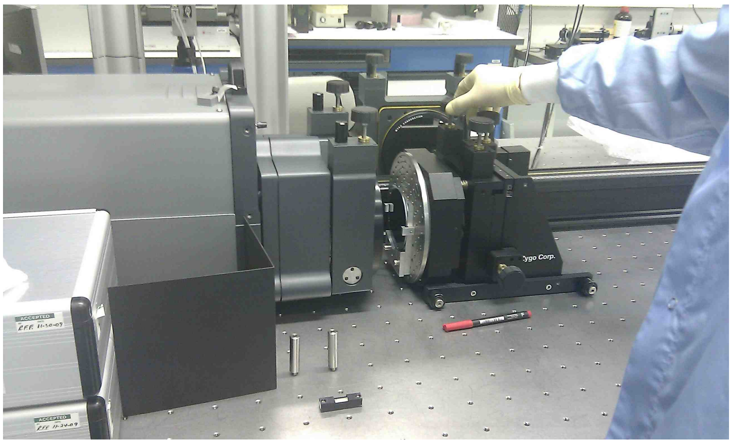

Figure A.14: Silicon wafer during the interferometric profile measurements.

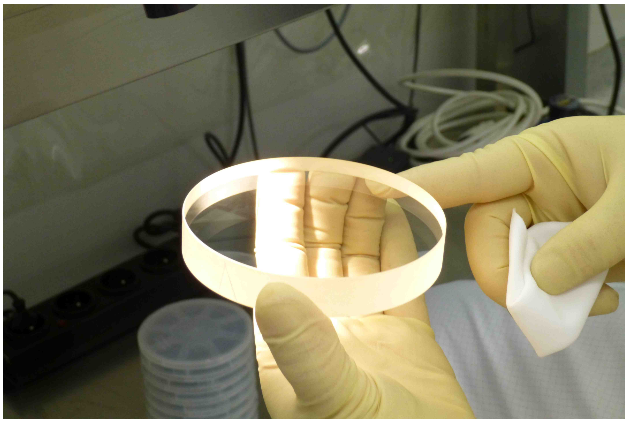

Figure A.15: The spherical Pyrex during the cleaning.

Once the surfaces are clean the silicon wafer is put in contact with the concave blank. This operation should be done as fast as possible in order to minimize the presence of dust particles. On top of the silicon wafer we put a thin film of conducting kapton of the same size and the convex glass blank (Fig. A.16).

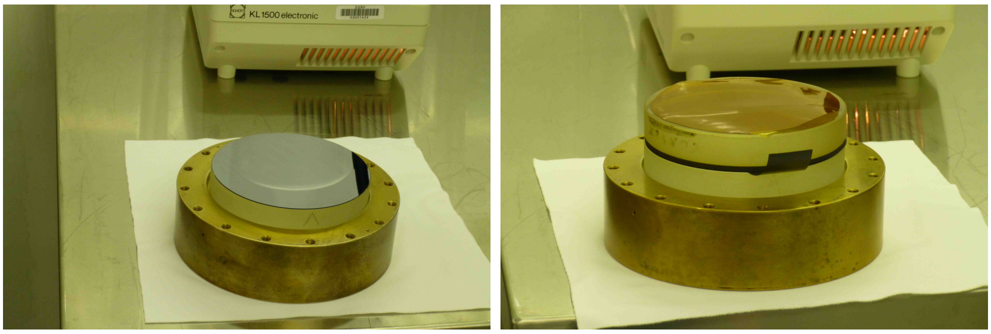

Figure A.16: *Left*: The silicon wafer on the glass concave substrate. *Right*: The ensemble once the convex glass is placed on. The kapton film (black) is also visible.

Afterwards the whole ensemble is installed in the pressing tool (Fig. A.17) and heated up to 200÷350 °C for 2h. A positive high voltage (1500÷4000 V) is gradually applied to the conducting kapton and maintained for 2-3 h until the produced current decreases to zero (Fig. A.18). A zero current means that all the free positive ions have moved away from the bonding surface.

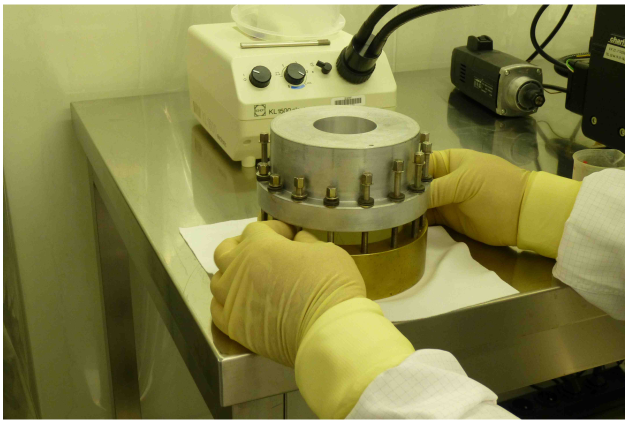

Figure A.17: The pressing tool.

In typical working conditions (T=335 °C and V=1800 V) the current rapidly increases to 2.9÷3.1 mA and then decreases exponentially to zero within a few hours.

Once the analyser is ready, the X-ray characterization is done often in backscattering configuration in order to minimize the various geometrical contributions to the energy resolution such as the source size, the Johann error contribution and the out-of-Rowland contribution, that are all proportional to cot θ_B or to $\cot^2\theta_B$. The results are very good, and the resolution achieved by analysers realized with the anodic bonding procedure is very high (ΔE=1÷10 meV).

The above described manufacturing technique is very satisfactory and it does not need major modifications. The analyzers have an energy resolution very close to the expected one over basically the whole crystal surface and they have as well a very good focal spot.

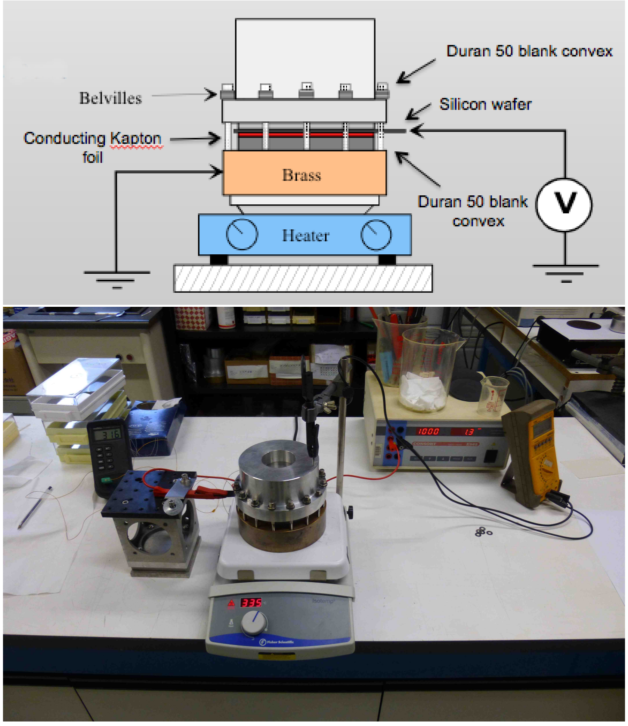

Figure A.18: *Top*: Schematic view of the experimental apparatus for the anodic bonding procedure. The voltage is applied on a thin conducting kapton foil situated between the silicon wafer and the Pyrex convex blank. *Bottom*: A picture of the apparatus during the bonding.

IRAP Erasmus Mundus PhD Activity

Schools, Conferences and Collaborations

- IRAP Ph.D. Erasmus Mudus School, September 6-30, 2010, Nice (France);
- 25th TEXAS Symposium on Relativistic Astrophysics, December 6-10, 2010, Heidelberg (Germany) ;
- IRAP Ph.D. Erasmus Mundus Workshop, March 21-26, 2011, Pescara (Italy);
- IRAP Ph.D. Erasmus Mundus Workshop, April 3-8, 2011, Les Houches (France);
- IRAP Ph.D. Erasmus Mundus School, May 23th - June 6th, 2011, Nice (France);
- SPIE Optics + Photonics Conference, August 21-25, 2011, San Diego (USA);
- IRAP Ph.D. Erasmus Mundus School, September 5-13, 2011, Nice (France);
- Second Ferrara Workshop on X-Ray Astrophysics up to 511 KeV, September 14-16, 2011, Ferrara (Italy);
- Galileo-Xu Guanqui Meeting, October 11-15, 2011, Beijing (China);

- IRAP Ph.D. Erasmus Mundus School, June 4-15, 2011, Nice (France);
- SPIE Astronomical Telescopes + Instrumentation 2012 Conference, July 1-7, 2012, Amsterdam (Netherlands);
- The Thirteenth Marcel Grossmann Meeting - MG13, July 1-7, 2012, Stockholm (Sweden);
- IRAP Ph.D. Erasmus Mundus School, September 3-22, 2012, Nice (France);
- X-ray Astronomy: towards the next 50 years!, October 1-5, 2012, Milan (Italy);
- Training/research period (mobility) requested by the Ph.D. program IRAP at the European Synchrotron Radiation Facility (ESRF), October 15th - December 15th, 2012, Grenoble (France);
- Research period (mobility) requested by the Ph.D. program IRAP at the "University of Stockholm", April 15th - July 15th, 2013, Stockholm (Sweden);
- The first URCA meeting on Relativistic Astrophysics ICRANet Rio, June 24-29, 2013, Rio de Janeiro, Brazil;
- SPIE Optics + Photonics Conference, August 25-29, 2013, San Diego (USA);

Courses, Activity and Certificates

- First certificate in English (Cambridge ESOL) Grade B;
- "Temporal data analysis: Theory and Procedures", Prof. Mauro Orlandini (40 hours course);
- "X-/Gamma-rays Observations", Prof. Filippo Frontera (40 hours course);

- "Spectrum energy correlations in GRBs", Prof. Lorenzo Amati (40 hours course);
- "Detectors for High Energy Astrophysics", Prof. Ezio Caroli (20 hours course);
- "Entry-level LabVIEW course (CLAD)", Prof. Roberto Foddis (25 hours course).

....

Bibliography

[1] F. Frontera, E. Costa, D. Dal Fiume, M. Feroci, L. Nicastro, M. Orlandini, E. Palazzi, and G. Zavattini. The High Energy Instrument PDS on-Board the BeppoSAX X-Ray Astronomy Satellite, *Astronomy & Astrophysics Suppl. Series, 122: 357-369* (1997).

[2] P. Ubertini, F. Lebrun, G. Di Cocco, A. Bazzano, A. J. Bird, K. Broenstad, A. Goldwurm, G. La Rosa. IBIS: The Imager on-board INTEGRAL, *Astronomy and Astrophysics, v.411, p.L131-L139* (2003).

[3] K. D. Joensen, F. E. Christensen, H. W. Schnopper, P. Gorenstein, J. Susini, P. Hoghoj, R. Hustache, J. L. Wood, and K. Parker. Medium-Sized Grazing Incidence High-Energy X-Ray Telescopes Employing Continuously Graded Multilayers, *Proc. SPIE, 1736: 239-248* (1993).

[4] Fiona A. Harrison, William W. Craig, Finn E. Christensen, Charles J. Hailey, William W. Zhang. The Nuclear Spectroscopic Telescope Array (NUSTAR) High Energy X-ray Mission, *ApJ* ***770*** *103* (2013).

[5] F. Fiore, G. C. Perola, G. Pareschi, O. Citterio, A. Anselmi, and A. Comastri. HEXIT-SAT: A Mission Concept for X-Ray Grazing Incidence Telescopes from 0.5 to 70 keV, *Proc. SPIE, 5488: 933-943* (2004).

[6] Camattari R., Bellucci V., Guidi V. and Neri I. Quasi-mosaic crystals for high-resolution focusing of hard x-rays through a Laue lens, *Proc. of SPIE Vol. 8147, 81471 G* (2011).

[7] F. Frontera, P. De Chiara, M. Gambaccini, and G. Pasqualini G. Landini. Hard X-ray imaging via crystal diffraction: first results of reflectivity measurements, *Proc. SPIE, 1549: 113-119* (1991).

[8] Exploring the X-ray Universe by Frederick D. Seward and Philip A. Charles, *Cambridge University Press* (2010).

[9] Giacconi, R. and Gursky, H. and Paolini, F. R. and Rossi, B. Evidence for x Rays From Sources Outside the Solar System, *Physical Review Letters, 439-443* (1962).

[10] Giacconi, R. and Gursky, H. and Kellogg, E. and Schreier E. Discovery of Periodic X-Ray Pulsations in Centaurus X-3 from UHURU, *Astrophysical Journal, vol. 167, p.L67* (1971).

[11] Voges, W., Aschenbach, B., Boller, T., Brauninger, H., Briel, U., Burkert, W. The ROSAT all-sky survey bright source catalogue, *Astronomy and Astrophysics 349, 389-405* (1999).

[12] Forman, W., Jones, C., Cominsky, L., Julien, P., Murray, S., Peters, G. The fourth Uhuru catalog of X-ray sources, *Astrophysical Journal, Suppl. Ser., Vol. 38, p. 357 - 412* (1978).

[13] A.M. Levine, et al. The HEAO 1 Catalog of High-Energy X-Ray Sources, *Astrophysical Journal Supplement Series vol. 54, p. 581-617* (1984).

[14] Giacconi, R., Branduardi, G., Briel, U., Epstein, A., Fabricant, D., Feigelson, E. The Einstein /HEAO 2/ X-ray Observatory, *Astrophysical Journal, Part 1, vol. 230, p. 540-550* (1979).

[15] Aschenbach, B. First Results from the X-Ray Astronomy Mission ROSAT, *Reviews in Modern Astronomy, v. 4, p. 173-187.* (1991).

[16] Gruber, D. E., Blanco, P. R., Heindl, W. A., Pelling, M. R., Rothschild, R. E. The high energy X-ray timing experiment on XTE,*Astronomy and Astrophysics Supplement, v.120, p.641-644* (1996).

[17] Boella, G. and Butler, R. C. and Perola, G. C. and Piro, L. and Scarsi, L. and Bleeker. BeppoSAX, the wide band mission for X-ray astronomy, *A&A Supplement series, Vol. 122, 299-307* (1997).

[18] E. Costa, F. Frontera, J. Heise, M. Feroci, J. in 't Zand, F. Fiore. Discovery of an X-ray afterglow associated with the -ray burst of 28 February 1997, *Nature 387, 783-785* (1997).

[19] Weisskopf, M. C. and Brinkman, B. and Canizares. An Overview of the Performance and Scientific Results from the Chandra X-Ray Observatory (CXO), *he Publications of the Astronomical Society of the Pacific, Volume 114, Issue 791, pp. 1-24* (2002).

[20] F. Jansen, D. Lumb, B. Altieri, J. Clavel, et al. XMM-Newton observatory. I. The spacecraft and operations, *Astronomy and Astrophysics, v.365, p.L1-L6* (2001).

[21] N. Gehrels et al. The Swift Gamma-Ray Burst Mission, *ApJ **611** 1005* (2004).

[22] Naya, J., von Ballmoos, P., Smither, R.K., Faiz, M., Fernandez, P., Graber, T., Albernhe, F., Vedrenne, G. *Nuclear Instr. Meth. Phys. Res. Sect. A 373, 159* (1996).

[23] Peter von Ballmoos, Hubert Halloin, Jean Evrard, Gerry Skinner, Nikolai Abrosimov. CLAIRE: First light for a gamma-ray lens, *Experimental Astronomy, Volume 20, Issue 1-3, pp 253-267* (2005).

[24] H.Halloin, P.von Ballmoos, J.Evrard, et al. CLAIRE gamma-ray lens: flight and long distance test results, *Proceedings of the SPIE, Volume 5168, pp. 471-48* (2004).

[25] Glenn F. Knoll. Radiation detection and measurement 3rd ed, *John Wiley & Sons Inc, New York* (2000).

[26] U. Fano. On the Theory of Ionization Yield of Radiation in Different Substances, *Physics Review 70, 44* (1946).

[27] A. F. Muggleton. Semiconductor X-Ray Spectrometers, *Nuclear Instruments and Methods 101, 113* (1972).

[28] D. A. Gedcke. How Histogramming and Counting Statistics Affect Peak Position Precision, *ORTEC Application Note AN58, available at http://www.ortec-online.com/Library/index.aspx?tab=1.*

[29] Ron Jenkins, R. W. Gould and Dale Gedcke. Quantitative X-Ray Spectrometry, *Marcel Dekker, Inc., New York* (1981).

[30] Bradt, H., Garmire, G, Gursky H. The Modulation Collimator in X-ray Astronomy *Space Science Reviews, Volume 8, Issue 4, pp.471-506* (1968).

[31] Amplifier Introduction - ORTEC, *URL: http://www.ortec-online.com/.*

[32] P.W. Nicholson, Nuclear Electronics, *John Wiley & Sons, London* (1973).

[33] E. Virgilli, F. Frontera, V. Valsan, V. Liccardo. Laue lenses for hard X-/soft γ rays: new prototype results, *Proc. of SPIE Vol. 8147* (2011).

[34] F. Frontera, G. Loffredo, A. Pisa, L. Milani, F. Nobili, N. Auricchio, V. Carassiti. Development status of a Laue lens project for gamma-ray astronomy, *Proc. of SPIE Vol. 6688* (2007).

[35] F. Ferrari, F. Frontera, G. Loffredo, E. Virgilli. New results on focusing of gamma-rays with Laue lenses, *SPIE Proceedings, vol.7437-19* 2009.

[36] G. Loffredo F. Frontera, D. Pellicciotta, A. Pisa, V. Carassiti. The X-ray facility of the physics department of the Ferrara University, *Experimental Astronomy, Volume 18, Issue 1-3, pp 1-11* (2004).

[37] W. H. Zachariasen, Theory of X-ray Diffraction in Crystals, *Wiley & Sons, London* (1945).

[38] F. Frontera, G. Loffredo, A. Pisa, F. Nobili, V. Carassiti. Focusing of gamma-rays with Laue lenses: first results, *Proc.SPIE vol.7011* (2008).

[39] J. Knodlseder, P. Jean, V. Lonjou, G. Weidenspointner. The all-sky distribution of 511 keV electron-positron annihilation emission, *Astronomy and Astrophysics, Volume 441, Issue 2, pp.513-532* (2005).

[40] J. Knodlseder, P. von Ballmoos, F. Frontera, A. Bazzano, F. Christensen, M. Hernanz, and C. Wunderer. Gri: focusing on the evolving violent universe. In *Optics for EUV, X-Ray, and Gamma-Ray Astronomy III. Edited by O'Dell, Stephen L.; Pareschi, Giovanni. Proc of SPIE, Vol. 6688* (2007).

[41] J. Vink, J. Martin Laming, Jelle S. Kaastra. Detection of the 67.9 AND 78.4 keV lines associated with the 44 radioactive decay of Ti in Cassiopea A. *The Astrophysical Journal, 560:L79-L82* (2001).

[42] F. Frontera, M. Orlandini, R. Landi, A. Comastri. The cosmic X-ray background and the population of the most heavily obscured AGNs, *The Astrophysical Journal, 666:86-95* (2007).

[43] F. Frontera and Peter von Ballmoos. Laue gamma-ray lenses: status and prospects, *X-Ray Optics and Instrumentation Volume 2010* (2010).

[44] Lund N., A study of focusing telescopes for soft gamma rays, *Experimental Astronomy 2, 259-273* (1992).

[45] Cullity B. D., X-ray diffraction, *Addison-Wesley Publishing Company, Inc.* (1956).

[46] Authier A., Dynamical Theory of X-ray Diffraction, *Oxford University Press, Oxford* (2001).

[47] Hubert Halloin, Pierre Bastie, Laue diffraction lenses for astrophysics: Theoretical concepts, *Experimental Astronomy, Volume 20, Issue 1-3, pp 151-170* (2005).

[48] Barriere, N., Rousselle, J., von Ballmoos, P., Abrosimov, N. V., Courtois, P., Bastie, P., Camus, T., Jentschel, M., Kurlov, V. N., Natalucci, L., Roudil, G., Frisch Brejnholt, N., and Serre, D., Experimental and theoretical study of diffraction properties of various crystals for the realization of a soft gamma-ray Laue lens, *Journal of Applied Crystallography 42, 834-845* (2009).

[49] Malgrange, V., X-ray Propagation in Distorted Crystals: From Dynamical to Kinematical Theory, *Crystals research and technology 37, 654-662* (2002).

[50] N. Barriere, P. von Ballmoos, P. Bastie, P. Courtois, N. V. Abrosimov, R&D progress on second-generation crystals for Laue lens applications, *Proc of SPIE, Volume 6688* (2008).

[51] V. Bellucci, R. Camattari, V. Guidi, A. Mazzolari, Bending of silicon plate crystals through superficial grooving: Modeling and experimentation, *Thin Solid Films, vol. 520, issue 3, pp. 1069-1073* (2011).

[52] V. Bellucci, R. Camattari, V. Guidi, I. Neri, N. Barriere, Self-standing bent silicon crystals for very high efficiency Laue lens, *Experimental Astronomy, Volume 31, Issue 1, pp.45-58* (2011).

[53] R. Camattari, V. Guidi, I. Neri, Quasi-mosaicity as a tool for focusing hard x-rays, *Proc. of SPIE Vol. 8443* (2012).

[54] Guidi Vincenzo, Camattari Riccardo, Neri Ilaria and Lanzoni Luca, Bent crystals as high-reflectivity components for a Laue lens: basic concepts and experimental techniques, *Proc. of SPIE Vol. 8443* (2012).

[55] Yu. M. Ivanov, A. A. Petrunin, and V. V. Skorobogatov, Observation of the Elastic Quasi-Mosaicity Effect in Bent Silicon Single Crystals, *JETP Letters, Vol. 81, No. 3, pp. 99-101* (2005).

[56] Vincenzo Guidi, Valerio Bellucci, Riccardo Camattari and Ilaria Neri, Proposal for a Laue lens with quasi-mosaic crystalline tiles, *JJ. Appl. Cryst. 44, 1255-1258.* (2011).

[57] Elisa Buffagni, Claudio Ferrari, Francesca Rossi, Laura Marchini, Andrea Zappettini, Preparation of bent crystals as high efficiency optical elements for hard x-ray astronomy, *Proc. of SPIE Vol. 8147* (2011).

[58] C. Ferrari, Zanotti, A. Zappettini and S. Arumainathan, Mosaic GaAs crystals for hard x-ray astronomy, *Proc. of SPIE Vol. 7077* (2008).

[59] Claudio Ferrari, Elisa Buffagni, Laura Marchini, Andrea Zappettini, High resolution x-ray characterization of mosaic crystals for hard x- and gamma-ray astronomy, *Proc. of SPIE Vol. 8147* (2011).

[60] Elisa Buffagni , Elisa Bonnini, Andrea Zappettini, Francesca Rossi, Claudio Ferrari, Crystal bending by surface damaging in mosaic GaAs crystals for the LAUE project, *Proc. of SPIE Vol. 8861-13* (2013).

[61] C. Ferrari, E. Buffagni, E. Bonnini, A. Zappettini, X-ray diffraction efficiency of bent GaAs mosaic crystals for the LAUE project, *Proc. of SPIE Vol. 8861-12* (2013).

[62] V. Liccardo, E. Virgilli, F. Frontera, V. Valsan, Characterization of bent crystals for Laue lenses, *Proc. of SPIE Vol. 8443* (2012).

[63] Kunieda, H., Awaki, H., Furuzawa, A., Haba, Y., Iizuka, R., Ishibashi, K., , Ishida, M., Itoh, M., Kosaka, T., Maeda, Y., Matsumoto, H., Miyazawa, T., Mori, H., Namba, Y., Ogasaka, Y., k. Ogi, Okajima, T., Suzuki, Y., Tamura, K., Tawara, Y., Uesugi, K., Yamashita, K., and Yamauchi, S., Hard x-ray telescope to be onboard ASTRO-H, in *Proc. of SPIE Vol. 7732* (2010).

[64] F. Frontera, E. Virgilli, V. Valsan, V. Liccardo, V. Carassiti, E. Caroli, F. Cassese, C. Ferrari, V. Guidi, S. Mottini, M. Pecora, B. Negri, L. Recanatesi, L. Amati, N. Auricchio, Scientific prospects in soft gamma-ray astronomy enabled by the LAUE project, *Proc. of SPIE Vol. 8861* (2013).

[65] E. Virgilli, F. Frontera, V. Valsan, V. Liccardo, E. Caroli, J.B. Stephen, F. Cassese, L. Recanatesi, M. Pecora, S. Mottini, P. Attina, B. Negri, The LAUE project for broadband gamma-ray focusing lenses, *Proc. of SPIE Vol. 8147* (2011).

[66] E. Virgilli, F. Frontera, V. Valsan, V. Liccardo, V. Carassiti, S. Squerzanti, M. Statera, M. Parise, S. Chiozzi, F. Evangelisti, E. Caroli, J. Stephen, N. Auricchio, S. Silvestri, A. Basili, F. Cassese, L. Recanatesi, V. Guidi, V. Bellucci, R. Camattari, C. Ferrari, A. Zappettini,

E. Buffagni, E. Bonnini, M. Pecora, S. Mottini, and B. Negri, The LAUE project and its main results, *Proc. of SPIE Vol. 8861* (2013).

[67] F. Frontera, E. Virgilli, V. Liccardo, V. Valsan, V. Carassiti, S. Chiozzi, F. Evangelisti, S. Squerzanti, M. Statera, V. Guidi, C. Ferrari, Development status of the LAUE project, *Proc. of SPIE Vol. 8443* (2012).

[68] Caroli E., Auricchio N., Basili A., Carassiti V., Cassese F., Sordo S. D., Pecora F. F. M., Recanatesi L., Schiavone F., Silvestri S., Squerzanti S., Stephen J. B., and Virgilli E., The ground support equipment for the laue project, *SPIE Conference Series 8861-7* (2013).

[69] V. Valsan, E. Virgilli, F. Frontera and V. Liccardo, Results of the simulations of the petal/lens as part of the laue proiect, *Society of Photo-Optical Instrumentation Engineers (SPIE) Conference Series, 8861* (2013).

[70] U. Bergmann, and S. P. Cramer, High-Resolution Large-Acceptance Analyzer for X-ray Fluorescence and Raman Spectroscopy, *SPIE Conference Series 3448, p. 198-209* (1998).

[71] J.W.M. DuMond, and H. A. Kirkpatrick, The multiple crystal X-ray spectrograph, *Review of Scientific Instruments, Vol. 1, Issue 2* (1930).

[72] S. Huotari, F. Albergamo, Gy. Vanko, R. Verbeni and G. Monaco, Resonant inelastic hard x-ray scattering with diced analyzer crystals and position-sensitive detectors, *Review of scientific instruments 77, 053102* (2006).

[73] R. Verbeni, M. Kocsis, S. Huotari, M. Krisch, G. Monaco, F. Sette, G. Vanko, Advances in crystal analyzers for inelastic X-ray scattering, *Journal of Physics and Chemistry of Solids, Volume 66, Issue 12, p. 2299-2305* (2005).

[74] Roberto Verbeni, Tuomas Pylkkanen, Simo Huotari, Laura Simonelli, Gyorgy Vanko, Keith Martel, Christian Henriquet and Giulio Monaco,

Multiple-element spectrometer for non-resonant inelastic X-ray spectroscopy of electronic excitations, *Journal of Synchrotron Radiation ISSN 0909-0495* (2009).

[75] A. Goldwurm, E. Brion, P. Goldoni, P. Ferrando, F. Daigne, A. Decourchelle, R.S. Warwick, P. Predehl, A New X-Ray Flare from the Galactic Nucleus Detected with the XMM-Newton Photon Imaging Cameras, *ApJ* ***584*** *751* (2003).

[76] Gruber, D. E.; Blanco, P. R.; Heindl, W. A.; Pelling, M. R.; Rothschild, R. E.; Hink, P. L., The high energy X-ray timing experiment on XTE, *Astronomy and Astrophysics Supplement, v.120, p.641-644* (1996).

[77] Winkler C., INTEGRAL - Overview and Current Status, *Proceedings of the 5th INTEGRAL Workshop on the INTEGRAL Universe (ESA SP-552)* (2004).

[78] J. Wang and T.J. Blackburn, X-ray image intensifiers for fluoroscopy, *Radio Graphics, Vol. 20 Issue 5* (2000).

[79] T. Jerrold Bushberg, J. Anthony Seibert, M. Edwin Leidholdt Jr, and M. John Boone, The essential physics of medical imaging, 2nd ed, *Lippincott Williams & Wilkins* (2002).

[80] G. Kirchhoff, *Ann. d. Physik. p663, 2, 18,* (1883).

[81] Takagi S., A dynamical theory of diffraction for a distorted crystal, *Journal of Physical Society of Japan Vol. 26, pp. 1239* (1969).

[82] Watson et al., The XMM-Newton Serendipitous Survey, *A&A 365, L51-L59* (2001).

[83] ESA website *http://www.rssd.esa.int.*

[84] Valsan V., PhD Thesis, Extending the band of focusing X-ray telescopes: motivations and proposed solutions, Universita di Ferrara, 2013.